

Volcanic Tremor and Physical Source Models: Lascar Volcano, Chile

Von der Fakultät Geo- und Biowissenschaften der Universität Stuttgart
zur Erlangung der Würde eines Doktors der
Naturwissenschaften (Dr. rer. nat.) genehmigte Abhandlung

Vorgelegt von Margaret Hellweg aus Cambridge, Massachusetts

Hauptberichter: Prof. Dr. R. Schick
Mitberichter: Prof. Dr. E. Wielandt
Tag der mündlichen Prüfung: 22. Februar 2000

Institut für Geophysik der Universität Stuttgart

2000

Contents

	Abstract	5
	Zusammenfassung	9
1	Introduction	19
1.1	Background	19
1.2	Objectives	21
2	Lascar Volcano: The Wavefield	23
2.1	The Volcano	23
2.2	The Measurements	23
2.3	Characteristic Seismic Signals of Lascar Volcano	27
2.3.1	Rapid Fire Tremor	27
2.3.2	Tornillos	32
2.3.3	Harmonic tremor	36
3	Harmonic Tremor: Analysis	41
3.1	Seismograms	41
3.1.1	Waveforms	41
3.1.2	Amplitudes	42
3.2	Spectra and Spectrograms	45
3.2.1	Powerspectra	45
3.2.2	Spectrograms	46
3.2.3	Phasograms	48
3.3	The Reduced Instantaneous Phase	50
3.4	Polarization	57
3.4.1	Particle Motion Diagrams	58
3.4.2	Directional Dependence of the Spectral Intensity	60
3.4.3	Polarization Rosettes and Polarograms	65
3.5	Summary of Observations and their Implications for Harmonic Tremor	68
4	Tremor Frequency: The Source	71
4.1	Vortex Shedding	73
4.2	Turbulent Slug Flow	81
4.3	Soda Bottle	90
5	Tremor Polarization: The Medium	99
5.1	Scattering	99
5.2	Superposition	108
5.3	Surface Reflections	110
5.4	Summary	113
6	Conclusions	115
7	Definition of Variables	119
8	References	123
	Acknowledgements	131

Abstract

Lascar, the most active volcano in northern Chile, lies near the center of the region studied during the Proyecto de Investigación Sismológica de la Cordillera Occidental 94 (PISCO '94). Its largest historical eruption occurred on 19 April 1993. During the spring of 1994, its activity consisted mainly of a plume of water vapor and SO₂. In April and May 1994, three short-period, three-component seismometers were placed on the flanks of the volcano, augmenting the broadband seismometer located on the NW flank of the volcano during the entire deployment. In addition to the usual seismic signals recorded at volcanoes, during this deployment Lascar produced several unusual tremor types: Rapid-fire tremor, tornillos and harmonic tremor.

Rapid-fire tremor (RF tremor) appears to be a sequence of very similar, but independent, impulsive events (RF events) with a large range of amplitudes. The similarity in the frequency content of many of the individual RF events indicates that they are all generated in a single relatively small volume near or under the active crater. Statistical analysis of a suite of these events indicates that both large and small RF events have similar source mechanisms.

Tornillos, nearly monochromatic events with slowly decaying codas are present at frequencies between 1 and 4 Hz, as at other volcanoes in South America. Additional tornillos were recorded with characteristic frequencies between 5 and 10 Hz. The mechanism which produces these unusual waveforms is still unknown.

Harmonic tremor is a continuous, cyclic signal lasting several hours. It is characterized by a spectrum with peaks at a fundamental frequency at about 0.63 Hz and up to 30 integer overtones. Power spectra and spectrograms of Lascar's harmonic tremor demonstrate that the frequencies recorded are the same at all stations, and therefore cannot be explained as path effects. They must be attributed to mechanisms at or near the source. On the other hand, the polarization of the wavefield cannot be simply explained as the propagation from a single source of any of the classical types of seismic waves. Harmonic tremor signal polarization and amplitudes are not correlated across the network, while frequency changes are consistent across stations and components. The fundamental frequency changes at the

same time at all stations, indicating that such changes must be caused at the source. These observations must be explained by volcano models.

Two particular observations of the spectral peaks of Lascar's harmonic tremor lead to the suggestion of new models for the source of this tremor. First, changes in the frequency of the fundamental, f_1 , are reflected exactly in the frequencies of the overtones, $f_n(t) = nf_1(t)$, while peak-broadening in the power spectra is the result of shifts in the frequency as a function of time. Secondly, many, up to 30, overtones were observed at Lascar. Harmonics are not only observed as higher order resonances of an oscillating system. They also occur in the spectrum of a source signal if it is repetitive but nonsinusoidal. Fluid dynamics offers at least three source models for harmonic tremor for systems which may exist in volcanos and which produce repetitive, nonsinusoidal waveforms: The release of gas through a very small outlet (the soda bottle model), regular, intermittent turbulence in a narrow conduit (the slug flow model), and the shedding of von Kármán vortices produced at obstacles (the vortex shedding model). These models represent different flow regimes, each with its own characteristic range of Reynolds numbers. For each model, the fundamental frequency of the tremor is related to the Reynolds number for the flow. Combining the Reynolds numbers for each model with typical kinematic viscosities for the possible fluids present in a volcano — magma, water, steam, air or some combination, at appropriate temperatures and pressures — provides limits on such physical parameters of the volcano as the dimensions of the flow conduit and the flow velocity of the fluid generating the tremor. If any single one of these three models is actually the process in the volcano which generates harmonic tremor, then the tremor must be caused by movements of water or gases in the hydrothermal system near the volcano's surface.

The interpretation of the polarization of the harmonic tremor wavefield is more difficult than in earthquake seismology, where the polarization is used to determine wavetype and the direction to the source. Volcanic tremor in general, and each peak of harmonic tremor in particular, consists of a narrowband wavefield propagating through the heterogeneous volcanic edifice. While its polarization may be due to a complicated source mechanism or an extended source, simple models for scattering, superposition and surface reflection can

qualitatively explain its complexity. For an impulsive source pulse, propagation through a three-dimensional acoustic model of random scatterers reproduces the well-known shape of volcanic shocks, with the density of the scatterers controlling the length and the relative amplitude of the coda. While the polarization of the initial arrivals depends only on the direction between the source and the receiver, the polarization of the coda is random and changes for each realization of the medium. Continuous narrowband signals, simulated by a sine wave, produce a transient following the first arrival, during which the scattering space is filled by waves. When the scattering space has been saturated, the polarization at the receiver remains constant, but apparently unrelated to the source-receiver direction. Small changes in the frequency or location of the source may cause large changes in the polarization. For a wavefield such as that generated by harmonic tremor, both the polarization and amplitude of the individual spectral lines depend strongly on their frequency. Similarly, superposition of continuous, narrowband P- and S-waves or the effects of reflection at the receiver produce an initial transient and then a constant wavefield polarization with little relationship to the source-receiver direction. The polarization of volcanic tremor's continuous, narrowband signals tells more about the medium than the source.

Zusammenfassung

Lascar, der aktivste Vulkan im Norden Chiles, ist ein mehr als 5000 m hoher Stratovulkan bei $23^{\circ} 22' S$, $67^{\circ} 44' W$. Sein größter, historisch bekannter Ausbruch fand am 19. April 1993 statt. Lascar liegt im Zentrum eines während des Proyecto de Investigación Sismológica de la Cordillera Occidental 94 (PISCO '94) aufgebauten seismischen Netzes. Im Rahmen dieser Messkampagne nahmen Mitarbeiter des Sonderforschungsbereichs (SFB) 267, '*Deformationsprozesse in den Anden*', die großräumige Seismizität der Zentralanden auf. Während dieses Messprogramms wurde im April und Mai 1994 für mehr als 30 Tage auch ein Seismometer-Netz um den Vulkan installiert. Es bestand aus einem Breitbandseismometer an der Nordwestflanke und drei kurzperiodischen Dreikomponenten-Stationen im Nordosten sowie an der Südseite. Während der Messungen war Lascars eruptive Aktivität weitgehend abgeklungen. Allerdings konnte das kontinuierliche Ausströmen großer Mengen von Wasserdampf und SO_2 beobachtet werden. Von den Instrumenten des Lascar-Netzes wurden außer den üblichen vulkanseismischen Signalen drei ungewöhnliche Tremortypen registriert: Rapid-Fire Tremor, Tornillos und harmonischer Tremor.

Rapid-Fire Tremor (RF-Tremor) besteht aus einer Abfolge von einander in der Wellenform ähnlichen, aber statistisch unabhängigen, impulsiven Ereignissen. Obwohl zwischen den einzelnen RF-Events starke Variationen in der Amplitude bestehen, zeigen ihre Spektren große Ähnlichkeiten. Das deutet darauf hin, dass die Quelle dieser Events in einem begrenzten Volumen in der Nähe des aktiven Krater liegt. Eine statistische Analyse einer großen Anzahl der RF-Events lässt außerdem darauf schließen, dass der Quellmechanismus für alle Ereignisse dieser Klasse sehr ähnlich sein muss.

Bei den Tornillos handelt es sich um Ereignisse mit langsam abklingender Amplitude und einem annähernd monochromatischen Spektrum. Es lassen sich zwei Gruppen unterscheiden mit charakteristischen Frequenzen zwischen 1 und 4 Hz, beziehungsweise zwischen 5 und 10 Hz. Der Quellmechanismus der Tornillos ist noch unbekannt.

In der vulkanologischen Literatur wird schon seit langem "harmonic tremor" an zahlreichen Vulkanen beschrieben. Darunter versteht man in der Regel sinusförmige Tremor-Signale mit einer oder wenigen dominierenden Frequenzen. Lascars harmonischer Tremor ist dagegen ein kontinuierliches, zyklisches Signal, dessen Spektrum aus schmalbandigen Spitzen mit einer Grundfrequenz von 0,63 Hz und bis zu 30 ganzzahligen Vielfachen davon besteht. Während der Messungen gab es einige Phasen harmonischen Tremors, die jeweils mehrere Stunden lang anhielten und an allen Stationen registriert wurden. Wie bei anderen Formen des vulkanischen Tremors gibt es auch beim harmonischen Tremor keine scharfen Einsätze. Vielmehr entsteigt dessen Signal nur langsam aus dem Hintergrundrauschen. Die Signalform des harmonischen Tremors lässt sich durch eine strenge Periodizität und schroffe Spitzen beschreiben. Ziel dieser Arbeit ist es, diesen Tremor an Hand von Signalform und Amplitude zu charakterisieren, ihn zu analysieren und Modelle für seinen Quellmechanismus zu entwickeln.

Ein erster Schritt bei der Analyse des harmonischen Tremors ist es, die für die Erzeugung des Tremorwellenfeldes nötige, im Quellgebiet aufzuwendende Kraft aus der Größe der Signalamplitude abzuschätzen. Dabei wird hier das komplizierte seismische Medium des Vulkangebäudes des Lascar durch einfache Annahmen simuliert, so dass sich bei der Abschätzung lediglich ein unterer Grenzwert der Quellstärke ergibt. Besteht das Wellenfeld des harmonischen Tremors aus P-Wellen, und werden diese Wellen durch eine Punktkraft erzeugt, muss sie mindestens 3×10^8 N betragen. Besteht das Tremorwellenfeld dagegen aus S-Wellen, ist die minimale Punktkraft in der Quellregion dagegen nur 1×10^8 N groß.

Ein zweiter Schritt bei der Analyse ist die Anwendung sogenannter "Phasogramme". Diese Methode erlaubt es zunächst, schmalbandige Signale, wie die der einzelnen spektralen Spitzen des harmonischen Tremors, qualitativ zu untersuchen. Dazu wird die Zeitreihe in einem schmalen Frequenzband um die Grundfrequenz gefiltert. Dabei zeigt sich, dass Frequenzänderungen gleichzeitig und in gleicher Amplitude auf allen Stationen des Netzes zu beobachten sind. Das deutet darauf hin, dass die Frequenzänderungen unabhängig vom

Wellenweg und vom Seismometerort sind, also von der Quelle des harmonischen Tremors herrühren müssen.

Eine quantitative Untersuchung der zeitlichen Änderungen in der Frequenz des Signals ist nach der Berechnung der momentanen Phase, ihrer Ableitung, der momentanen Frequenz, sowie der reduzierten momentanen Phase möglich. Im Gegensatz zu Analysen des zeitlichen Verhaltens der Frequenz mit anderen Methoden wie den Spektrogrammen finden diese Berechnungen im Zeit- und nicht im Frequenzbereich statt. Deshalb können Frequenzänderungen wesentlich detaillierter verfolgt werden.

Die Anwendung dieser Verfahren zeigt, dass die Änderungen der Frequenz des harmonischen Tremor auf allen Komponenten gleichzeitig zu beobachten sind. Im Analyseintervall schwankt die Grundfrequenz zwischen 0,617 Hz und 0,648 Hz. Änderungen der Frequenzen der Obertöne im gleichen Intervall stehen im ganzzahligen Verhältnis zur Änderung der Grundfrequenz. Wenn die Frequenz des Grundtons um 0,05 Hz steigt, steigen beispielsweise die Frequenzen der ersten und zweiten Obertöne um 0,10 Hz beziehungsweise 0,15 Hz.

Die Polarisationsanalyse ist in der Erdbebenseismologie eine wichtige Methode zur Untersuchung eines seismischen Wellenfeldes. Ist beispielsweise der Ort der Quelle bekannt, kann aus der Polarisation eines Wellenzuges der Wellentyp abgelesen werden. Ist dagegen der Wellentyp bekannt, kann man auf die Richtung zur Quelle schließen. Es liegt also nahe zu versuchen, ähnliche Schlüsse auch aus der Polarisation des harmonischen Tremors zu ziehen. Eine Untersuchung der Partikelbewegung für die ersten drei spektralen Spitzen an den vier Stationen des Lascar-Netzes lässt aber keine eindeutige Beziehung zwischen Wellentyp und Ausbreitungsrichtung erkennen. Das gilt einerseits für kurze Zeiträume von mehreren Sekunden. Obwohl sich in dieser Zeit die Orientierungen der Partikelbewegungen für die einzelnen Frequenzen an den verschiedenen Stationen nicht ändern, sind sie nicht - wie bei einem von einem Erdbeben ausgehenden Wellenfeld - mit der Ausbreitung eines einzelnen Wellentyps von einer Punktquelle in einem einfachen Medium zu erklären. Zusätzlich

ist bemerkenswert, dass die Verhältnisse der Amplituden der Bodenbewegungen für die verschiedenen Obertöne an den einzelnen Stationen des Netzes sehr unterschiedlich sind. Auch bei der Analyse längerer Zeitintervalle lässt sich die Polarisierung der Bodenbewegungen an den einzelnen Stationen nicht mit der Ausbreitung eines einzelnen Wellentyps von einer Punktquelle in einem einfachen Medium erklären. Das ergibt die Untersuchung der Richtungsabhängigkeit der spektralen Intensität sowie die Auswertung zweidimensionaler Histogramme der Polarisierung, der so genannten Polarogramme.

Die Deutung der Polarisierung des Wellenfeldes des harmonischen Tremors ist also weitaus schwieriger als in der Erdbebenseismologie. Obwohl nicht ausgeschlossen werden kann, dass die komplizierte Polarisierung des Tremors von einer komplexen oder ausgedehnten Quelle stammt, können sehr einfache Modelle für Streuung, Wellenüberlagerung und Reflexionen an der Oberfläche die beobachteten Signale erklären. Dazu werden zunächst vulkanische Erdbeben durch eine impulsive Quelle simuliert, deren Wellenfeld sich durch ein dreidimensionalen Raum voller Streukörper ausbreitet. Berechnet wird hier nur der akustische Fall, also die Ausbreitung von P-Wellen. Dabei bestimmen die Anzahl und Dichte der Streukörper die Länge und relative Amplitude der Coda. Obwohl die Polarisierung des Ersteinsatzes nur von der Richtung zwischen Quelle und Empfänger abhängt, ist die Polarisierung der Coda zufällig.

Kontinuierliche, schmalbandige Signale, wie beispielsweise die einzelnen spektralen Spitzen des harmonischen Tremor, werden durch eine Sinuswelle simuliert. In den entsprechenden synthetischen Seismogrammen erscheint nach dem Ersteinsatz ein Einschwingvorgang. In dieser Zeit wird das Medium mit den Sinuswellen gesättigt. Danach bleibt zwar die Polarisierung der Bodenbewegung am Empfänger konstant. Die Polarisierungsrichtung steht aber in keinem Zusammenhang mehr mit der Richtung zur Quelle. Sie wird vielmehr durch die Position und Stärke der Streukörper im Medium bestimmt. Kleine Änderungen in der Frequenz oder der Position der Quelle können große Änderungen in der Polarisierung bewirken.

Das komplette Wellenfeld des harmonischen Tremors, das aus einer Überlagerung von vielen schmalbandigen Signalen besteht, wird durch eine Rechteckwelle simuliert. In diesem Fall hängen sowohl die Polarisierung als auch die Signalamplitude der einzelnen spektralen Spitzen nicht nur von der Position und der Stärke der Streukörper ab. Die beiden Messgrößen werden auch stark von der Frequenz der Welle beeinflusst. Bei keinem der schmalbandigen Signale gibt es jedoch eine Verbindung zwischen der Orientierung der Partikelbewegung und der Richtung zur Quelle.

Ein ähnlicher Effekt lässt sich beobachten, wenn man die Ausbreitung von P- und S-Wellen in einem homogenen Medium betrachtet. Ist das Quellsignal impulsiv, kann man klar die Einsätze von P und S auf den radialen und transversalen Komponenten der Seismogramme unterscheiden. Bei der Sinuswelle wird die zunächst in Richtung der Quelle zeigende Polarisierung nach dem Eintreffen der S-Wellen verschoben. Das Maß der Verschiebung hängt dabei von der Entfernung zur Quelle ab. Das aus P- und S-Wellen bestehende Wellenfeld einer Rechteckwelle simuliert schließlich die Polarisierung des harmonischen Tremors hinreichend. Die Polarisierungsrichtungen der einzelnen Oberwellen sind dabei gegenüber der ursprünglichen Richtung der P-Welle jeweils um ein anderes Maß rotiert, so wie es auch beim harmonischen Tremor beobachtet wird.

Da die komplizierte Polarisierung des Wellenfeldes des harmonischen Tremors sich mit diesen einfachen Modellen des Mediums erklären lässt, können daraus also keine Informationen über die Quelle abgeleitet werden. Welche Eigenschaften des harmonischen Tremors kann man aber nun benutzen, um die Quelle zu modellieren? Die Frequenzen der Grundmode und der Obertöne bieten sich an, denn sie sind unabhängig von der Station und der Komponente. Sowohl die Grundfrequenz als auch die Obertöne ändern sich in allen Registrierungen gleichzeitig und gleichartig. Ihre Größen können deshalb nicht dem Wellenweg zugeschrieben werden. Die Beobachtungen deuten vielmehr darauf hin, dass die Frequenzänderungen in oder in unmittelbarer Umgebung der Quelle erzeugt werden, also durch physikalische Quellmodelle erklärt werden können. Obwohl die Frequenzen der

spektralen Spitzen und die jeweils empfangene Gesamtleistung des Wellenfeldes an den verschiedenen Stationen gut miteinander übereinstimmen, findet man dagegen in den an den verschiedenen Stationen aufgezeichneten Daten keine Korrelation bei den Tremoramplituden oder den Polarisierungen für die einzelnen spektralen Spitzen. Diese Signaleigenschaften können also nicht eindeutig der Quelle zugeschrieben werden.

In den meisten, bisher veröffentlichten Modellen vulkanischen Tremors wird die Quelle als Resonanz eines schwingungsfähigen Mediums behandelt. Das Medium ist dabei in einem begrenzten Volumen des Vulkans weitgehend stationär. Im Gegensatz dazu schlage ich nun Modelle für den harmonischen Tremor des Lascar vor, die auf der Strömungsmechanik eines fließenden Mediums beruhen. Die Modelle basieren auf zwei wichtigen Eigenschaften der spektralen Spitzen des harmonischen Tremors. Zum ersten gibt es eine genau ganzzahlige Gesetzmäßigkeit zwischen den Änderungen der Grundfrequenz und der Obertöne: $f_n(t) = n f_1(t)$. Zweitens enthalten die Spektren des harmonischen Tremor bis zu 30 Obertöne. Solche Obertöne werden nicht nur als Resonanzen höherer Ordnung in schwingungsfähigen Systemen beobachtet. Sie erscheinen auch in den Spektren von nichtsinusoidalen, jedoch zyklischen Signalen. In der Strömungsmechanik findet man mindestens drei Systeme, die solche zyklischen Signale erzeugen und die bei der Übertragung auf Vulkane realistische Größenordnungen liefern. Es sind:

- Die Bildung einer von-Kármán-Wirbelstraße an einem Hindernis (Vortex Shedding Model),
- intermittierende Turbulenz in einem schmalen Rohr oder Schlot (Slug Flow Model) und
- das langsame Ausströmen von Gas aus einem gesättigten System wie aus einer Sprudelflasche (Soda Bottle Model).

Diese drei Modelle repräsentieren unterschiedliche Flussbedingungen mit jeweils charakteristischen Reynoldszahlen. Für jedes Modell kann man die Frequenz des Tremors mit der Reynoldszahl der strömenden Substanz in Verbindung bringen.

Wirbelstraßen bilden sich häufig hinter einem Hindernis in einer Strömung. Sie entstehen, wenn sich dabei ab einer bestimmten Grenzggeschwindigkeit der Strömung regelmäßig Wirbel von dem Hindernis ablösen. Solche Wirbelstraßen sind beispielsweise die Quelle der Heultöne, die bei einem Sturm an einer Hausecke oder einer Überlandleitung entstehen. Die Frequenz des Heultons entspricht dabei der Ablösefrequenz der Wirbel. Bei einem strömenden Medium mit kinematischer Zähigkeit, κ , und der charakterischen Größe des Hindernisses, d , kann man die Ablösefrequenz, f_k , über die Reynoldszahl, $Re = vd/\kappa$, und die Strouhalzahl, $St = f_k d/v$, mit der Strömungsgeschwindigkeit, v , in Verbindung bringen. Bei der Anwendung dieses Modells auf den Vulkan Lascar nehme ich an, dass die Grundfrequenz des harmonischen Tremor der Ablösefrequenz der Wirbel entspricht. Das erlaubt Aussagen über das Strömungssystem im nicht ausbrechenden Vulkan. Magma scheidet beispielsweise als strömendes Medium aus. Um nämlich eine Tremorfrequenz von 0,63 Hz zu erzeugen, wären Fließgeschwindigkeiten von etwa 100 m/s und ein Hindernis mit einem Ausmaß von etwa 100 m notwendig. Diese Werte sind für einen "ruhenden" Vulkan zu groß. Die entsprechenden Werte für Dampf unter hohem Druck sind dagegen zu klein, um realistisch zu sein. Nur für Wasser, Dampf oder vulkanische Gase unter atmosphärischen Bedingungen ergibt das Modell realistische Strömungsgeschwindigkeiten von etwa 1 m/s und Hindernisgrößen von etwa 0,1 m. Die sich aus dem Modell ergebende Kraft, die ein ablösender Wirbel auf einen Zylinder ausübt, ist zwar wesentlich kleiner als die Punktkraft, die aus den Seismogrammen für die Quelle errechnet wurde. In der Literatur sind aber viele Hinweise darauf zu finden, dass bei der Berechnung für den einfachen Fall eines Zylinder als Hindernis die Werte für andere Formen von Hindernissen oft um Größenordnungen unterschätzt werden.

Periodische Kräfte gehen häufig auch von Strömungen mit intermittierender Turbulenz aus. Solche "Turbulenzpfropfen" können in einer sonst laminaren Strömung in langen Rohren oder Schloten bei einer kleinen Erhöhung der Strömungsgeschwindigkeit entstehen. Das turbulente Gebiet bedingt einen Stau in der Strömung, hinter dem die Geschwindigkeit wieder langsamer wird und die Strömung deshalb in ihren laminaren Zustand zurückkehrt. Im Laufe eines Zyklus arbeitet sich der Turbulenzpfropfen bis zum Ende des Rohrs durch.

Da die Flüssigkeit anschließend wieder ungestört laminar strömen kann, erhöht sich die Strömungsgeschwindigkeit so lange, bis ein neuer Turbulenzpfropfen entsteht. Solche Erscheinungen treten auf, wenn die Länge des Rohrs mindestens das Fünzigfache seines Durchmessers ist. Mit der Bildung und dem Zerfall der Turbulenzen gehen Druckänderungen auf die Wandung des Rohres einher. Daher lässt sich in diesem Modell die Aufenthaltsdauer des Pfropfens im Rohr mit der Tremorperiode gleichsetzen. Nimmt man nun an, dass die Strömungsgeschwindigkeit konstant ist, kann man das Entstehen und das Zerfallen der Turbulenzen mit einer Rechteckwelle modellieren. Aus dem Vergleich ihres Spektrums mit dem Spektrum des harmonischen Tremors ergibt sich für die Strömung eine Reynoldszahl von 2675. Daraus und aus der Frequenz des harmonischen Tremors lässt sich nun eine Abschätzung über die Art des strömendes Mediums machen. Andesit müsste mit mehr als 100 m/s fließen um einen entsprechenden harmonischen Tremor zu erzeugen. Derart hohe Flussgeschwindigkeiten von Magma sind aber in einem "ruhenden" Vulkan nicht zu erwarten. Die Strömungsgeschwindigkeit für Dampf unter hohem Druck ist dagegen mit 0,1 mm/s zu klein, um entsprechende Signale zu erzeugen. Realistische Werte sagt das Modell dagegen für Wasser, Dampf und vulkanische Gase unter atmosphärischen Verhältnissen voraus. Eine Abschätzung der Kräfte, die durch intermittierende Turbulenz in einem Vulkan auf das umgebende Medium ausgeübt werden, ergibt sich aus der Betrachtung der Impulsänderung bei der Änderung der Strömungsgeschwindigkeit. Für Wasser, Dampf und Luft sind die errechneten Kräfte allerdings um Größenordnungen geringer als man erwartet.

Das dritte Modell lässt sich mit einer Sprudelflasche vergleichen, die nur ein wenig geöffnet wird. Dabei treten oft periodische Druckschwankungen verbunden mit Blasenbildung auf. Nach dem ersten, durch das Öffnen verursachten Druckabfall bilden sich in der Flüssigkeit Blasen. Der damit verbundenen Druckanstieg gleicht zunächst den Druckabfall aus, lässt aber nach einer gewissen Zeit den Druck in der Flasche über den ursprünglichen Wert ansteigen, was die Blasenbildung unterbindet. Neue Blasen bilden sich erst wieder dann, wenn der Druck erneut gefallen ist. Das Druckverhalten dieses Systems kann durch eine nicht-lineare Gleichung beschrieben werden. Unter geeigneten Anfangsbedingungen treten

starke Druckschwankungen auf, die Ähnlichkeit mit den Seismogrammen des harmonischen Tremors haben. Dabei ist es wichtig, dass die Flüssigkeit nur wenig zäh ist. Nimmt man an, dass sich das Quellvolumen durch die Druckschwankungen ändert, kann man die Dimensionen dieser Änderung an Hand der Amplitude der Wegseismogramme abschätzen. Für den Vulkan Lascar ergibt sich dabei ein Grundvolumen von etwas mehr als 30000 m^3 .

Obwohl diesen drei Modellen für die Quelle des harmonischen Tremors völlig unterschiedliche Geometrien und physikalische Vorgänge zu Grunde liegen, zeigen sie doch mindestens eine überraschende Gemeinsamkeit. In ihnen wird der harmonische Tremor des Lascar jeweils durch die Strömungen von Wasser, Dampf oder vulkanischen Gasen in der Nähe der Oberfläche erzeugt. Das lässt den Schluss zu, dass die Quelle im hydrothermalen System des Vulkans zu suchen ist.

1 Introduction

1.1 Background

For generations, active volcanoes all over the world have fascinated mankind. The era of scientific observation began with Plinius the Younger's record of the eruption of Vesuvius in 79 A.D. At first, observations were limited to the descriptions of eruptions. Later, investigators broadened the scope of volcano studies to include geological, geochemical, petrological and mineralogical investigations. Despite this long history, very little is known about the physical processes which take place in volcanoes.

These processes occur on broad ranges in scale, both in space and time. Microscopic phenomena, such as the formation of crystals, are as important to understanding volcanoes as the tremendously large Plinian eruptions and pyroclastic flows which can kill thousands of people. Strombolian gas or ash explosions may last only minutes, while the extrusion of an andesitic lava dome can take many months. To describe the processes which occur in volcanoes requires many branches of physics. The fundamentals of rock mechanics, thermodynamics and fluid dynamics are all important. In addition, it is often necessary to consider the dynamics of two- or even three-phase systems, as well as modern methods for parametrizing non-linear processes, when describing volcanic phenomena.

A major obstacle to understanding the physics of volcanic systems is that it is not yet possible to directly measure physical state variables inside the volcano. We must therefore invent simple physical or chemical models for the processes which take place in volcanoes and constrain them using observations made at the surface. Years of seismic measurements have shown that such observations can be gathered by recording and analyzing the many different types of seismic signals produced by active volcanoes which can often be correlated with visible or audible activity [RIPEPE and BRAUN 1993, HELLWEG et al, 1994, WASSERMAN and SCHERBAUM, 1994, BENOIT and McNUTT, 1997, LEES et al, 1997]. Recent improvements in instrumentation allow continuous, high dynamic range recording of such volcanic seismic signals. Many other types of observation and measurement, such as tilt, deformation and

gravity, contribute important information to understanding volcanoes, but they are not conducive to continuous, immediate and remote observation as is seismology, nor can they capture the same dynamic range of activity.

Some volcanic seismic signals are like those known from earthquake seismology. They must be the result either of extensional or shear fractures, or of explosive point sources similar to those of explosion seismology. Such signals, however, represent only a small portion of the “seismic spectrum” of a volcano. More frequently, the volcanic seismic signals appear to be generated continuously by an unknown source within the volcano. These signals, which often vary in amplitude and frequency content and are present in some form at all active volcanoes, are called “volcanic tremor”.

What is the source of volcanic tremor? The term volcanic tremor describes a continuous sequence of seismic waves traveling through a complex medium, the volcano. Seismic waves can, for example, be generated by the action of a point force on the medium (AKI and RICHARDS, 1980) or by a change in the volume of a source region (WIELANDT, 1975). The source of tremor is a physical or chemical process in the volcano which produces seismic waves by acting as a time-dependent point force on the medium, or by causing the volume of the source region to change. A better understanding of volcanic tremor will provide insights into such processes in a volcano.

The analysis of volcanic tremor presents two problems to the seismologist. First, the multitude of volcanic seismic signals often exceeds the “classical” analysis possibilities offered by techniques developed for analysing the wavefield generated by the short excitations due to rock fracture or explosions. Second, the volcano is not a simple medium for wave propagation. Tremor analysis as a means of studying its source is complicated by the passage of the tremor waves through the highly inhomogeneous volcanic edifice. Analysis techniques from other branches of physics, information theory or mathematics offer some help in discovering and defining characteristics of volcanic tremor which may otherwise remain hidden in the seismic data. These characteristics, along with information attained using “classical” seismological methods must then be carefully analysed to determine whether they describe parameters of the tremor source or the path.

Finally, tremor source parameters derived from seismic measurements must be related to the variables of state in a volcano. Even thorough and exhaustive analysis of seismic data cannot replace the direct measurement of such variables. To improve our understanding, we must develop physical or chemical models for processes occurring in volcanoes and compare their predictions with the results of measurements.

1.2 Objectives

The spectrum of volcanic tremor is often characterized by narrowband peaks. In the past, tremor was recorded using single-component, low-gain equipment, leaving many questions about the tremor wavefield open. It was difficult to determine tremor parameters other than the frequency and amplitude or to distinguish between propagation effects and source characteristics. Without such discrimination, it is impossible to use tremor recordings to constrain models of physical or chemical processes in a volcano. Data from several three-component seismometers recorded with high dynamic range allow a more complete analysis of the tremor wavefield. As a result, tremor traits due to the source may be distinguished from those influenced by path and medium. The source-related parameters can then be used, along with source models, to determine the volcano's variables of state.

Although both chemical and physical interactions occur in volcanoes, there is, as yet, little evidence that chemical processes produce seismic signals. The goal of this thesis is, therefore, to develop physical models for the source of volcanic tremor using parameters measured from tremor recordings. The first step must therefore be to determine tremor characteristics which can be used for modelling. This occurs in Chapters 2 and 3. Only then (Chapters 4 and 5) can I propose and develop models for the source and path which use the tremor parameters, while at the same time making predictions about tremor behavior. I describe Lascar Volcano, the seismological measurements and a selection of Lascar's seismic signals (Chapter 2). During the deployment, Lascar generated a unique type of tremor, characterized by a harmonic spectrum with a sharply peaked fundamental and up to thirty integer overtone frequencies. I analyze this tremor to determine parameters which can be used for modelling and discuss the implications of the analysis results for the tremor

source (Chapter 3). One aspect of this discussion is the distinction between tremor characteristics which can be attributed to the source and can therefore be used to constrain physical models and those which may be affected by the path. In Chapter 4, I use the fundamental tremor frequency to develop three theoretical models for physical processes in Lascar Volcano which can generate harmonic tremor and compare their predictions with the results of tremor analysis. I follow this with a description of three simple models for the path of seismic waves through the volcano and relate them to the polarization of harmonic tremor (Chapter 5).

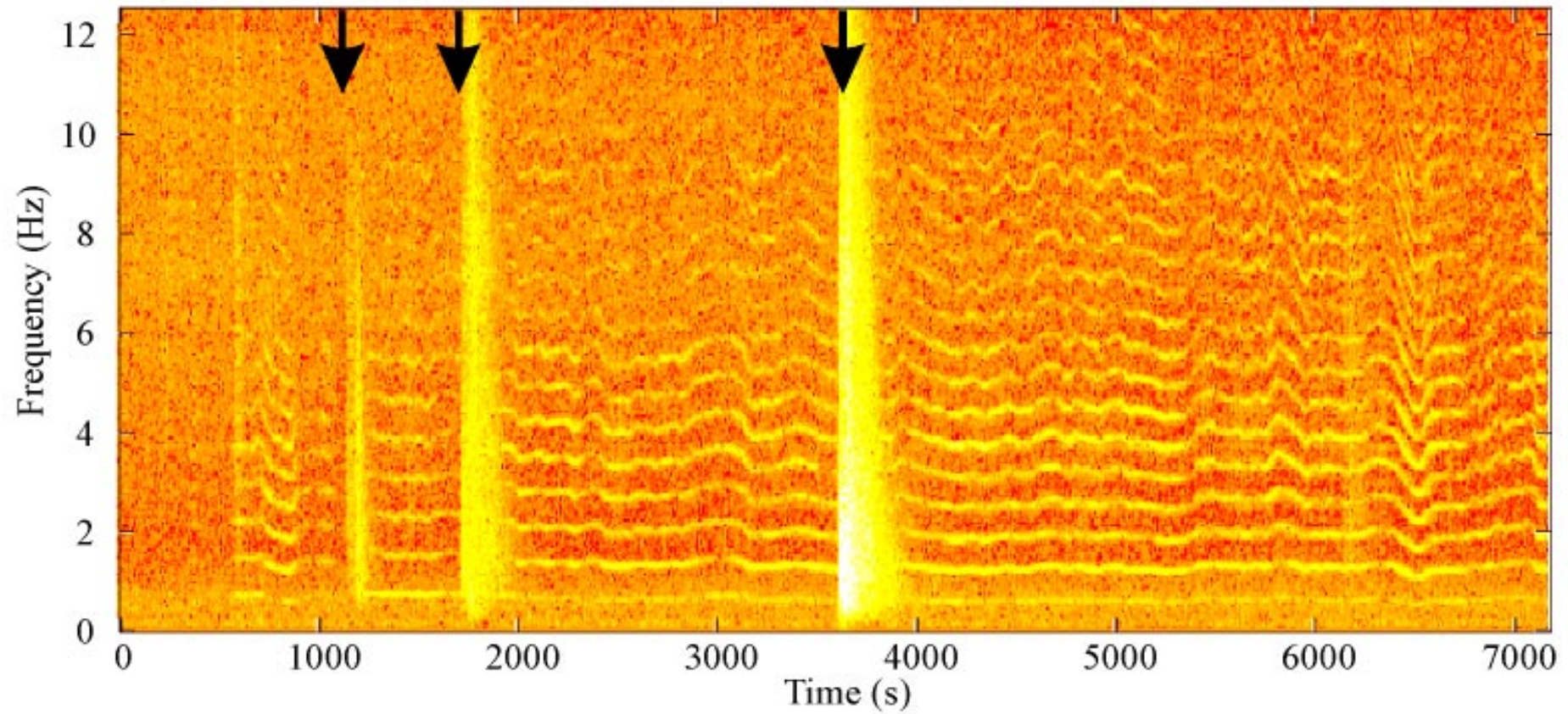


Figure 2.12 Spectrogram of two hours taken from the E-component at station LA2 starting at 01:30 on 18 April 1994. The data were resampled to 25 Hz. The spectrogram was calculated using data windows 10.24 s long and 50% overlapping. Arrows mark regional earthquakes.

This unusual form of tremor has a high signal-to-noise ratio in the recordings from Lascar. Because it has rarely been observed, it has not yet been analyzed and no models exist for its generation. Perhaps the results from an analysis of harmonic tremor from Lascar can offer new insights in the the physical processes occuring in volcanoes.

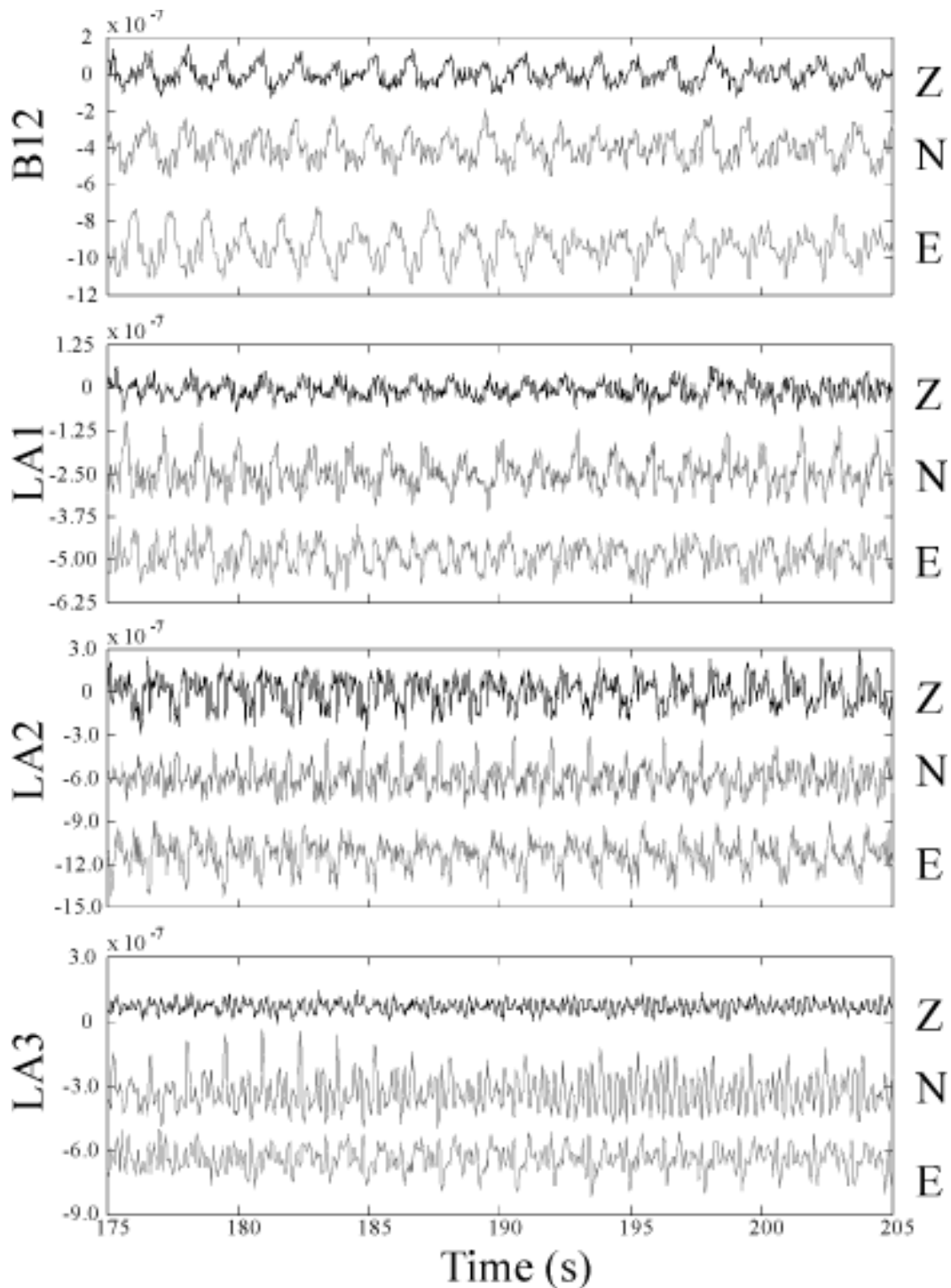


Figure 2.11 Thirty seconds of harmonic tremor at all stations. Here the broadband seismograms for station B12 are bandpass-filtered between 0.5 and 20 Hz and resampled to 50 Hz, as they have been for all other figures with no specific notes. Data for the short period stations have been lowpass-filtered and resampled to 50 Hz. The velocity amplitude is given in m/s.

the component with the largest amplitude at each of the stations (Figure 2.8) show energy is present at these frequencies during the entire recording. The physical process which generates tornillos is not yet known, although several models have been proposed [JULIAN, 1994, CHOUET 1996, SEIDL et al, 1998].

The Lascar stations also recorded a second type of tornillo, one with much higher characteristic frequencies. Figure 2.9 shows the recording and a spectrum from station LA2 for one of these high frequency events. The characteristic frequencies for this event, 11.50 Hz and 12.27 Hz, are present at all four Lascar stations (Figure 2.10). The interaction between these two neighboring frequencies is clearly visible as beating in the seismograms. Similar, high frequency events have also been observed at Galeras Volcano in Colombia [R. TORRES and D. GÓMEZ, personal communication, 1998].

2.3.3 Harmonic tremor

The recordings at Lascar also captured a new form of volcanic tremor characterized by harmonic spectra with a fundamental frequency near 0.6 Hz and many integer overtones with large amplitudes. In the past, volcanic tremor which is nearly sinusoidal has been called harmonic, however, here the signals with harmonic overtones will be called harmonic tremor (Figure 2.11). On each component, the tremor's shape changes slowly as a function of time. As this happens, the fundamental frequency changes, as do the amplitude of the cycle, the frequency content (amplitudes of overtones) and the polarization at each of the stations. At Lascar, harmonic tremor is not associated with volcanic explosions and may continue for several hours (Figure 2.12) with only small changes in the frequency of the fundamental. At Lascar on 18 April 1994, for example, harmonic tremor was recorded for more than 15 hours. Regional earthquakes (arrows) have no apparent effect on the frequency of the tremor. Similar signals observed at other volcanoes usually occur during a short interval following a triggering event and have only a few overtones [KAMO et al., 1977, MORI et al., 1989, SCHLINDWEIN et al., 1995, BENOIT and McNUTT, 1997, HAGERTY et al., 1997, LEES et al, 1997]. The only place where similar tremor may have been observed is Galeras Volcano, Colombia, in 1989 [GIL-CRUZ, 1999].

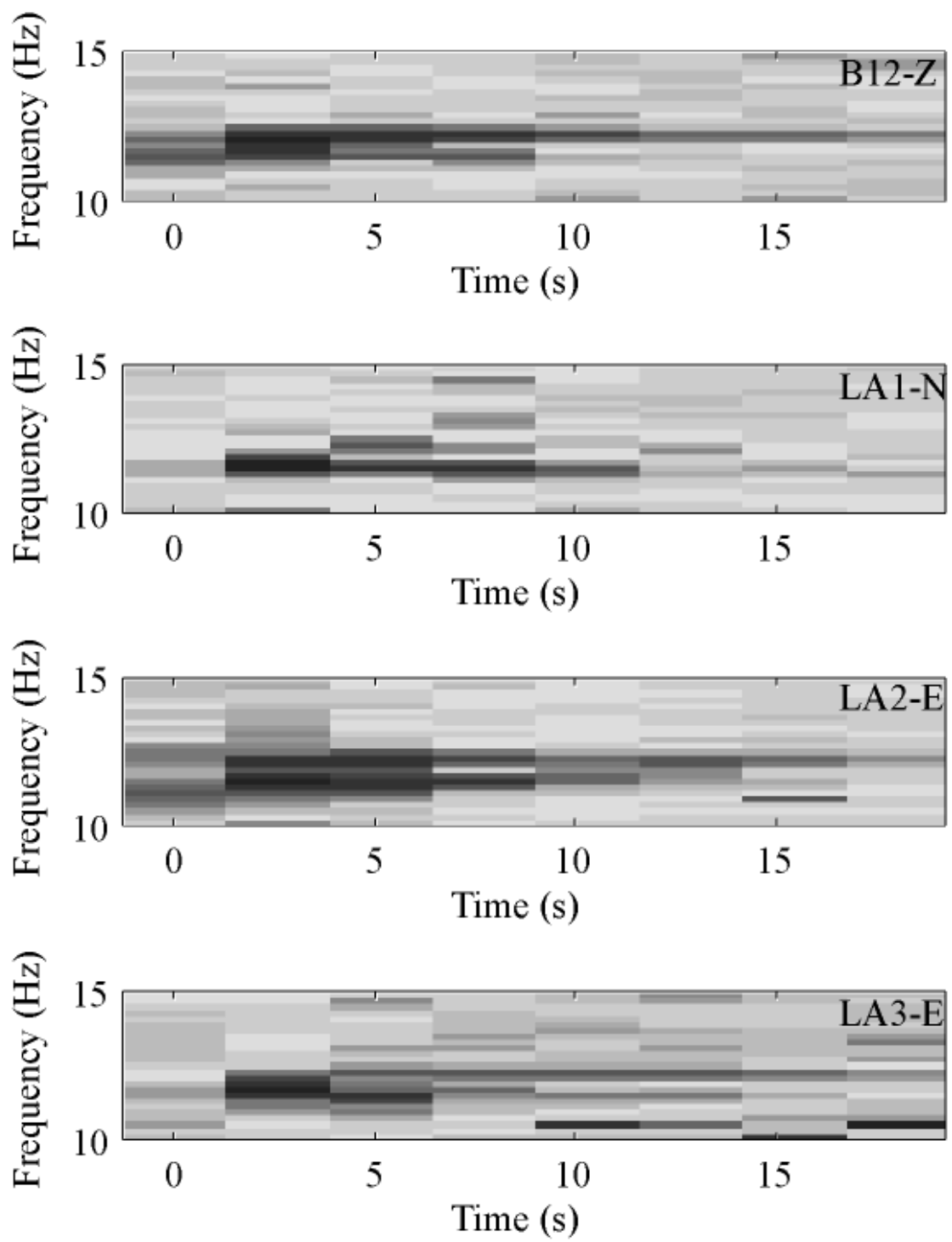


Figure 2.10 Spectrograms of the high frequency tornillo shown in Figure 2.9. For each station, the spectrogram is calculated and plotted for the component with the largest amplitude.

frequencies which usually lie between 1 Hz and 8 Hz. Similar events have also been observed at Asama-yama and Sakura-jima Volcanoes in Japan [SEKIYA, 1967, HAMADA *et al.*, 1976, and SAWADA, 1998]. Figure 2.7a shows a tornillo recorded at Lascar on 16 April 1994 at 15:43:26 UTC. The recordings have unusually long codas which look like sine waves with decreasing amplitude. The amplitude spectrum for the E component shows that the characteristic frequencies for this tornillo are 3.52 Hz and 6.24 Hz (Figure 2.7b). Spectrograms for

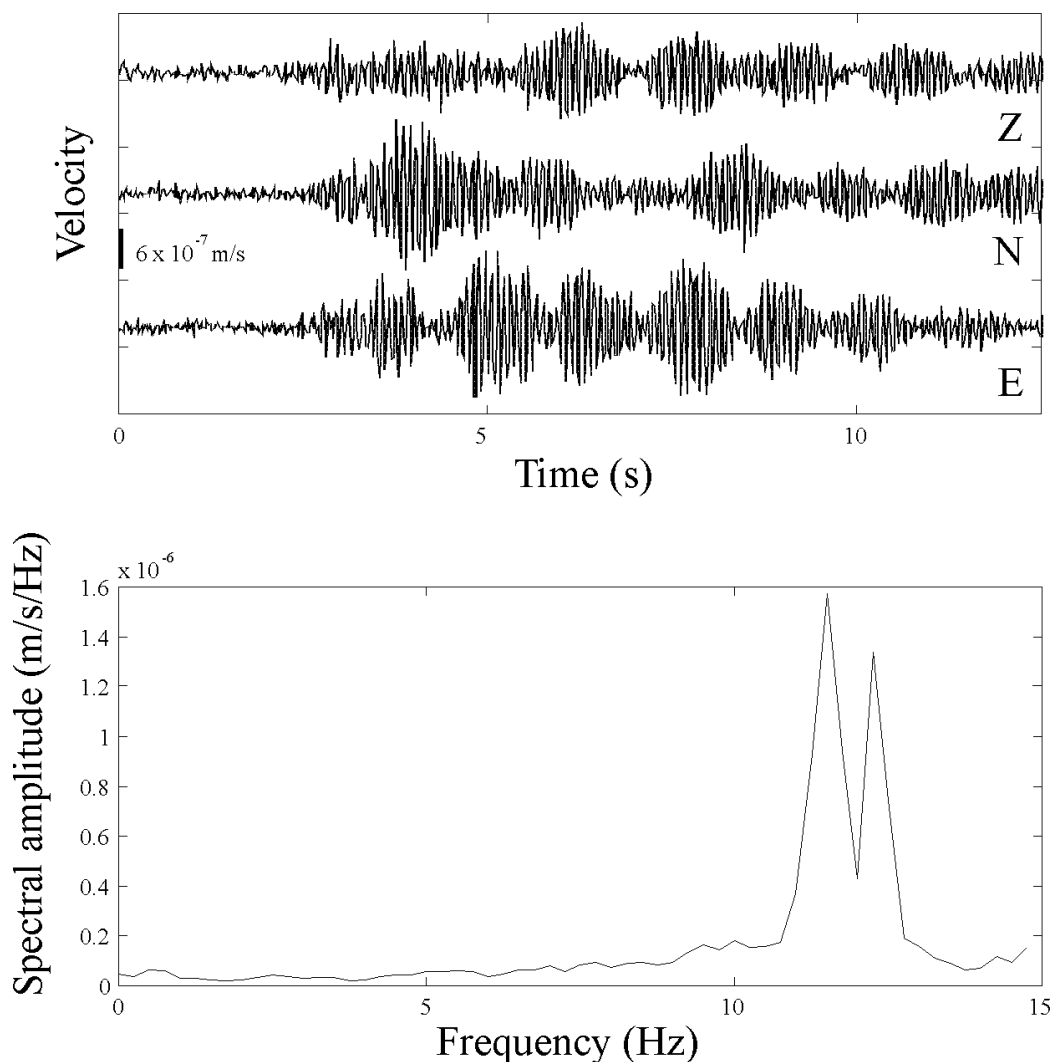


Figure 2.9 High frequency Lascar tornillo. (top) Seismograms of a high frequency tornillo (onset time 17 April 1994, 13:57:27 UTC) recorded at station LA2. The amplitude scale is marked by a bar on the left. (bottom) Spectrum of the high frequency tornillo from the E component of the recording at LA2.

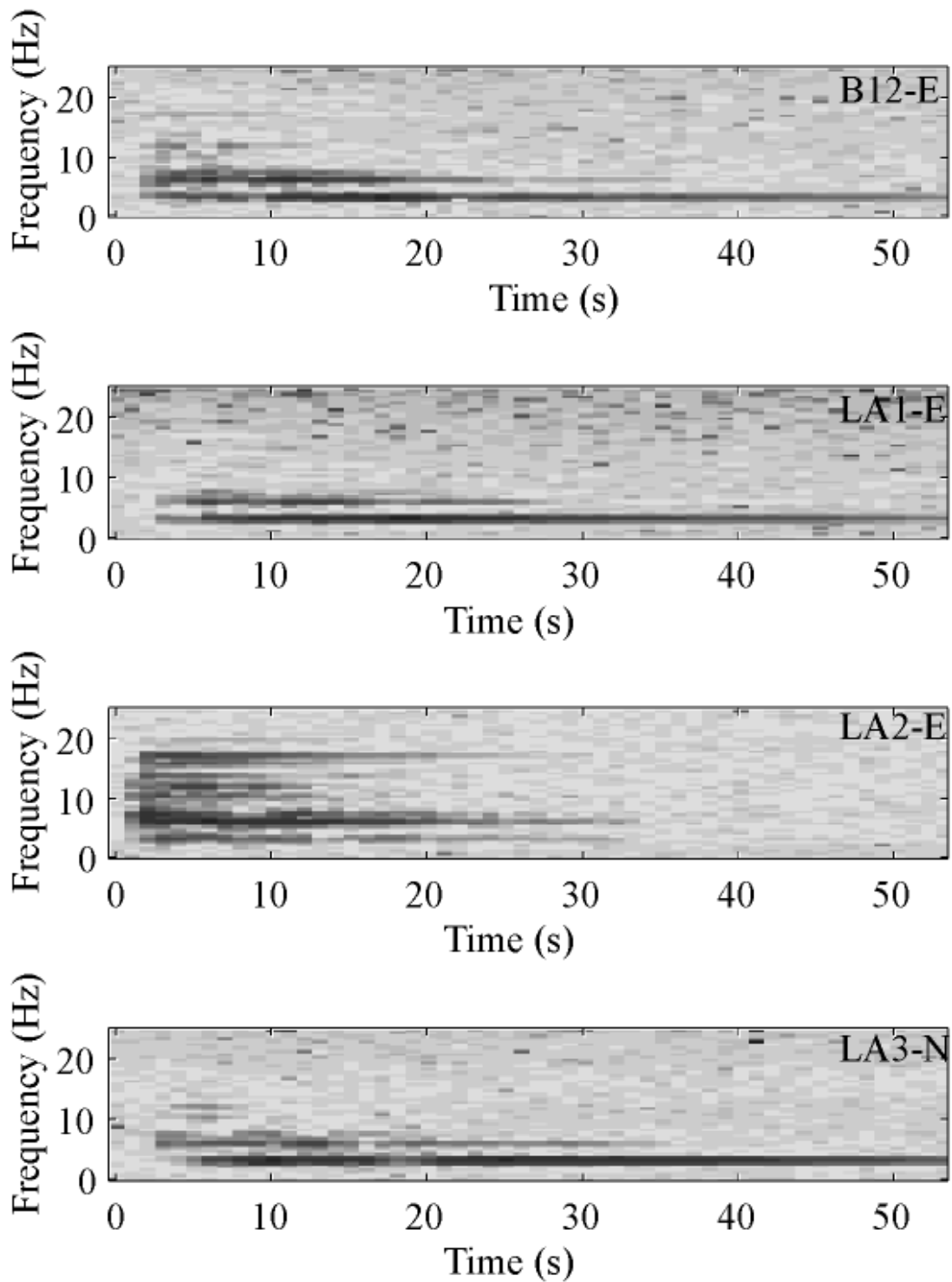


Figure 2.8 Spectrograms from the recordings of the tornillo in Figure 2.7. For each station, the spectrogram is calculated and plotted for the component with the largest amplitude.

2.3.2 Tornillos

In contrast to spectra measured from the seismograms of earthquakes or explosions, spectra of volcanic events and tremor often have well defined peaks at one or more frequencies. This is particularly true for an unusual type of event identified at Galeras Volcano in Colombia [GÓMEZ and TORRES, 1997, NARVÁEZ et al, 1997, TORRES et al, 1996]. These events are called tornillos, because their shape on a seismogram looks like a screw with a long, sinusoidal, slowly decaying coda. Each of these events has one or two predominant

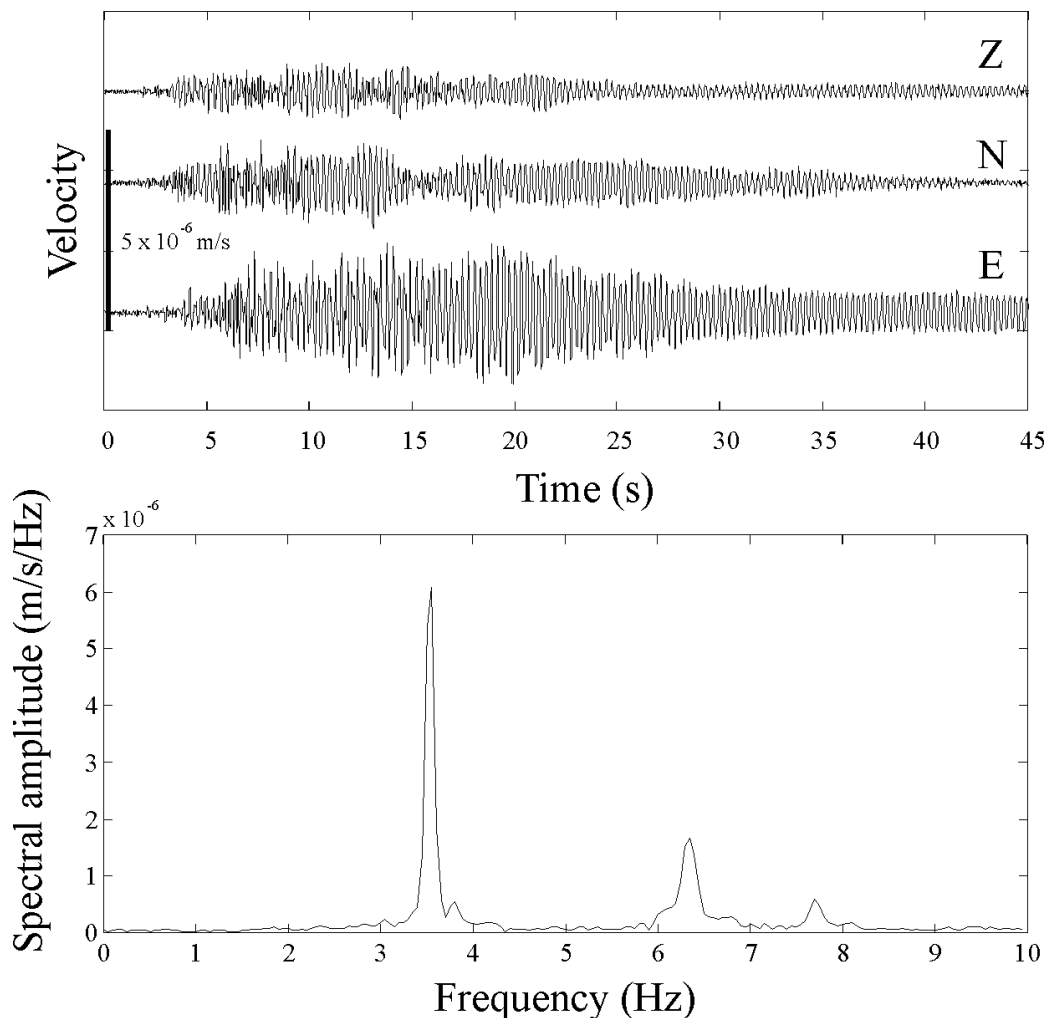


Figure 2.7 Lascar tornillo. (top) Seismograms of a tornillo (onset time: 16 April 1994, 15:43:26 UTC) recorded at station LA1. The amplitude scale is marked by a bar on the left. (bottom) Spectrum of the tornillo from the E component of the recording at LA1.

Since the events are all located within a small volume, the path to a given station, $g(t)$, is nearly the same for all wavegroups. We can therefore describe the source excitation for event n as:

$$s_n(t) = A_n s_0(t) \quad (2.4)$$

where $s_0(t)$, the characteristic source function for RF-events, is independent of their size.

The time dependence of the event source excitation is independent of its energy and a general source function exists which, apart from an amplitude factor, A_n , can describe all RF-events. This is unlike tectonic events, where the waveform and spectral content depend on the energy released. It is therefore unlikely that the RF-events are tectonic-type events produced by rock fractures in the solid volcanic edifice. Rather, they must be generated as an interaction or movement of volcanic fluids, magma, water or gases. They may, for example, be caused by nearly instantaneously heating of water or other gases which then expand explosively.

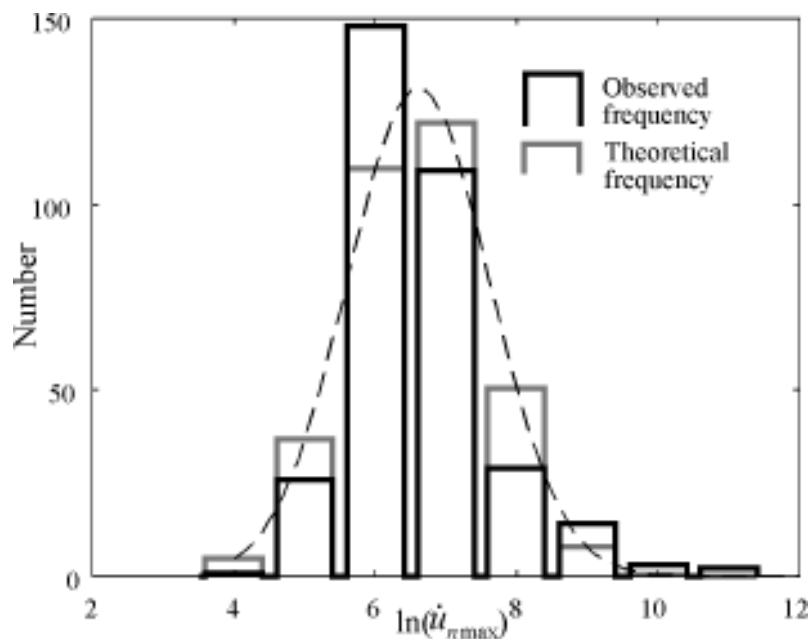


Figure 2.6 Histogram of the natural logarithm of the maximum RF-event amplitude, $\ln(i_{n\max})$. The histogram is compared with the best-fitting normal distribution.

log-normally distributed variables are the sizes of bubbles or amounts of monthly rainfall. RF-events must stem from a similar process.

We can synthesize these observations to better define RF-tremor. Since the spectra of small and large events are similar [ASCH *et al*, 1996], they can be described by a single function which varies only in amplitude. Thus, the linear correlation between $\log(\dot{u}_{\max})$ and $\log(E_{nT})$ suggests that the n th rapid-fire event can be described as:

$$\dot{u}_n(t) = A_n \dot{u}(t), \quad (2.2)$$

where $\dot{u}(t)$ is a characteristic function of time for all wavegroups and A_n is an amplitude factor determined by the event energy E_{nT} . An event n recorded at given seismometer site can also be described as a convolution between the source-time-function, $s_n(t)$, and the response function of the medium between the source and the station, $g(t)$,

$$\dot{u}_n(t) = s_n(t) * g(t). \quad (2.3)$$

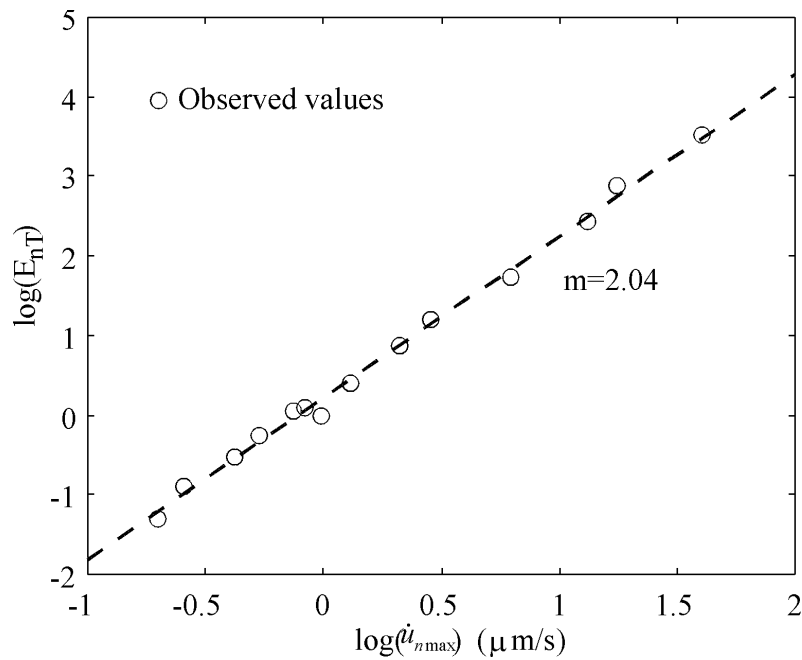


Figure 2.5 Relationship between $\dot{u}_{n\max}$ and the total RF-event energy E_{nT} . The slope of the dashed line, $m=2.04$, gives the exponent in the relationship in Equation 2.1

and the next in the RF-tremor sequence. The intervals between RF-events conform to a Poisson distribution, with the Poisson parameter $\lambda = 117$ s. This suggests that although the RF-events often appear to be almost continuous, they are independent of each other. That is, the occurrence of an individual RF-event is not influenced by previous events.

In Figure 2.5 the total signal energy, E_{nT} , for several events is plotted as a function of the events' maximum velocity amplitude, $\dot{u}_{n\max}$, in a log-log representation. E_{nT} is calculated as the integral of the square of the velocity over the entire event, while $\dot{u}_{n\max}$ is measured as the maximum amplitude from the instrument-corrected seismograms. The least-squares fit line for this data has a slope of 2.04. This indicates that

$$E_{nT} \propto \dot{u}_{n\max}^2. \quad (2.1)$$

Thus, the maximum ground velocity of an RF-event can be used as an indicator for its total energy, and the distribution of event energies can be deduced from the distribution of event amplitudes. Because of this relationship, a histogram of the maximum velocity amplitude (Fig. 2.6) gives the distribution of the events' energies. These are distributed log-normally, which is confirmed by χ^2 -testing. In general, variables which are distributed log-normally are the product of growth processes [TAUBENHEIM, 1969]. Typical examples of

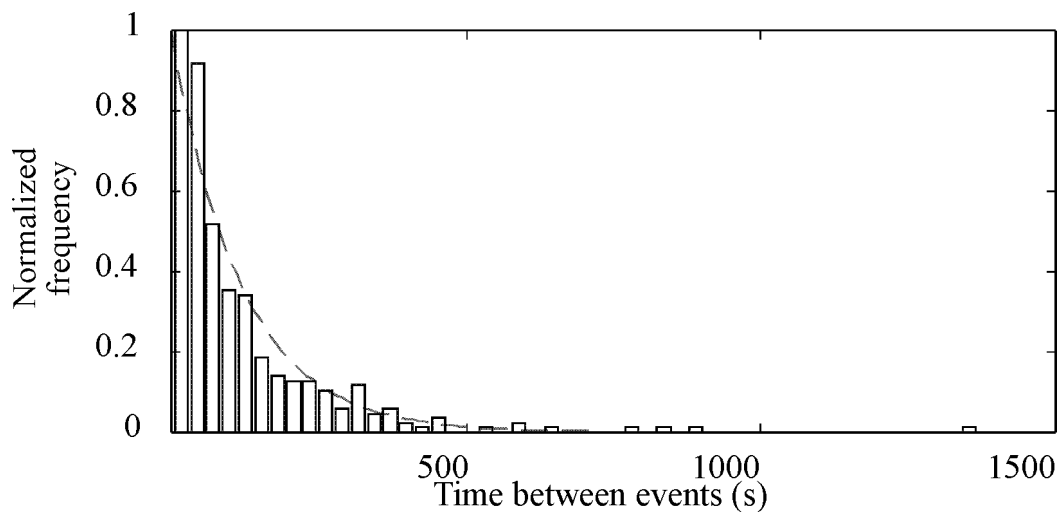


Figure 2.4 Histogram of intervals between RF-events. The dashed line shows the amplitude of a Poisson distribution with $\lambda = 117$ s.

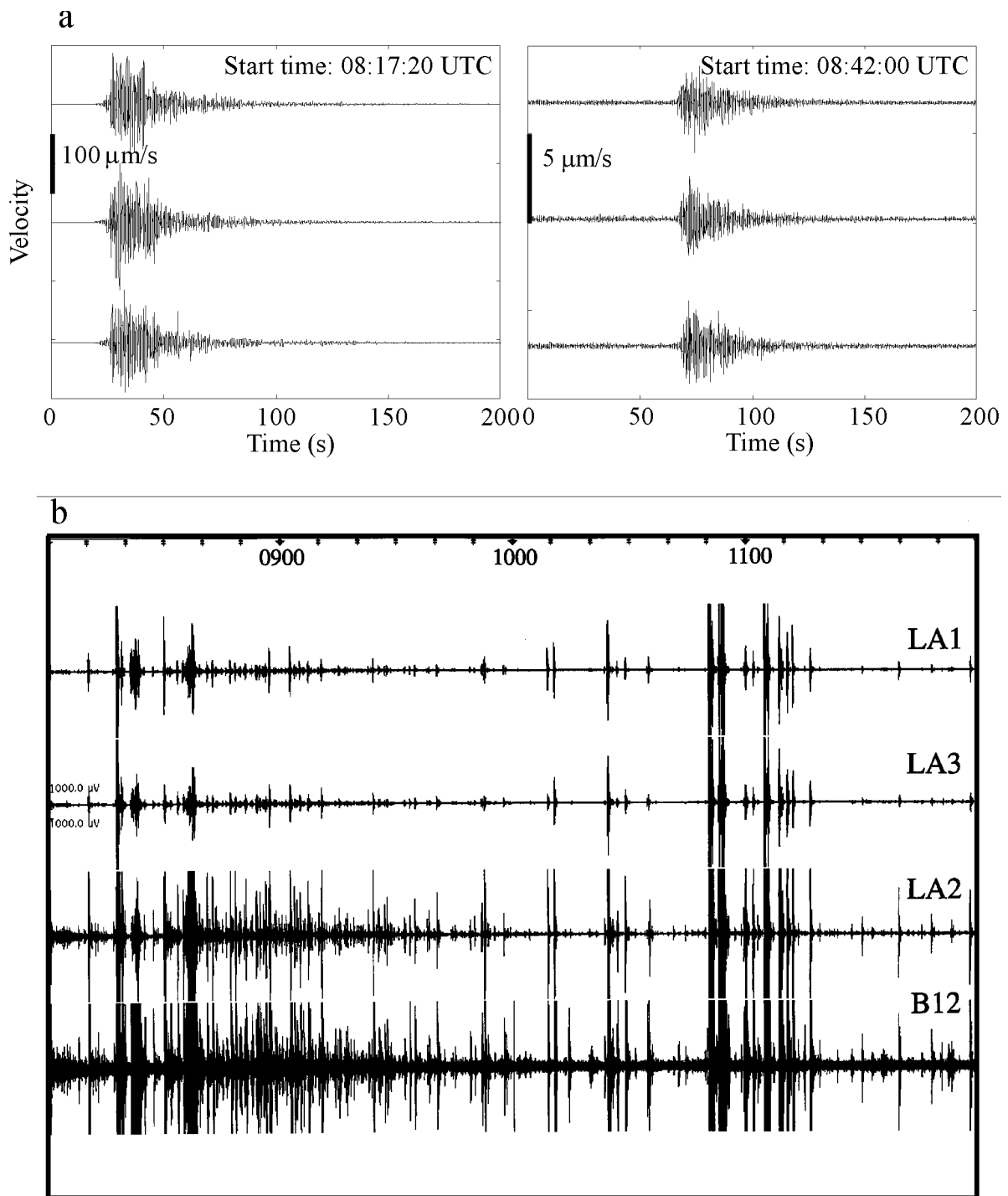


Figure 2.3 a) Three-component seismograms of two rapid-fire events of different amplitudes. b) Seismograms of the vertical components from the Lascar network from 08:00 to 12:00 UTC during the episode of RF-tremor on 6 May 1994. In this rendition, the largest events are clipped on all traces, so that small events can also be seen. The recordings show a 'rapid-fire', random series of events with very large dynamic range.

2.3 Characteristic Seismic Signals of Lascar Volcano

An active volcano produces many different types of seismic signals. These signals are measurable symptoms of its internal physical processes. Observations made from recordings of these signals can be used as a basis for modelling their sources.

In addition to the regional events recorded with the entire PISCO network during its deployment, the Lascar network recorded many events and episodes of tremor of the types typically observed at volcanoes. However, the recordings also captured several less common, but highly interesting volcanic seismic signals. Perhaps one of these signals will provide new insights into physical source processes, and thereby improve our understanding of how volcanoes work.

2.3.1 Rapid Fire Tremor

The seismic wavefield generated by Lascar Volcano during the PISCO'94 measurements often included a type of signal that has not been observed at many volcanoes. This tremor consists of an irregular sequence of event-like wavegroups with amplitudes that vary by several orders of magnitude. Often they occur so frequently that they appear to be almost continuous. Since HILL *et al.* [1990] report similar activity at Long Valley Caldera (California) which they describe as a sequence of "rapid-fire events", I will call this type of signal rapid fire tremor (RF-tremor). On 6 May, during a particularly intense episode of RF-tremor at Lascar more than 1300 RF-events occurred during a twelve hour interval (Figure 2.3). ASCH *et al.* [1996] analyzed data from this episode. They showed that the spectra of the individual event-like wavegroups making up RF-tremor (RF-events) have peaks at many of the same frequencies at all stations, indicating that the frequencies are a characteristic of the source. RF-events differing in amplitude by a factor of 100 also have some of the same frequencies, which means they are probably generated by the same mechanism within a small volume. ASCH *et al.* [1996] determined that three of the largest events were located near the active crater.

Figure 2.4 shows the distribution of the length of the time interval between RF-event-onsets. These data are calculated as the difference between the onset times of one event

Although the instruments of the Lascar network were deployed for only five weeks, the data set it produced differs fundamentally from many prior seismological observations at volcanoes. It has

- continuous, digital recordings for an extended period of time,
- three components at each site, and
- data with a high dynamic range.

In addition, the data from the broadband station, B12, provide information on the complete bandwidth of signals generated by Lascar.

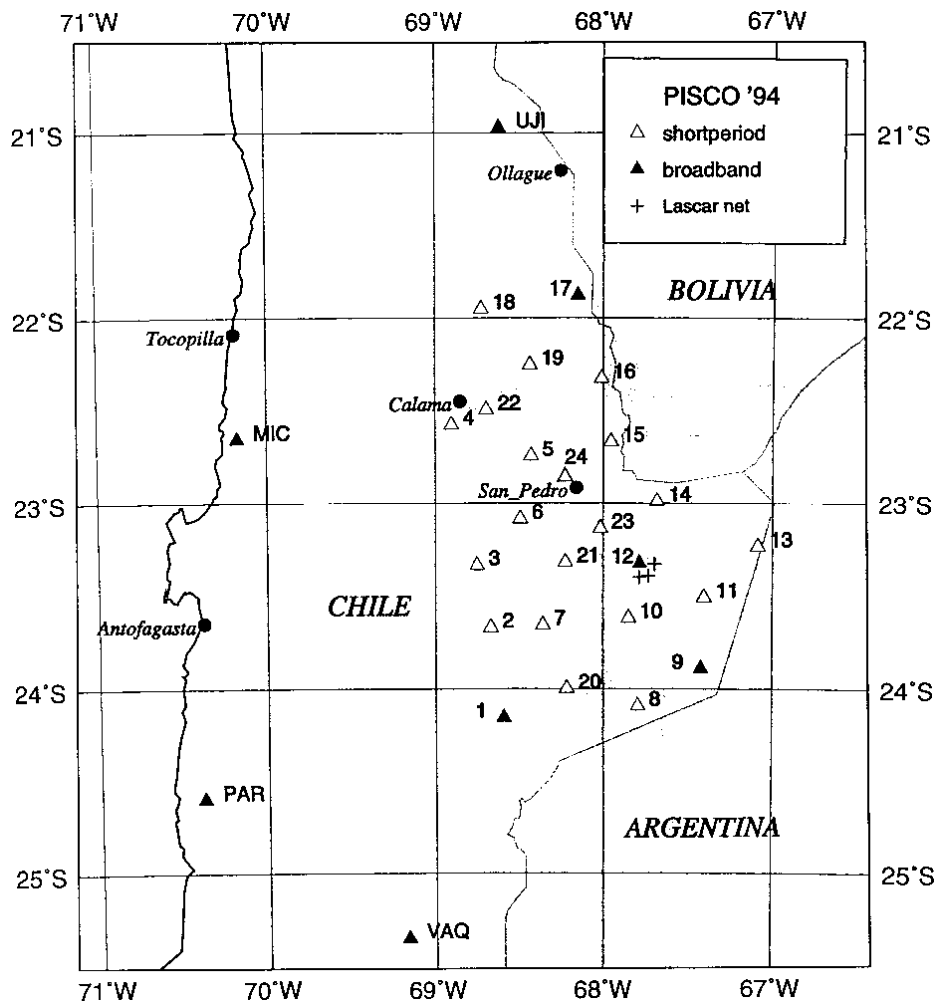


Figure 2.2 Seismic network of the PISCO'94 deployment. Lascar volcano is located near station 12. The short period stations of the Lascar network are marked by (+).

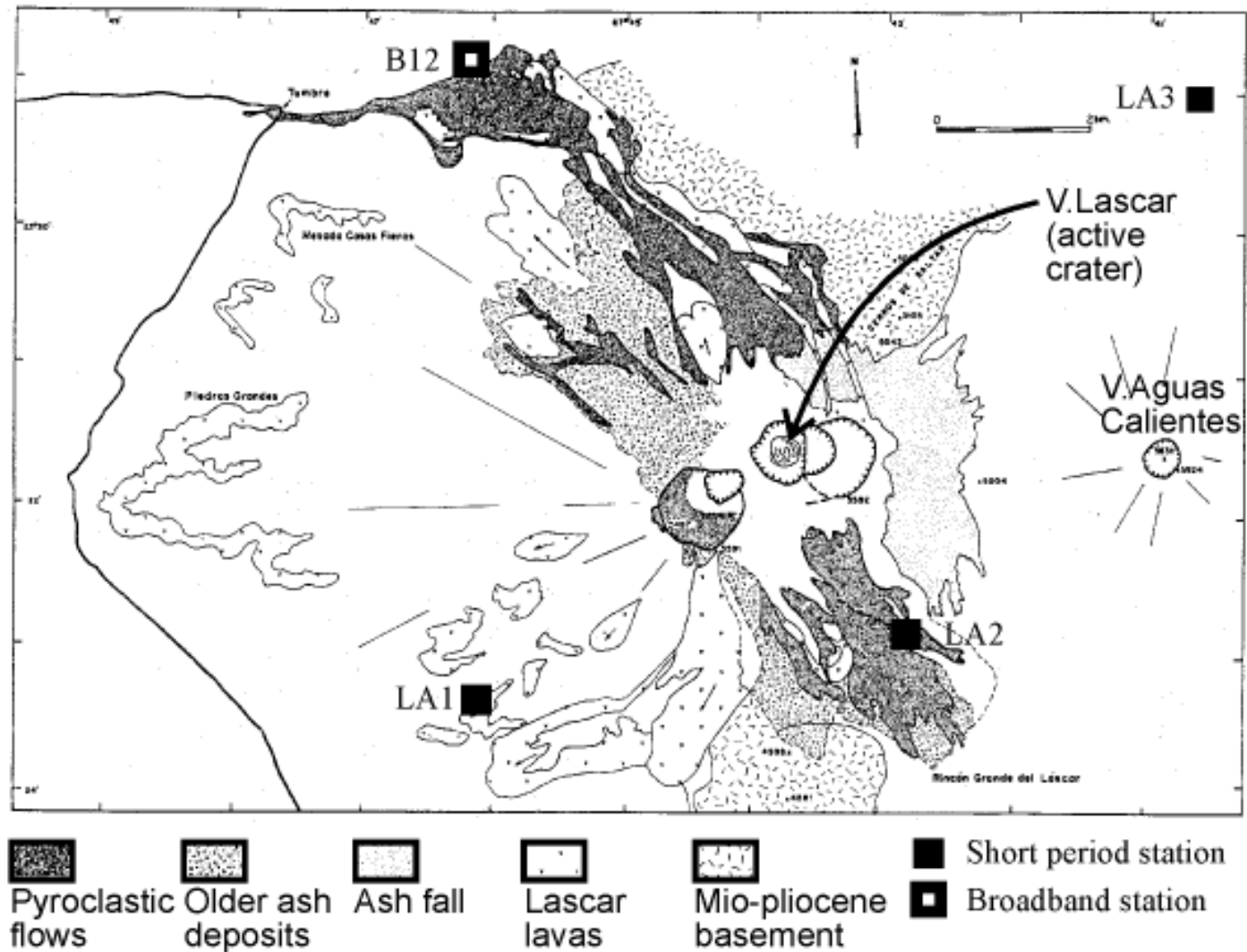


Figure 2.1 Map of the volcano Lascar with the stations of the Lascar network. The active crater is indicated by an arrow. Reproduced with the permission of Dr. Moyra Gardeweg, SERINGEOMIN, Chile.

map the subducting slab (Figure 2.2). The network included twenty shortperiod, three-component seismometers (L-4C), four STS-2 and four CMG-3 broadband instruments. Digital data were recorded continuously at all stations. The deployment was part of the German Research Foundation Collaborative Research Program (SFB) 267, “*Deformationsprozesse in den Anden*”.

Station B12 of the PISCO network was a STS-2 seismometer installed about 6.4 km from the active crater on the NW flank of the volcano Lascar (Figure 2.1, Table 1). In April 1994, three additional shortperiod, three-component seismometers were deployed to the SW, SSE and NE of the volcano (LA1, LA2 and LA3, Table 1). Continuous data were recorded digitally on local hard disks using PDAS recorders in gain-ranging mode (140 dB dynamic range). As the data were recorded at sampling rates of 200 Hz (100 Hz for station B12), the disks were replaced every three days, and the data were archived on CDRoms. The four stations operated from 8 April until 12 May 1994 (Julian days 98 - 132).

Table 1

Station	Coordinates	Site Geology ¹	Dist/Az to Crater	Sensor		Gen. Constant (Vs/m)
B12 100 Hz	3950 m	At edge of lava flow in ash/tephra	6.4 km	STS-2	Z	1500
	23°19'27" S		128°		N	1500
	67°46'43" W				E	1500
LA1 200 Hz	4000 m	On E flank of a valley near old lava flow, buried in ash/tephra	6.7 km	L4	Z	272
	23°23'55" S		49°		N	280
	67°46'42" W				E	285
LA2 200 Hz	4750 m	Near wall of welded tuff protected by large boulder, in ash/tephra	3.5 km	L4	Z	275
	23°23'25" S		352°		N	285
	67°43'27" W				E	284
LA3 200 Hz	4700 m	Buried in ash/tephra plain	5.5 km	L4	Z	284
	23°19'43" S		231°		N	276
	67°41'14" W				E	279

1 A. Rudloff, personal communication

2 Lascar Volcano: The Wavefield

2.1 The Volcano

Lascar, a stratovolcano more than 5000 m in altitude, is located on the puna, Chile's altiplano, at 23° 22' S, 67° 44' W. GARDEWEG and MEDINA [1994] note that it is the most active volcano in northern Chile. Reports of Lascar's activity begin in the sixteenth century with the arrival of the Spanish in the region and continue until the present. Its activity is mainly fumarolic, although the continuous degassing is occasionally interrupted by large explosions from the various craters in the summit region. Since 1986, Lascar has undergone several cycles of lava dome growth and collapse. The growth phases usually last several months and are accompanied by numerous small explosions.

On 19 April 1993, a dome growth phase culminated in the largest historically recorded eruption of Lascar [Bulletin of the Global Volcanism Network (GVN), April, 1993, GARDEWEG and MEDINA, 1994]. After several hours of Vulcanian explosions, a series of Plinian eruptions generated ash columns and pyroclastic flows (Figure 2.1). Declining activity was followed on 20 April 1993 by an additional explosion and the formation of a new ash column. In the course of the following month, the activity decreased until it reached the usual level of continuous fumarolic activity with high levels of SO₂ emission. On the average, Lascar emits about 2400 Mg/day SO₂ [ANDRES and KASGNOC, 1998].

On 17 December 1993 another, smaller eruption occurred [GVN, March, 1994]. Afterwards, the activity decreased to normal levels within several hours. As observed from San Pedro de Atacama between January and May 1994, Lascar's activity was limited to the emission of steam and SO₂ [G. ASCH, personal communication]. Despite its low level of activity during this period, Lascar produced many interesting and unusual seismic signals.

2.2 The Measurements

In early 1994 ASCH et al [1995, 1996] installed a network of seismometers in northern Chile as part of the "Proyecto de Investigación Sismológica de la Cordillera Occidental '94" (PISCO'94). The instruments were deployed in an area between 19.5° S and 25.5° S and between the coastal cordillera and the puna in order to study the region's seismicity and

3 Harmonic Tremor: Analysis

As other volcanic seismic signals, harmonic tremor at Lascar must be generated by some physical or chemical process in the volcano. What and where is its source? How are the seismic waves generated by the source affected by their path through the volcano? What does it tell us about the physics of volcanoes? Because the Lascar recordings have a high signal-to-noise ratio, they can be analyzed using standard seismological methods, as well as methods from other fields. The results of this analysis may then serve as the basis for a physical model for the source of harmonic tremor.

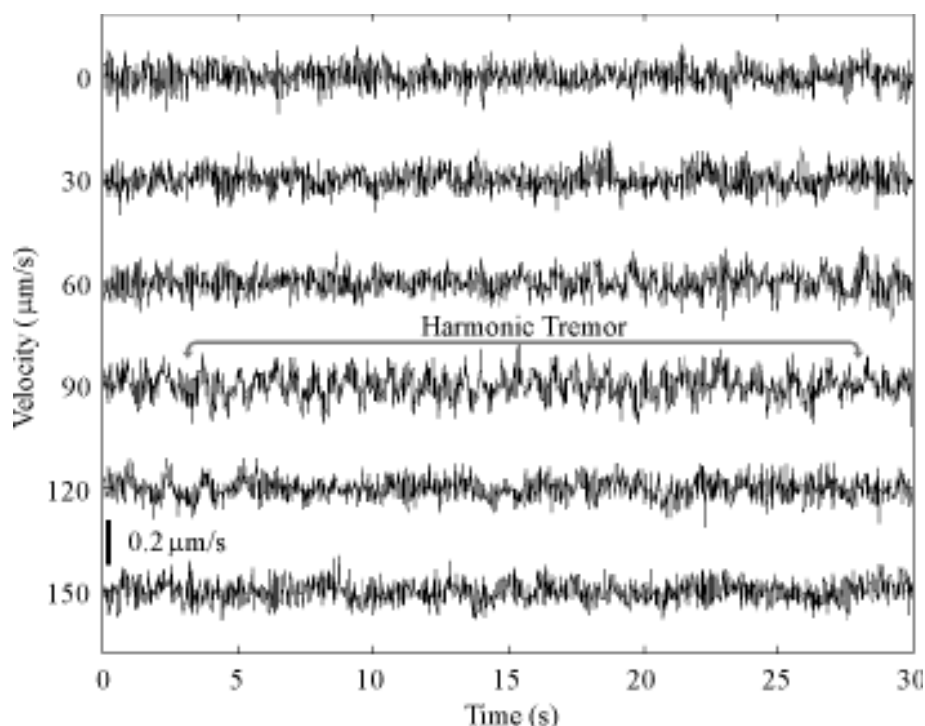


Figure 3.1 Beginning of harmonic tremor. 180 s of the recording of the E component at station LA2 are plotted like a helicorder record. In the 25 s long segment beginning at second 93 which is marked by a bracket, there is a hint of an 0.7 Hz oscillation which differs from the surrounding noise. The interval begins on 18 April 1994 at 01:36:00 UTC. The bar on the lower left shows the amplitude scale.

3.1 Seismograms

3.1.1 Waveforms

At its beginning, harmonic tremor slowly rises above the normal seismic noise signal (Figure 3.1). As is the case with other types of tremor, there is no clear onset. In the

marked segment at 93 s, an oscillation is apparent which differs from the usual noise and lasts about 25 s. About 19 min later, the cycles which are harmonic tremor become clearly recognizable in the seismogram (Figure 3.2).

The cycles of the harmonic tremor can be seen clearly on all stations and components of the Lascar network (Figure 2.11). The period of the cycles is the same at all stations, only the signal shape varies from station to station and component to component.

3.1.2 Amplitudes

AKI and RICHARDS [1980] give the following relationship between the i th component of the displacement wavefield for body waves, $u_i(\mathbf{x}, t)$, and a point force in the j direction, $F_0(t)$, if the medium is elastic and there is neither scattering nor absorption:

$$u_i(\mathbf{x}, t) = \frac{1}{4\pi\rho} (3\gamma_i\gamma_j - \delta_{ij}) \frac{1}{r^3} \int_{r/\alpha}^{r/\beta} \tau F_0(t - \tau) d\tau + \frac{1}{4\pi\rho\alpha^2} \gamma_i\gamma_j \frac{1}{r} F_0(t - r/\alpha) - \frac{1}{4\pi\rho\beta^2} (\gamma_i\gamma_j - \delta_{ij}) \frac{1}{r} F_0(t - r/\beta) \quad (3.1)$$

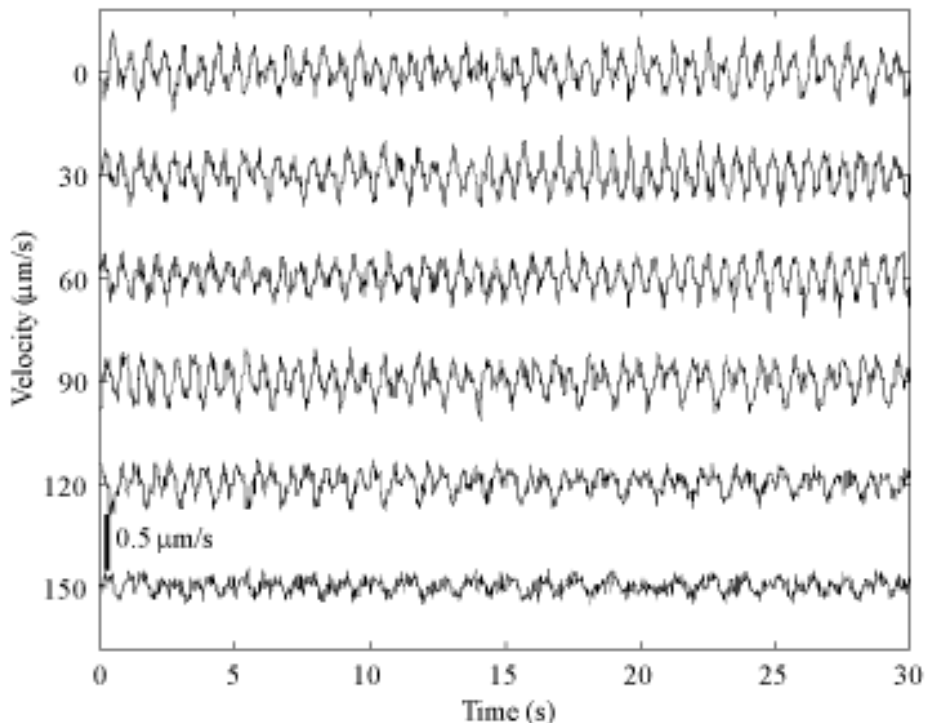


Figure 3.2 Typical 180 s long segment of harmonic Tremor on the recordings of the E component at station LA2. This interval begins at 01:55:00 UTC on 18 April 1994. The bar on the lower left shows the amplitude scale.

In this equation, γ_i and γ_j are the directional cosines and δ_{ij} is the Kronecker delta function, while ρ , α and β are the density of the medium and its P and S wave velocities, respectively. The first term decreases in amplitude with $1/r^3$, so it gives the displacement in the near field. The second and third terms describe the far-field ground motion due to the P and S waves, respectively.

For harmonic tremor, the peak-to-peak ground velocity is about 4×10^{-7} m/s at the station closest to the active crater, LA2, and lower at the other, more distant stations (Figure 2.11). The peak-to-peak ground displacement at station LA2 is about 6×10^{-8} m. This value can be used in Equation 3.1 to estimate the amplitude of a point force at the origin. For this calculation, I assume that the medium has the density of andesite, $\rho = 2.8 \times 10^3$ kg/m³ [MURASE and MCBIRNEY, 1973], and that the factors containing the directional cosines have their maximum value, $\gamma_i, \gamma_j = 1$. For each station, r is taken to be the horizontal distance from the crater to the station. If the wavefield at the station consists

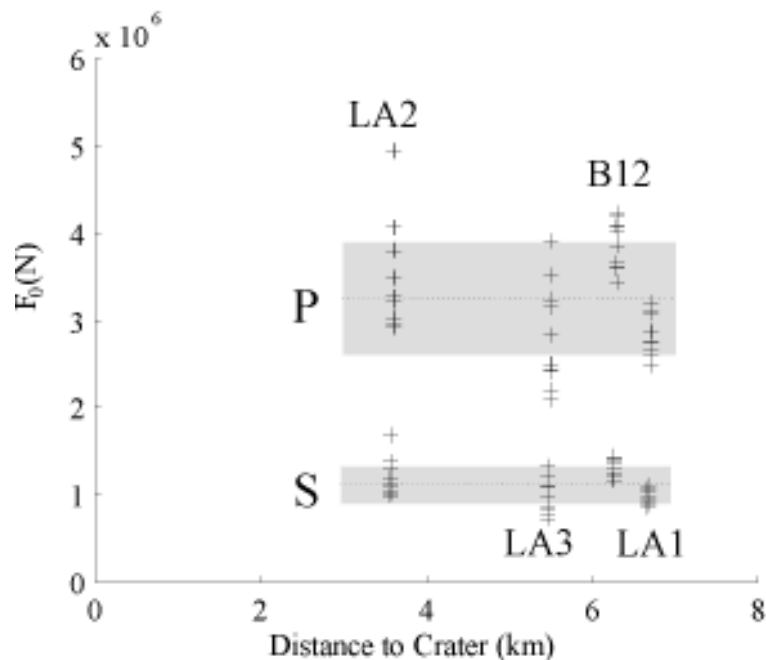


Figure 3.3 Magnitude of a point force necessary to generate recorded seismograms for P and S waves. The force is calculated from 40 s windows of the 400 s interval starting at 02:38:20 UTC on 18 April 1994 using Eq. 3.1. The dotted lines indicate the means, and the vertical extent of the shaded rectangles give the standard deviations.

only of P waves in the farfield, propagating at a velocity $\alpha = 1000$ m/s, the force necessary to generate the ground displacement due to harmonic tremor at the stations can be estimated using the second term in Equation 3.1. Mean values for F_{0P} , calculated for 40 s windows of data, are plotted in Figure 3.3 for each station along with their average $F_{0P} = 3.2 \times 10^6$ N. This figure also shows the values of F_{0S} for a wavefield of S waves ($\beta = 580$ m/s). In this case, the force at the origin is smaller, $F_{0S} = 1.1 \times 10^6$ N. Variations in the velocity of the medium or near-field effects may increase the estimated amplitude of the force. On the other hand, contributions from other factors, such as greater source depth or absorption in the medium, would cause the amplitude to decay more rapidly with distance than described by Equation 3.1. The source would then have to produce more seismic energy to generate the measured ground motion.

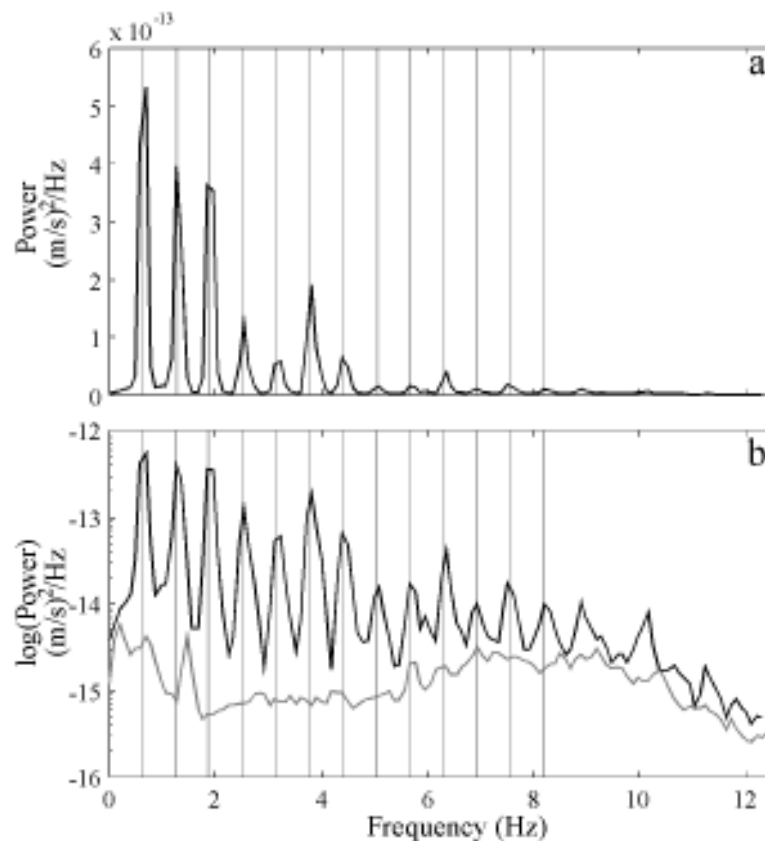


Figure 3.4 Power spectrum of a 10 minute interval of harmonic tremor beginning on 18 April 1994 at 02:35:00 UTC recorded on the E component of station LA2. The spectrum was calculated using 10.24 s windows and 50% overlapping. The vertical lines are drawn at multiples of the frequency of the first peak, 0.63 Hz. (a) Linear plot. (b) Semilog representations. The gray line shows the power spectrum for the 10 minute seismogram segment just before harmonic tremor begins (01:30 UTC).

3.2 Spectra and Spectrograms

3.2.1 Powerspectra

In a linear representation of the power spectrum of harmonic tremor (Figure 3.4a), seven spectral peaks are visible. The frequencies of these peaks are integer multiples of the frequency of the fundamental, $f_1 = 0.63$ Hz. Spectral peaks of order higher than seven which are only hinted at in Figure 3.4a are visible in the logarithmic representation in Figure 3.4b. Here at least 14 peaks are present which can be described by the equation $f_n = nf_1$. In Figure 3.4b the power spectrum of the background tremor shortly before the beginning harmonic tremor is also plotted (gray). Its spectrum is everywhere lower than

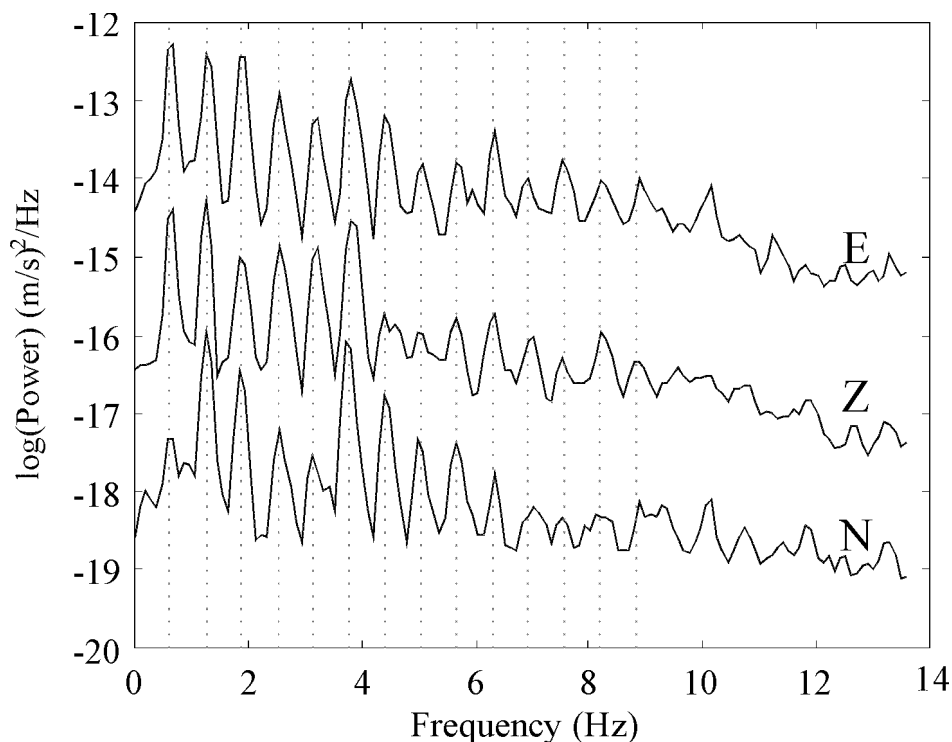


Figure 3.5 Semilog plot of power spectra calculated for the three components of station LA2. The data interval, windows and overlap are the same as Figure 3.4. Spectra for the Z and N components are offset by two and four orders of magnitude to improve viewing. The vertical lines are drawn at multiples of the frequency of the first peak, 0.63 Hz.

the spectrum of the harmonic tremor and it has none of the spectral peaks present in the harmonic tremor.

The logarithmic representation of the power spectra for the three components of station LA2 demonstrates that the Z, N and E components measure signals with the same frequencies but very different amplitudes (Figure 3.5). The same spectral lines are also present in the seismograms recorded at the other stations (Figure 3.6). At all stations the lines up to order seven are between 10 and 20 dB above the noise level. Spectral lines of higher order are only 5 dB above the noise with still lower amplitudes at the more distant stations, LA1 and LA3.

3.2.2 Spectrograms

Spectra (Figures 3.4, 3.5 and 3.6) can only show average values of a signal's amplitude, because they are calculated for an interval of a time series, rather than an instant. In addition, power spectra are usually calculated by averaging over several individual spectra.

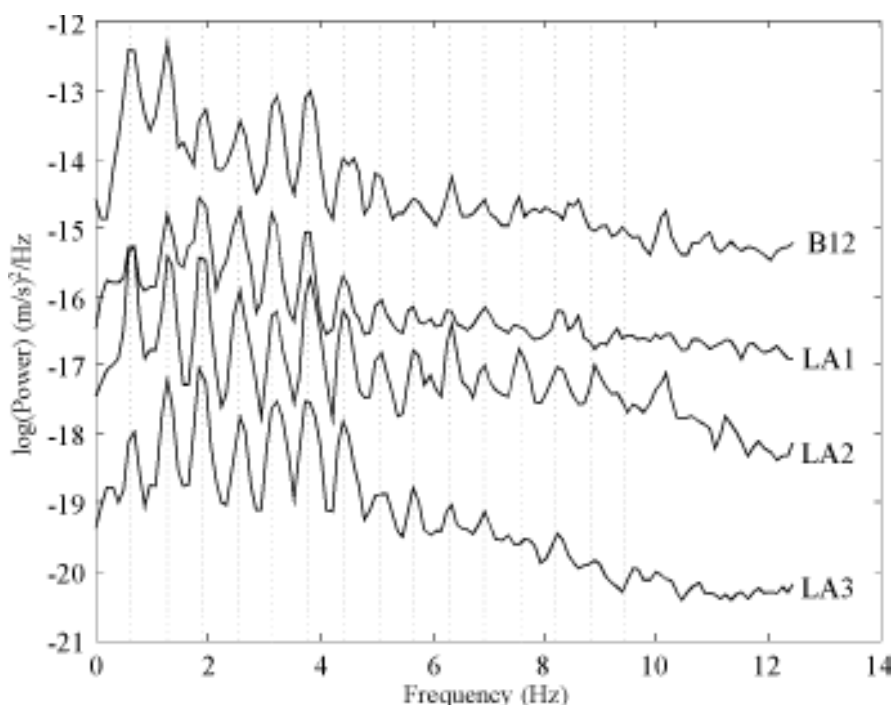


Figure 3.6 Semilog plot of power spectra calculated for the E components of all stations. The data interval, windows and overlap are the same as Figure 3.4. Spectra of LA1, LA2 and LA3 are shifted vertically to improve viewing. The vertical lines are drawn at multiples of the frequency of the first peak, 0.63 Hz.

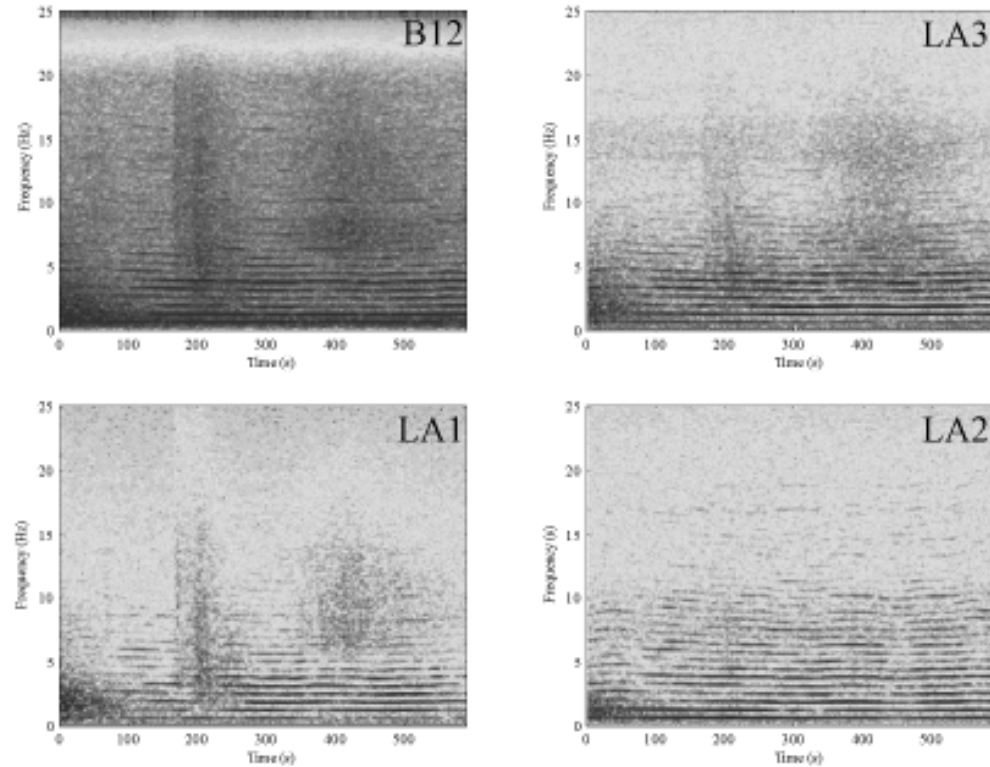
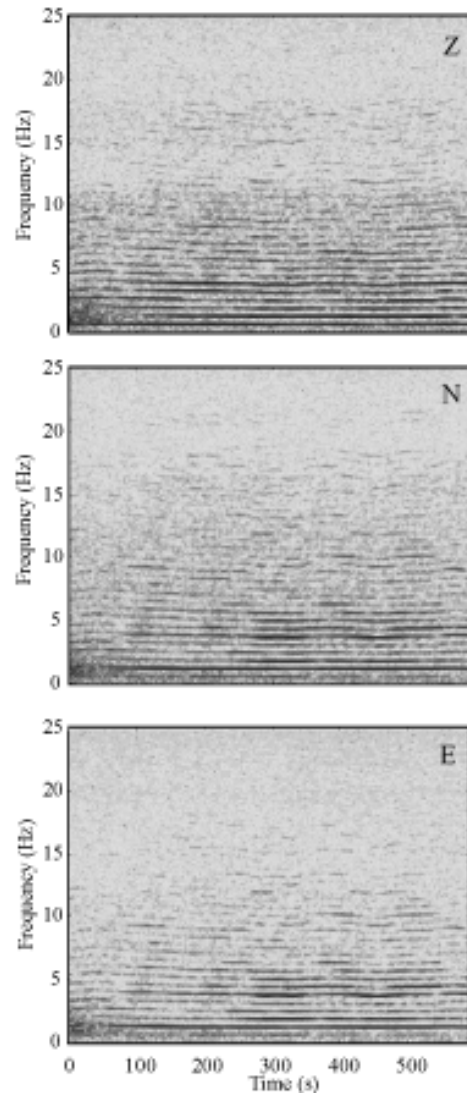


Figure 3.7 Spectrograms of data recorded on the Z, N and E components at station LA2 for the interval used in Figure 3.4. Each spectral window is 10.24 s long, and overlapped by 8.96 s.

Figure 3.8 Spectrograms of the E components of all four stations of the Lascar network for the interval used in Figure 3.4. They were calculated in the same way as Figure 3.7.

In the analysis of tremor which continues for long periods of time, it is desirable to be able to observe changes in the spectrum as a function of time. Spectrograms allow the representation of the time-dependence of the frequency of a signal. In such plots, the spectral amplitude is usually indicated by color or shading. In a spectrogram representation of the harmonic tremor at Lascar (Figure 2.12), frequency changes are recognizable at 3000 s, 5800 s and 6500 s. At the station nearest to Lascar's crater, LA2, the spectrograms of the components (Figure 3.7) show more than 25 harmonics. The frequency characteristics of the tremor can be recognized on all components (Figure 3.7) and at all stations (Figure 3.8). Changes in the frequency observed at Station LA2 occur at the same time at the other stations. This observation leads to the conclusion that such changes are produced at the source and are not caused by characteristics of the path or station site.

3.2.3 Phasograms

Volcanic tremor can be distinguished from seismic events by the fact that its source or sources are continuously active over long periods of time. Thus, it makes little sense to search a tremor recording for the changes in amplitude and and frequency that signal the arrival of seismic phases. On the other hand, the presence and behavior of narrowband signals in tremor can be resolved using complex demodulation.

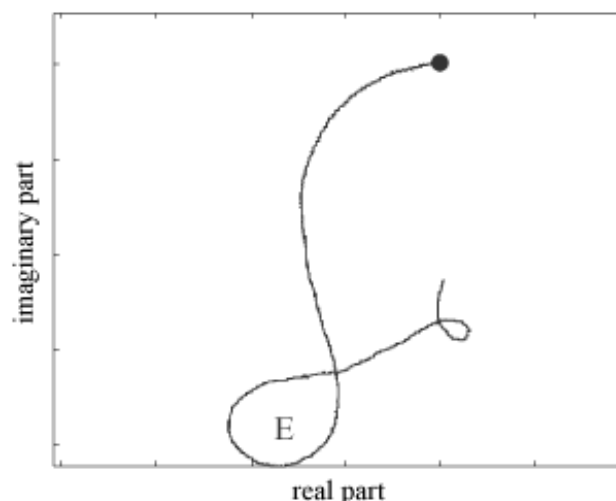


Figure 3.9 Phasogram for the fundamental recorded on the E component at station LA2. The test frequency is $f_0 = 0.63$ Hz. A bandpass filter with corner frequencies at 0.5 and 0.9 Hz was applied to the data before the phasogram was calculated. $t = 0$ is indicated by the dot.

In the method of “phasor walk-outs” — or phasorgrams — described by ZÜRN and RYDELEK [1994], the Fourier transform $X(f_0, n)$ of a time series $x(k\Delta t)$ is calculated not, as is usual, for all frequencies f , but only for a “test frequency” f_0 ,

$$X(f_0, n) = C \sum_{k=1}^n x(k\Delta t) \cdot e^{-2\pi i f_0 k \Delta t}, \quad (3.2)$$

where C is a scaling factor. The complex function $X(f_0, n)$ is then plotted in the complex plane. In the resulting diagram, very weak, narrowband signals at or near the test frequency can be recognized, as well as changes in the frequency of the signal or phase jumps [ZÜRN and RYDELEK, 1994]. The radius of curvature is an indication for the difference between the test frequency and the frequency of the signal. As a general rule, the smaller the radius of curvature, the farther the signal frequency is from the test frequency.

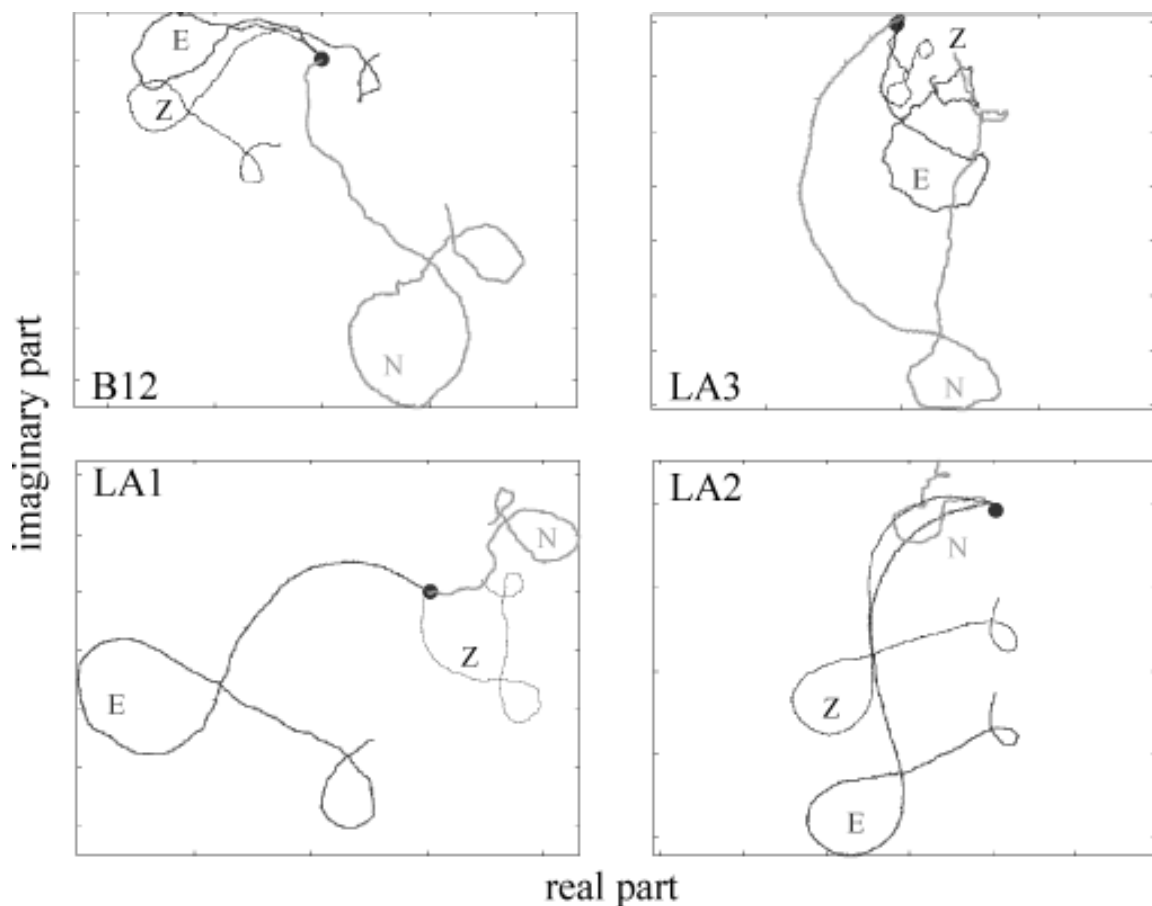


Figure 3.10 Phasorgram as in Figure 3.9 for all components at all stations. $t = 0$ is indicated by the dot.

As an example, I calculate the phasogram for a 2 minute interval of the bandpass filtered data (0.5-0.9 Hz) for the E component at station LA2 (Figure 3.9). The test frequency, $f_0 = 0.63$ Hz, corresponds to the maximum of the peak for the fundamental in the power spectrum. The variation in the radius of curvature of the phasogram curve shows the deviation of the frequency of the tremor from the test frequency. The curve begins with a large arc, indicating that the tremor frequency is close to f_0 . The next segment is nearly straight, so the tremor frequency is exactly 0.63 Hz. In the following section (around the letter E), the radius of curvature is much smaller than for the first interval. At the end of the phasogram another straight segment is followed by a very small loop, where the tremor frequency has drifted quite far from the test frequency. As indicated by these plots, the tremor frequency varies continuously and smoothly.

The individual phasograms for the three components at the station LA2 (Figure 3.10, lower right) all show similar pattern of loops and straight segments, although their directions and amplitudes differ. This is not surprising, since the seismometer partitions the ground motion into three orthogonal directions which are arbitrarily related to the polarization of the oscillations. On the other hand, the phasograms at the other three stations are very similar to those at station LA2 (Figure 3.10). Although the polarizations of the oscillations at the four stations appear to be unrelated to each other (see section 3.4), the phasograms have the same pattern with an arc, followed by a straight section, a large loop, another straight section and finally a small loop. This similarity means that the frequency changes of harmonic tremor are independent of path and site.

3.3 The Reduced Instantaneous Phase

The Hilbert transform of a real function of time $x(t)$ is:

$$y(t) = H(x(t)) = \frac{1}{\pi} P \int_{-\infty}^{\infty} \frac{x(\xi)}{\xi - t} d\xi, \quad (3.3)$$

where, ξ is the variable of integration for the time and P is the principal value of the integral [BUTTKUS, 1991]. Adding this function to the original function as the imaginary part gives the

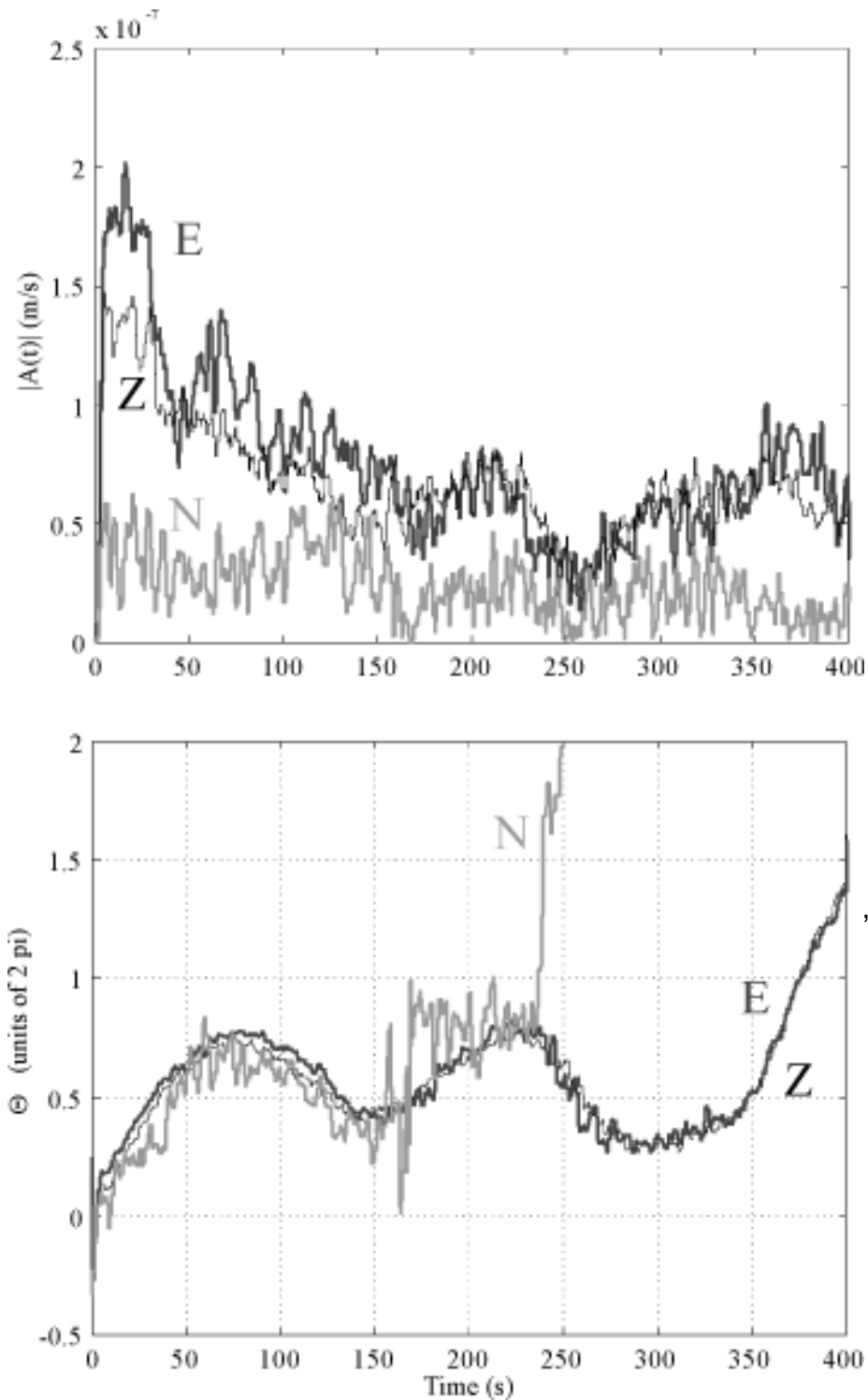


Figure 3.11 Hilbert transform of the fundamental at station LA2. Top: The instantaneous amplitude. Bottom: The reduced instantaneous phase Θ_R with $f_0 = 0.63$. A bandpass filter with corner frequencies at 0.5 and 0.9 Hz was applied to the data before the Hilbert transform was calculated. The data interval begins at 02:38:20 UTC on 18 April 1994.

analytic function, $z(t)$, which can also be expressed in terms of the instantaneous amplitude, $A(t)$, and the instantaneous phase, $\Theta(t)$:

$$z(t) = x(t) - iH(x(t)) = x(t) - iy(t) = A(t)e^{i\Theta(t)}. \quad (3.4)$$

In seismology this function may be used to determine the group and phase velocities of surface waves [DZIEWONSKI and HALES, 1972]. The Hilbert transform has also been applied to seismological data to determine arrival times and polarization (FARNBACH, 1975, VIDALE, 1986).

The time derivative of the instantaneous phase is the instantaneous angular frequency:

$$\omega(t) = 2\pi f(t) = \frac{d\Theta(t)}{dt}. \quad (3.5)$$

If $x(t)$ is a sine wave, $x(t) = \sin(2\pi f_0 t)$, then its Hilbert transform is $y(t) = \cos(2\pi f_0 t)$ and its instantaneous phase is a straight line with slope $2\pi f_0$. For narrowband signals we can use this fact to detect and measure even very small changes in the frequency. Let $s(t)$ be a recorded, sinusoidal signal with time varying amplitude, $A_1(t)$, and slowly changing frequency, $f(t)$,

$$s(t) = A_1(t) \sin(2\pi f(t)t). \quad (3.6)$$

If the changes of $f(t)$ around some value f_0 are small, they can be measured by plotting the reduced instantaneous phase ,

$$\Theta_R = \Theta(t) - 2\pi f_0 t, \quad (3.7)$$

as a function of time. When $f(t) = f_0$, the slope of Θ_R ,

$$m = 2\pi(f(t) - f_0), \quad (3.8)$$

will be zero. During intervals when $f(t)$ is constant, m is constant, and the slope of the reduced instantaneous phase changes when $f(t)$ changes.

While the phasorgrams described in Section 3.2.3 allow the qualitative analysis of the variations in the tremor frequency, the analytic function permits quantitative observations of

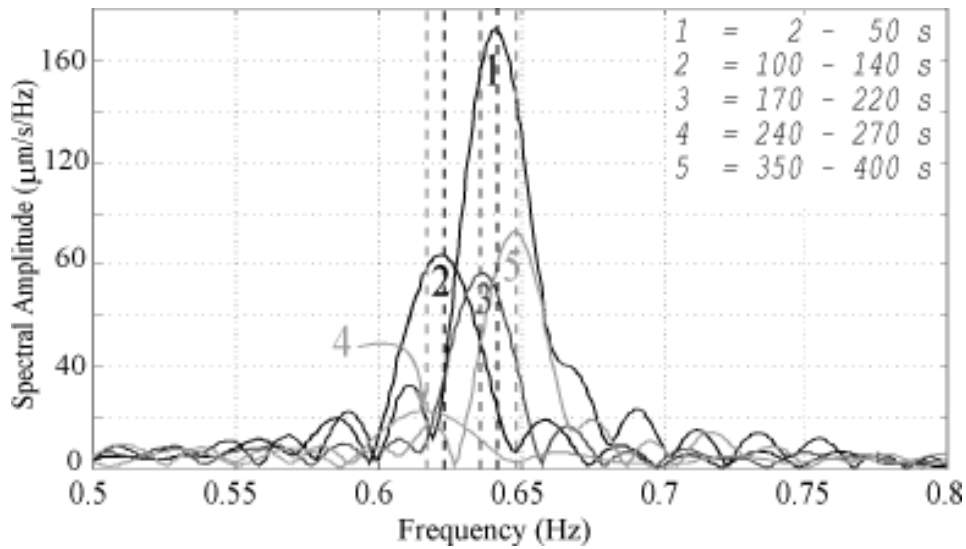


Figure 3.12 Determination of the exact frequency of the fundamental from the amplitude spectrum in five intervals. Before the spectra were calculated, zeros were appended to the data from each interval so that they were 50000 values long. The frequency separation of the spectral values is then 0.001 Hz. The vertical lines show the frequencies measured using the Θ_R .

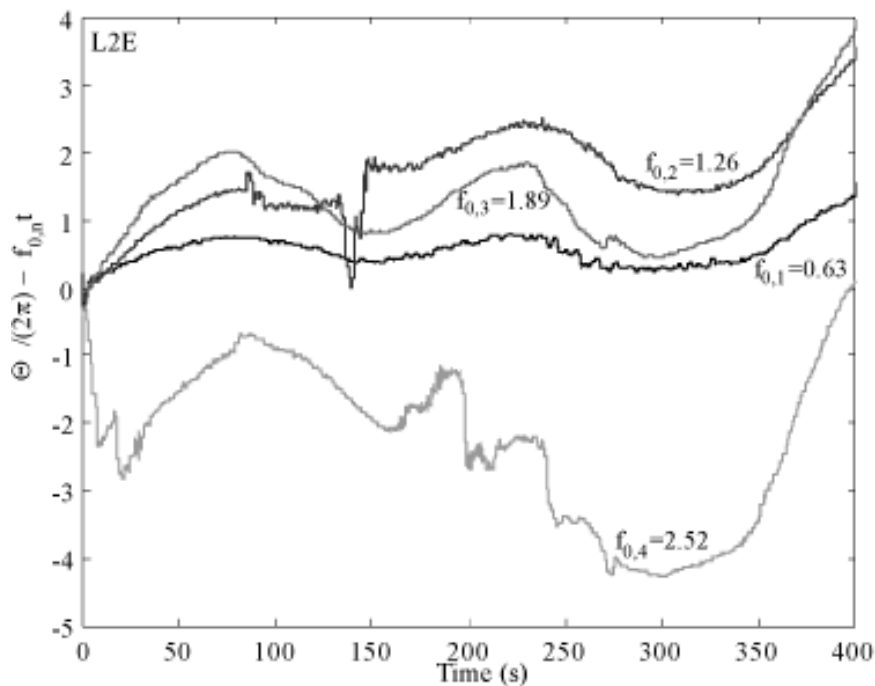


Figure 3.13 Comparison of the Θ_R for the first four harmonics at station LA2. Before calculating Θ_R , bandpass filters were applied to the data. The corner frequencies are: $n = 1$, 0.5-0.9 Hz; $n = 2$, 0.9-1.5 Hz; $n = 3$, 1.5-2.1 Hz; $n = 4$, 2.1-2.7 Hz. The test frequencies for each harmonic are given on the plot. The data interval begins at 02:38:20 UTC on 18 April 1994.

its changes. This is demonstrated in Figure 3.11 where the instantaneous amplitude (top) and Θ_R (bottom) are plotted for 400 s of the recording of the fundamental (bandpass filter 0.5-0.9 Hz) at LA2. Apart from very small variations, Θ_R for the Z and E components are the same. During the first 150 s, the N component is also similar to the other two components. It varies somewhat more because the signal-to-noise ratio (SNR) is much poorer than for Z and E. At 170 s the N component has several jumps of 2π . Here the SNR is low, so the instantaneous phase, $\Theta(t)$ is poorly defined. After a jump of 2π , the phase indicates the same location in the complex plane, so for the analysis of the reduced instantaneous phase, such jumps are of no consequence. Finally, after 240 s, the amplitude of the N component is so small that there are many jumps of 2π and the reduced instantaneous phase wanders out of the range of the figure.

For a quantitative analysis of the reduced instantaneous phase for the Z and E components, the curve in Figure 3.11 can be separated into five segments with relatively constant slope ($2 < t < 50$ s, $100 < t < 140$ s, $170 < t < 220$ s, $240 < t < 270$ s and $350 < t < 400$ s). Between these segments the slope changes radically. Using equation 3.8 I can calculate the deviation of the frequency of the fundamental from the test frequency, $f_0 = 0.63$ Hz. Table 2 gives the results with an accuracy of 0.001 Hz. The frequency for these intervals can also be measured from the maximum of the peak in the amplitude spectrum. In order to achieve an accuracy similar to that determined from Θ_R , the intervals had to be extended to 50000 data points (Figure 3.12). The frequencies, f_s , measured from the spectra agree very well with those determined by the analysis of Θ_R (Table 2).

Table 2 -- Tremor Frequency

Interval	Slope (1/s)	f_1 (Hz)	f_s (Hz)
2-50 s	0.0117 ± 0.0001	0.642	0.641
100-140 s	-0.0069 ± 0.0005	0.623	0.622
170-220 s	0.0065 ± 0.0004	0.636	0.636
240-270 s	-0.0108 ± 0.0023	0.617	0.617
350-400 s	0.0180 ± 0.0007	0.648	0.648

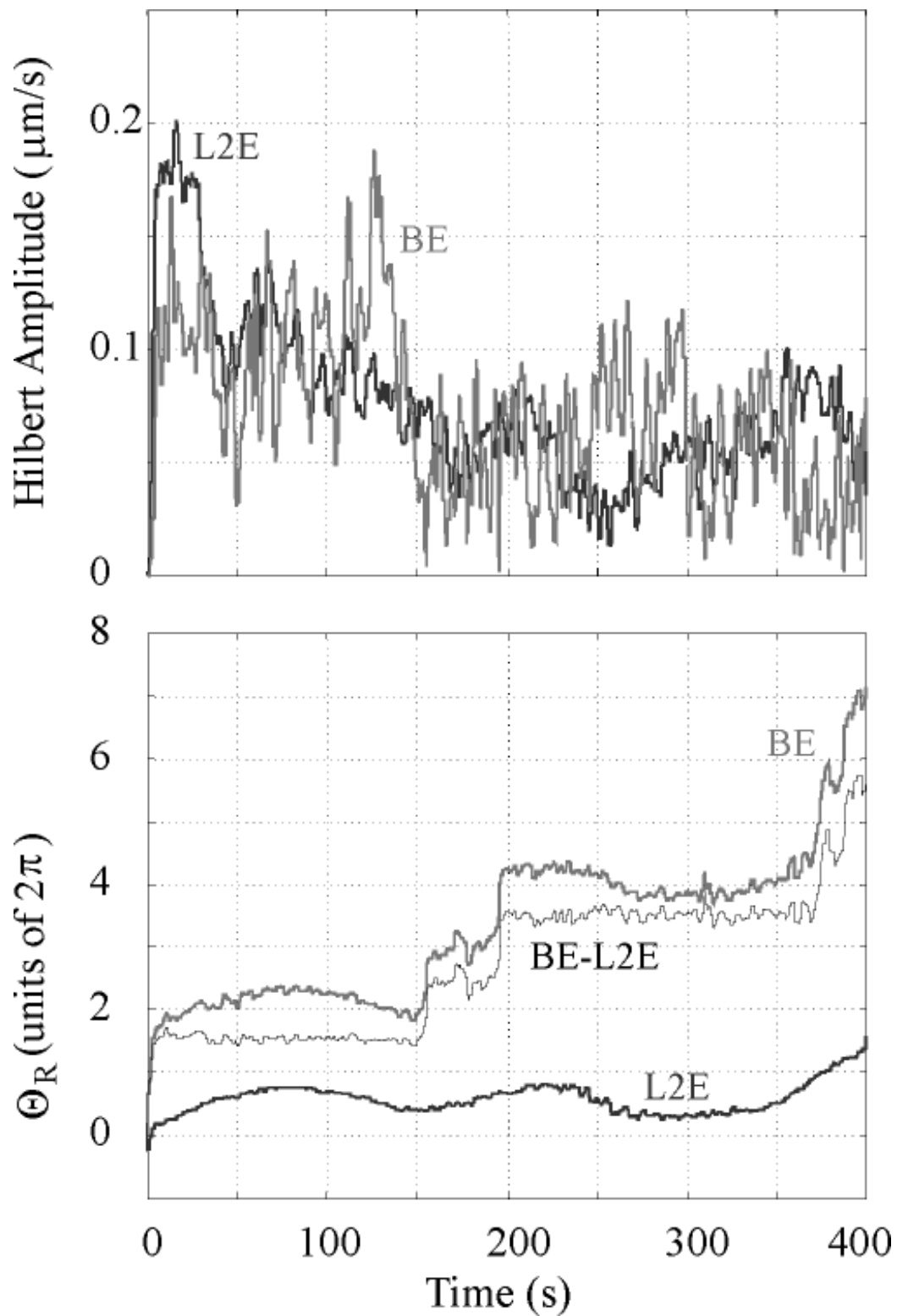


Figure 3.14 Comparison of the instantaneous amplitude (top) and Θ_R (bottom) of the E components of stations LA2 and B12. The data interval begins at 02:38:20 UTC on 18 April 1994.

Analysis of the reduced instantaneous phase calculated using the Hilbert transform is thus a very useful tool for investigating the variations of the frequency of narrowband tremor as a function of time. Because it can be applied to very short intervals, it gives an instantaneous reading of the frequency rather than an average over an interval, allowing observations of very slight and short term changes in the tremor frequency. It is much better suited to studying the frequency of individual narrowband signals than Fourier analysis.

To investigate Θ_R for the higher harmonics, I apply the method to the same interval of the recording at LA2 used for the fundamental. The test frequency for each harmonic, f_n , is $nf_0 = n0.63$ Hz. Although the amplitudes and polarization directions of the various harmonics are very different, the time variation of the frequencies are very similar (Figure 3.13). The intervals with constant slope used in Figure 3.11 can also be recognized in the reduced instantaneous phase of the harmonics. Their slope is exactly n times the slope for the fundamental during the same interval. This means that the harmonics are truly integer multiples of the fundamental.

For an investigation into the physical source of harmonic tremor the intervals between the regions of Θ_R with constant slope are especially interesting. If the frequency of harmonic tremor is a characteristic of the source, frequency changes reflect subtle changes in the physical state variables at or around the source. The changes do not occur suddenly, but gradually over an interval of several seconds or minutes. The frequency changes also take place at different rates.

Figure 3.14 shows the instantaneous amplitude and reduced instantaneous phase for the fundamental at the stations LA2 and B12. Although the instantaneous amplitudes of the E components (Figure 3.14, top) are very different, the similarity of the reduced instantaneous phases (Figure 3.14, bottom) is demonstrated by the fact that the difference, $\Theta_R(\text{BE}) - \Theta_R(\text{LA2E})$, is constant, except where there are jumps of 2π . These two stations are on opposite sides of the volcano, yet during the interval shown, their reduced instantaneous phases indicate that frequency changes are exactly the same at both stations. This is true not only for the stations LA2 and B12, but, aside from jumps of 2π caused by

low SNR, for all other combinations of stations and components, indicating that the frequency of the harmonic tremor and its changes characterize the source.

3.4 Polarization

In earthquake seismology, the polarization of the wave field is used in one of two ways. If the wave type is known, the orientation of the particle motion can be used to determine the direction to the source. On the other hand, if the location of the source is known, the polarization can help distinguish between different types of waves and in addition give some information of the characteristics of the medium such as anisotropy. With four three-component seismic stations and a single source it should be possible to use these insights to determine both the location of the source and the type of wave making up the harmonic tremor wavefield.

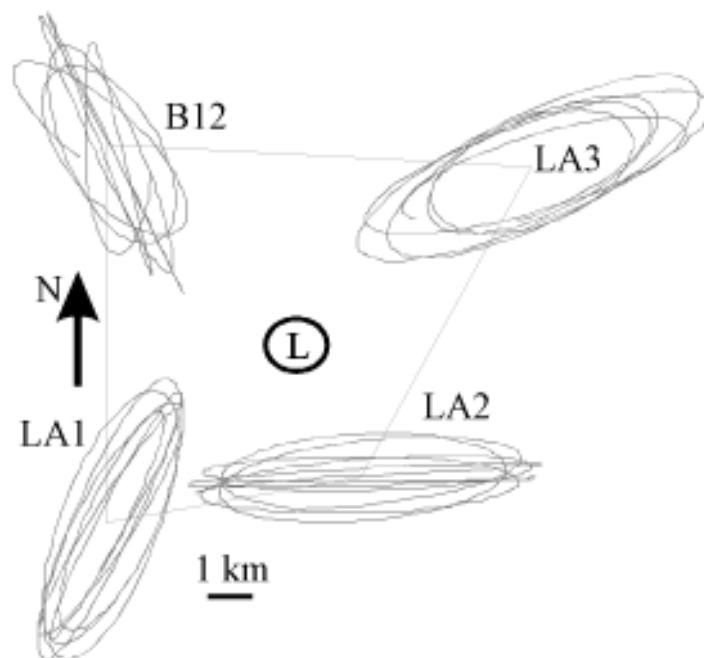


Figure 3.15 Particle motion in the horizontal plane for the fundamental frequency. The diagrams for the same 9.6 s at each station are plotted on a map of the stations of the Lascar network. To isolate the motion for the fundamental, all seismograms were bandpass filtered between 0.5 and 0.9 Hz. The "L" shows the approximate position of Lascar's active crater.

3.4.1 Particle Motion Diagrams

The particle motion of harmonic tremor plotted from the unfiltered ground velocity has no predominant direction of polarization. In contrast, particle motion diagrams become simpler, when the data are filtered using a narrow bandpass filter to select the energy of the individual spectral lines. Figure 3.15 shows the particle motion of the fundamental in the horizontal plane at each of the four stations during the same 9.6 s interval. During subsequent time segments, the particle motion at each station changes only slightly, remaining constant, or nearly so, for intervals much longer than the coherence time [SEIDL and HELLWEG, 1991]. The following discussion will therefore concentrate on the data interval

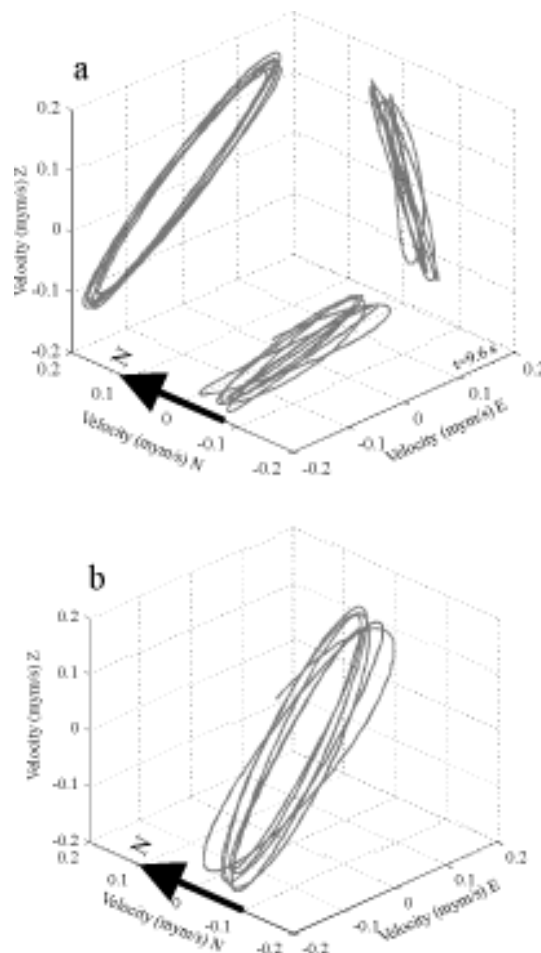


Figure 3.16 Particle motion due to the fundamental frequency at station LA2 for the 9.6 s interval used in Figure 3.15. The data are bandpass filtered between 0.5 and 0.9 Hz. (a) The particle motion is projected onto the Z-N, Z-E and N-E planes. (b) The three-dimensional particle motion is plotted in space.

shown in Figure 3.15 to show general features of the polarization. At station LA2 the horizontal particle motion is relatively stable and almost transverse to the direction to the crater. At B12 and LA3, on the otherhand, the particle motion is nearly radially polarized with respect to the active crater. The particle motion at LA1 is also steady, but neither transverse nor parallel to the crater direction. During the interval shown, the particle motion of the fundamental at the various stations is not consistent with a single wavetype propagating from a single source. Thus, the polarization of the fundamental in the horizontal plane cannot be used to determine the location of the source.

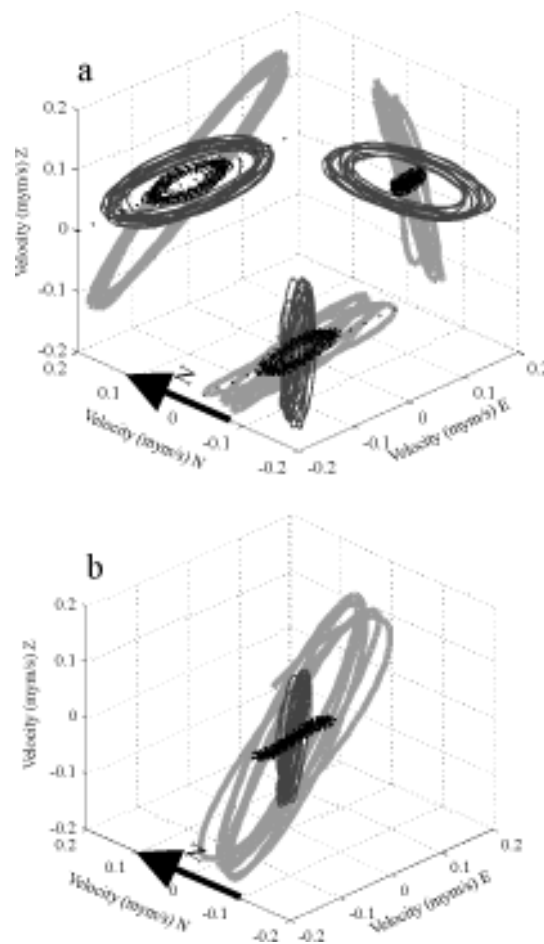


Figure 3.17 Particle motion for the first three harmonics ($n = 1, 2, 3$) at station LA2 for the same interval as Figure 3.15. The data are filtered as follows: fundamental [0.5-0.9] Hz ($n = 1$, light gray), first overtone [0.9-1.5] Hz ($n = 2$, medium gray), second overtone [1.5-2.1] Hz ($n = 3$, black). (a) Particle motion is projected onto the Z-N, Z-E and N-E planes. (b) The three-dimensional particle motion is plotted in space.

This conclusion is reinforced by observations of the particle motion in three-dimensions. To investigate the particle motion in space, I first project it onto the three planes defined by the orientation of the seismometer: the horizontal plane (N-E) and the two vertical planes (Z-N and Z-E). Figure 3.16a gives an example for station LA2. The three-dimensional particle motion diagram is presented in Figure 3.16b.

In Figure 3.17, data for the second and third harmonics (bandpass filters 0.9-1.5 Hz and 1.5-2.1 Hz) are superimposed on that of the fundamental. In the horizontal plane (Figure 3.17a), the fundamental (light gray) and third harmonic (black) appear to have similar orientations. In the three-dimensional representation, however, it is clear that all three spectral lines have completely different polarizations.

The three-dimensional particle motion diagrams for the other stations (Figure 3.18) are similar. At each station, the polarizations for the three harmonics are different. They cannot be interpreted as being produced by a single wave-type generated at a single point source. The same conclusion results from considering the polarization of an individual spectral line at the four stations: There is no simple interpretation in terms of a single source and single wavetype. The relative amplitudes of the lines are also very different at the various stations (Figure 3.18). At station LA2, for example, the fundamental (light gray) has the largest amplitude of the three lines. In contrast, the third harmonic (black) is largest at station LA3, while the second harmonic (medium gray) is largest at B12. This effect may stem from one of two causes: Either the amplitudes of the individual spectral lines are affected differently on their respective paths from source to station, or the radiation of the spectral lines from the source is not isotropic.

3.4.2 Directional Dependence of the Spectral Intensity

In the methods of polarization analysis just described, the polarization is examined separately for each peak in the spectrum. When analysing longer segments of tremor, it is desirable to calculate and display the average polarization for many peaks at the same time. This is possible, if we can calculate the directional dependence of the spectral intensity. To do this, the three component seismograms are rotated in predetermined increments of azimuth and inclination as described by PLEŠINGER et al [1986]. The power spectrum

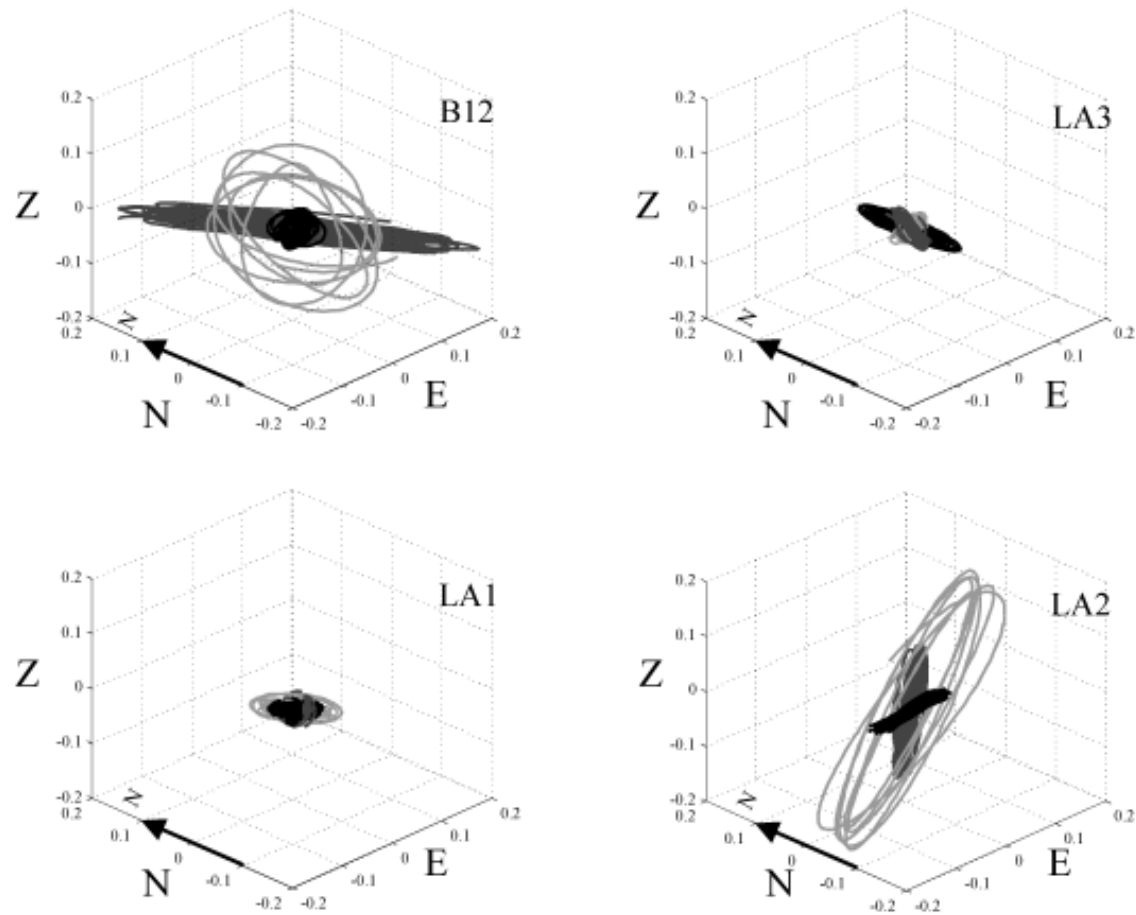


Figure 3.18 The three-dimensional particle motion at each station is plotted in space for the first three harmonics. Data are from the same interval as in Figure 3.15. Colors and filter parameters are as in Figure 3.17. Z, N and E axes give velocity in $\mu\text{m/s}$.

calculated for each rotated seismogram can then be plotted in different ways. Like all methods using the power spectrum, this method gives an average over the interval analysed. It can only be used to detect the direction of polarization with the highest average spectral intensity for a given frequency.

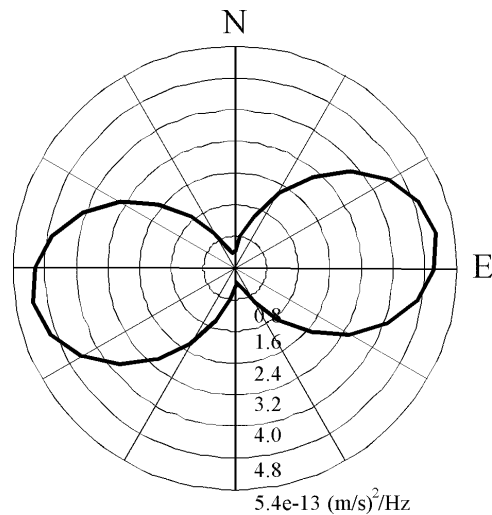


Figure 3.19 Directional dependence of the spectral amplitude of the power at 0.68 Hz in the horizontal plane at station LA2. The spectra are calculated as described for Figure 3.4 from the same 10 minute interval.

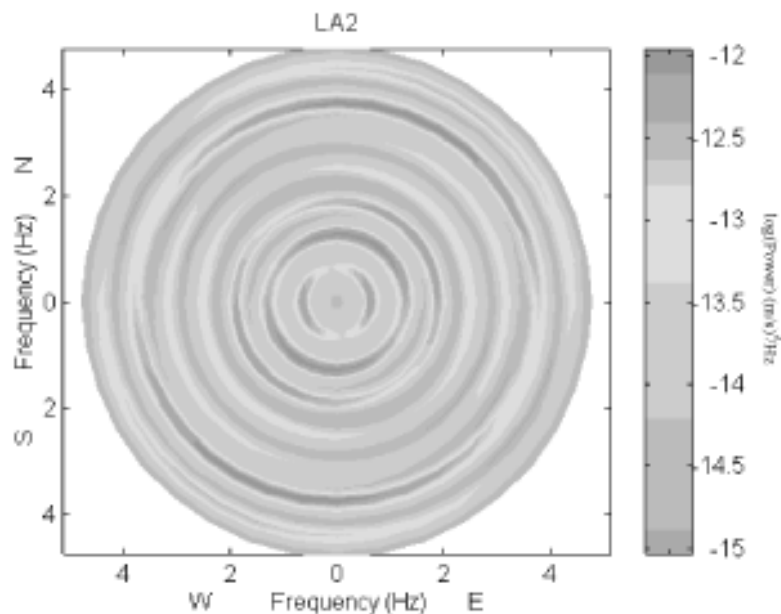


Figure 3.20 Directional dependence of the power spectrum in the horizontal plane at station LA2. The frequency is plotted radially and the spectral amplitude is represented by shading. The spectrum is calculated as described for Figure 3.4 from the same 10 minute interval.

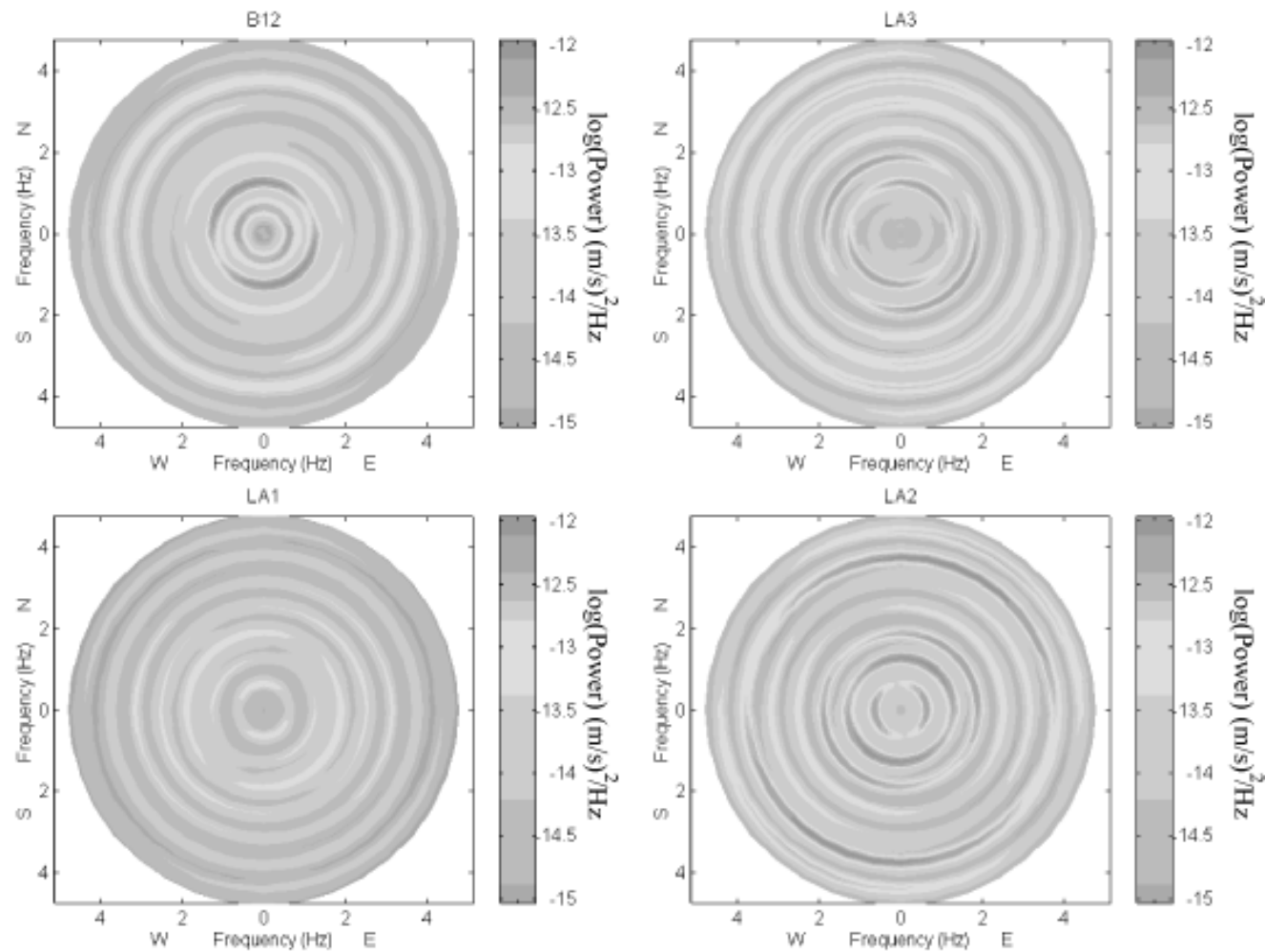


Figure 3.21 Directional dependence of the power spectra in the horizontal plane for the four stations of the Lascar network. The frequency is plotted radially and the spectral amplitude is represented by shading. The spectra are calculated as described for Figure 3.4 from the same 10 minute interval.

The power spectral amplitude for a selected frequency can be plotted in the horizontal plane with the angle representing the azimuth and the distance from the origin representing the spectral intensity. In the resulting diagram (Figure 3.19) the direction with the largest amplitude is the direction of the particle motion for which the spectral intensity is largest. This may mean that the amplitude for this direction is exceptionally large for a short period of time, or that the ground moves in this direction most of the time. The minimum amplitude is either a measure for the “background polarization noise” or it may indicate that other polarization directions have a relatively high rate of occurrence.

If the angle represents the azimuth and increasing frequency is plotted in the radial direction, the spectral intensity as a function of azimuth and frequency can be indicated by shading. Figure 3.20 shows the primary polarization directions for the first seven peaks at station LA2. This figure confirms the observation in Section 3.4.1 that the polarization is different for different peaks. In Figure 3.21, the directional dependence of the spectral intensity as a function of frequency is plotted for all four stations. None of the spectral peaks has a polarization field which permits a unique identification of its wavetype if the source of the seismic waves is in or near the crater.

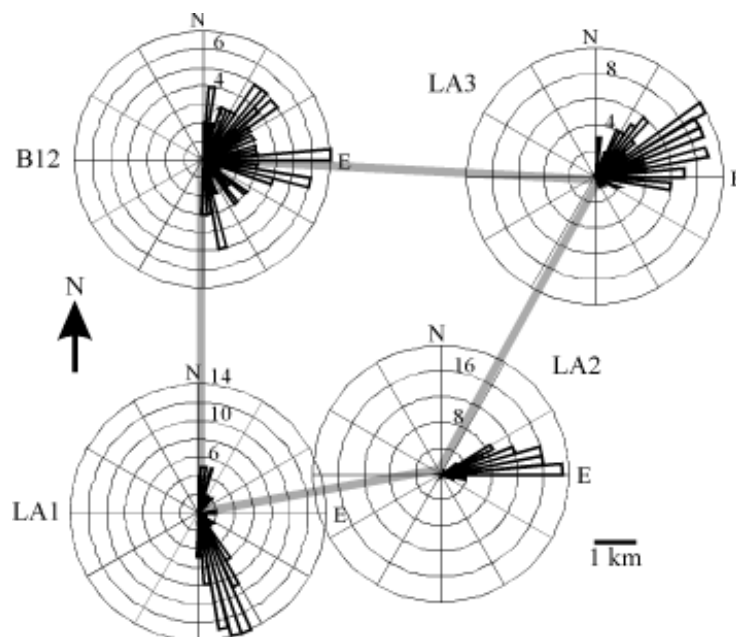


Figure 3.22 Horizontal polarization rosettes for all stations for the fundamental. The rosettes are plotted on a diagram of the Lascar network. The data are taken from the interval described in Figure 3.4, and were filtered using a bandpass filter [0.5-0.9] Hz.

3.4.3 Polarization Rosettes and Polarograms

With the methods described in Section 3.4.1 the polarization can only be studied for short intervals, while Section 3.4.2 shows the mean polarization, but only in two dimensions. An extension of the polarization rosette method [SEIDL and HELLWEG, 1992] to histograms offer an alternative means of studying the three dimensional polarization of longer intervals. If three component recordings are bandpass filtered to separate the energy of the individual spectral lines, the resulting seismograms are nearly sinusoidal. The three-dimensional particle motion diagrams for short intervals are ellipsoids (Figure 3.16). The major axis of a particle motion ellipsoid for a particular time interval, and thus its polarization direction, can be calculated using the covariance of the three filtered seismograms [MATSUMURA, 1981, KANASEWICH, 1981]. The polarization direction is defined as the direction of the eigenvector which corresponds to the largest eigenvalue of the covariance matrix.

SEIDL and HELLWEG [1992] show the results of such calculations as an azimuthally plotted histogram, or rosette, of the azimuths of the largest eigenvectors. The most common directions of polarization for the fundamental recorded at the four stations during a 10 minute interval, shown in Figure 3.22, agree with the particle motion for the short intervals shown in Figure 3.15.

The third component of motion is lost in this representation, however. Figure 3.22 gives no information about the inclination of the particle motion with respect to the horizontal plane. The representation of inclination originally chosen by SEIDL and HELLWEG [1992] — also a histogram in an arbitrarily selected vertical plane — can easily be misinterpreted. To avoid this, it is better to plot the azimuth and inclination explicitly in a polarogram. Figure 3.23 shows polarograms for the first six harmonics recorded at station LA2. The polarization of the fundamental at station LA2 (Figure 3.23, f1) has a sharp peak at 70° E azimuth and an inclination of 40° from the horizontal. For the second harmonic (Figure 3.23, f2), the method distinguishes two horizontal polarization directions, each with a unique inclination. Thus, the particle motion due to the second harmonic at the station LA2 has two directions of predominant polarization with different azimuths and inclinations. The higher order harmonics (Figure 3.23, lower four diagrams) also differ in their polarization. The polarization

differences among the harmonics observed during a short interval are also apparent in this analysis over a longer period.

The results from the polarization of a short data interval from the individual stations and the various harmonic frequencies presented in Section 3.4.1 are confirmed for longer intervals using

Table 3 -- Polarization Directions

Station	Azimuth from N	Inclination from H
B12	90°, 60°	0°, 15°
LA1	160°, 10°	10°, -5°
LA2	70°	40°
LA3	70°, 30°	5°, 5°

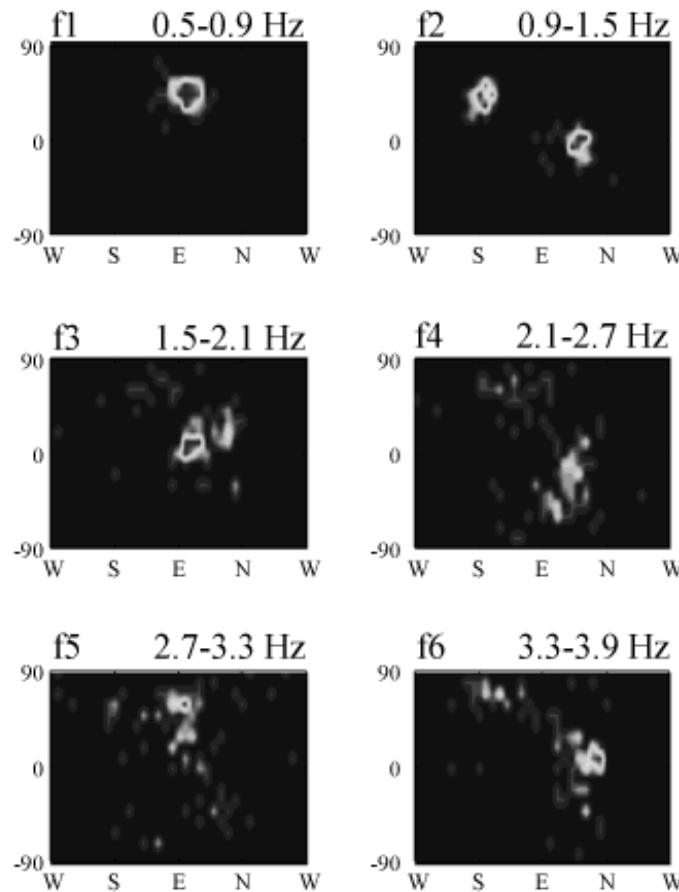


Figure 3.23 Polarograms for the first six harmonics at LA2 taken from the same interval as Figure 3.4. The horizontal axis gives the azimuth of the particle motion while the vertical axis gives its inclination from horizontal. The shading gives the number of times that a polarization ellipsoid occurs with the given orientation ($N > 6$ dark centers). The filter corner frequencies are given on the respective plots.

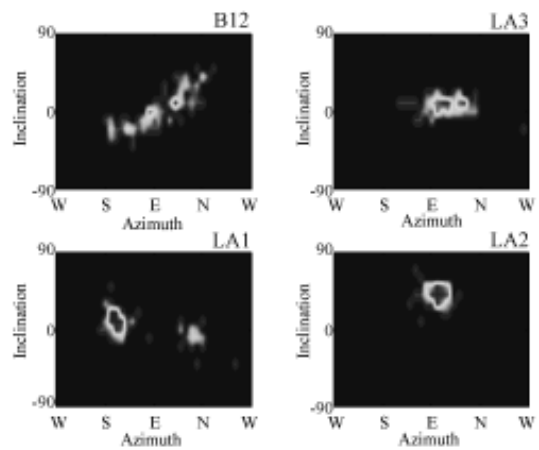


Figure 3.24 Polarograms of the four stations for the fundamental, f_1 : 0.5-0.9 Hz.

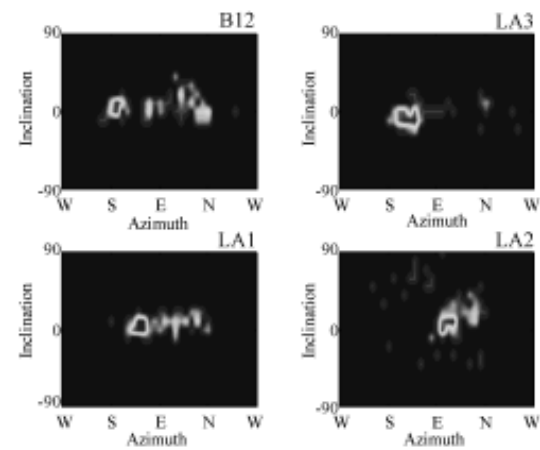


Figure 3.26 Polarograms of the four stations for the second overtone, f_3 : 1.5-2.1 Hz.

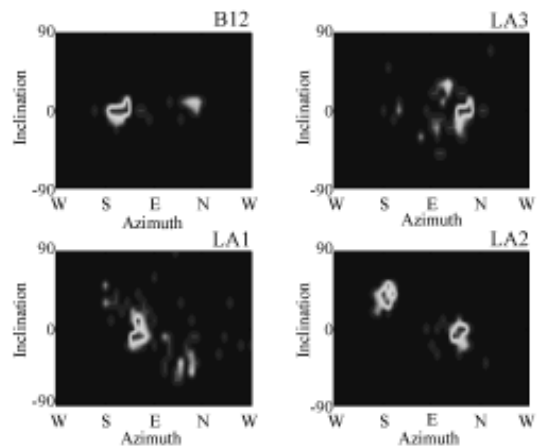


Figure 3.25 Polarograms of the four stations for the first overtone, f_2 : 0.9-1.5 Hz.

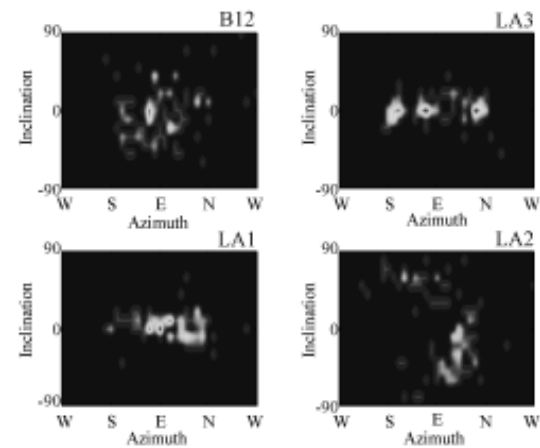


Figure 3.27 Polarograms of the four stations for the third overtone, f_4 : 2.1-2.7 Hz.

polarograms. Figures 3.24 through 3.27 show polarograms for the fundamental through the fourth harmonic at the four stations. The primary polarization directions for the fundamental are listed in Table 3 with the azimuth given in degrees from north (N) and the inclination in degrees from horizontal (H). None of the figures is consistent with a wavefield from a single source, for example the active crater, consisting of a single type of waves.

3.5 Summary of Observations and their Implications for Harmonic Tremor

The seismogram characteristic which is most consistent across components and stations is the fundamental frequency of the harmonic tremor. As demonstrated by both the phasor-walkout diagrams and plots of the reduced instantaneous phase, frequency changes occur at the same times and at the same rates at all stations. The frequencies of the integer harmonics also follow changes in the frequency of the fundamental exactly, $f_n(t) = nf_1(t)$ (where $n = 1,2,3\dots$). At times, more than 25 peaks can be observed in the spectrograms.

Peaks in a seismic spectrum are often attributed to path or site effects [SEIDL et al, 1981 and CHOUET, 1996]. However, since the frequencies are the same for all components at all stations, but the geologic conditions at the stations are different (Table 1), local conditions or path effects probably do not cause the many frequency peaks observed in Lascar's harmonic tremor. In addition, the influences of path and site cannot explain the changes in the fundamental frequency and the overtones that occur at the same time at all stations. The fundamental frequency must therefore be a characteristic of the source. The presence of energy at the frequencies of the harmonics at all stations indicates that these peaks are also generated at or near the source.

When the spectrum of volcanic tremor has more than one peak with at high signal-to-noise ratio, the seismic waves producing the peaks are usually attributed to different sources [CHOUET, 1996]. This is unlikely to be the case for the harmonic spectrum of Lascar's volcanic tremor, because there are so many overtones and their frequencies follow the frequency of the fundamental exactly. Harmonic spectra such as this are observed when the amplitude of the source is limited by non-linear effects.

In most seismological studies using three component data, the polarization of wavegroups at several stations can be used to determine whether the arriving signals are P-, S- or surface waves and the probable direction to the source. Despite several different attempts at polarization analysis, such considerations cannot successfully be applied to harmonic tremor. At a given station, the polarization direction is different for each of the harmonics. In addition, the polarization for a specific frequency, as measured at the four stations of the Lascar network cannot be reconciled with a single wavetype from a single point source. On the otherhand, the polarization at each of the stations remains relatively constant over long intervals. As demonstrated in the polarograms, each harmonic produces only one or at most two polarization directions at each station. Although the particle motion cannot be used to determine the direction to the source, its long term stability indicates that the source remains in the same place for an extended time

The apparently complicated polarization of Lascar's harmonic tremor may be due to unusual radiation patterns of a source that can be described neither an explosive point source nor as the double couple familiar from earthquake seismology. However, the polarization of the harmonic tremor wavefield is also affected during propagation in the complicated medium that is the volcanic edifice.

4 Tremor Frequency: The Source

Compared with the seismograms produced by the explosion and double-couple sources of earthquake seismology, volcanic tremor, especially harmonic tremor, is an unusual seismic signal. Earthquake sources, which are limited in time, are usually modeled as modified delta or step functions resulting from a dislocation in the earth. Seismic waves from the source then propagate through the earth. While the resulting seismogram may last for several hours depending on the epicentral distance, the frequency content of each segment is different and can be explained as a convolution of the source signal with the transfer function of the earth for the various types of waves. Harmonic tremor, on the other hand, continues for several hours at a time with only small changes in the frequency of the fundamental. It appears to be a sequence of repetitions of a slowly changing waveform. The changes in the shape of the waveform are reflected in the variation of the fundamental frequency, the amplitude, the frequency content and the polarization. An important objective of volcano seismology must be the effort to use information derived from tremor seismograms to describe the physical or chemical conditions at the tremor source through modelling.

Narrowband peaks observed in seismic recordings from volcanoes, particularly when they are members of a harmonic series, are generally attributed to oscillations of bodies of fluid or gas in the volcano. Several such models have been proposed, for instance, free eigenvibrations of a magma volume [SHIMA, 1958, SHIMOZURU, 1961], standing waves in a gas-filled conduit [SCHLINDWEIN et al, 1995, BENOIT and McNUTT, 1997] or the resonance of fluid-filled cracks [MORI et al, 1989 and CHOUET, 1996]. In these models, the authors assume that the conduit and its contents are an oscillator which they describe using a linear differential equation and which has been excited by the action of an impulsive force of unspecified origin. They claim that any harmonic overtones observed are the result of the excitation of higher modes. For these models, the authors match the frequency of the oscillations to the frequency of the tremor by varying the dimensions of the conduit model, along with the density, viscosity and other characteristics of the fluid in the conduit. In fact, these models neglect the most interesting question in volcano seismology: what is the the physical process which provides the force to excite the oscillator?

The observations derived from Lascar's unusual harmonic tremor with many overtones provide a foundation on which to develop physical models for the tremor source process which go beyond the oscillations in a gas-filled volume or a fluid-filled body in response to an outside force. To produce a spectrum with many exactly integer harmonics as in Lascar's harmonic tremor, the seismic waves generated by the source must have extremely steep slopes and a well-defined periodicity, as do sawtooth or square waves. Waves with such characteristics have been recorded during the resonance of bubbles in a sound field [LEIGHTON, 1994] and in shock waves during flow [LIGHTHILL, 1993]. They have also been observed in cyclic and reversible phenomena with rapid transitions between two or more quasi-steady states like Trevelyan's rocker [RAYLEIGH, 1945]. JULIAN [1994] models the source for tremor with harmonic overtones as the movement of conduit walls in response to unsteady flow of magma. Thus, the characteristics of harmonic tremor suggest that it is caused by the flow of liquids or gases and their interaction with the conduit.

Changes in the fundamental frequency of the harmonic tremor also provide clues to characteristics of the source. While they might be produced by a change in the speed of sound along the propagation path, such a change is not likely to occur over an interval of seconds. Doppler shifting of a constant frequency source due to motion toward or away from the stations can also be excluded as a cause of the frequency changes, since the stations lie in different directions from the volcano. In addition, if the frequency changes were caused by Doppler shifting, the frequency should revert to the original, constant frequency after motion ends. The frequency changes are probably the result of some systematic change at the source.

Models for the source of harmonic tremor must produce waveforms with the following characteristics.

- The signals must have a well-defined periodicity and steep slopes at some point during the cycle. The steep slope causes the many harmonic lines in the Fourier amplitude and power spectra.
- The model must also allow the cycle length to change over the time frame of minutes, as can be observed in Figure 2.12.

- The process must be “non-destructive”, since it continues for hours with no apparent external effect on the volcano.

Many of the flow processes studied in fluid dynamics satisfy these criteria. They are repetitive and may continue for hours, as long as the reservoir of fluid at the source is large. There are several fluids in any active volcano which may be involved in flow processes: Magma, water, either in the form of liquid or steam, and other gases such as CO₂ and SO₂. In general, a flow regime is described by the Reynolds number, which is dimensionless,

$$Re = vd/\kappa, \tag{4.1}$$

where v is the flow velocity of the fluid, d a measure of the characteristic dimension of the flow. κ , the kinematic viscosity of the fluid is defined as its shear or dynamic viscosity, η , divided by its density, ρ . The characteristic dimension of the flow regime depends on the specific example. In cases of flow in a conduit, d is taken to be the conduit diameter, while it may be the diameter of an obstruction in other cases.

Three flow regimes in which a continuous, steady flow is converted into a cyclic stream can be modelled as Vortex Shedding, Slug Flow and the Soda Bottle. The three models can be distinguished on the basis of the range of Reynolds numbers in which they occur. Vortex shedding occurs when the Reynolds numbers lies between 100 and 10⁵ [FABER, 1995]. Slug flow begins in model flow systems if the Reynolds number rises above 2300 [FABER, 1995], while the Reynolds numbers for the Soda bottle model must be very low, on the order of 1 [GINZBURG, 1963]. For each of the three models, I describe the phenomenon and draw parallels between the experimental conditions under which it is observed and realistic situations in a volcano which might produce it. Finally, I will constrain the model of the flow system using parameters measured from the harmonic tremor seismograms and discuss its implications for the source of tremor.

4.1 Vortex Shedding

Vortices or eddies often develop in the flow field, or wake, behind bluff objects. Two everyday phenomena caused by vortex shedding are the fluttering of a flag and the “singing“

of power lines in the wind. Fluid dynamics studies mainly concern themselves with the behavior of vortices behind cylinders, however vortex shedding has also been observed during flow past corners [BIRKHOFF and ZARANTONELLO, 1957] or steps [HOGAN and MORKOVIN, 1974] and in many other configurations which are important in engineering problems.

As the flow velocity increases, eddies which develop behind an object are likely to detach from it, forming a von Kármán vortex street. As each vortex develops and detaches, it produces sound waves. As long as the Reynolds number remains constant, eddies are shed regularly with alternating spin or vorticity. The sound pulses then appear as periodic oscillations of a sound field with a characteristic frequency [MORSE and INGARD, 1968].

When the Reynolds number is low ($Re < 10$), viscous forces are very important in a flow system. A fluid will flow smoothly and evenly around an object. As the velocity of the fluid, and consequently Re , increase, the flow separates from the object and eddies begin to develop on its downstream side. In calculating the Reynolds number, the characteristic dimension, d , is the diameter of the object. At still higher velocities ($Re > 100$), the eddies

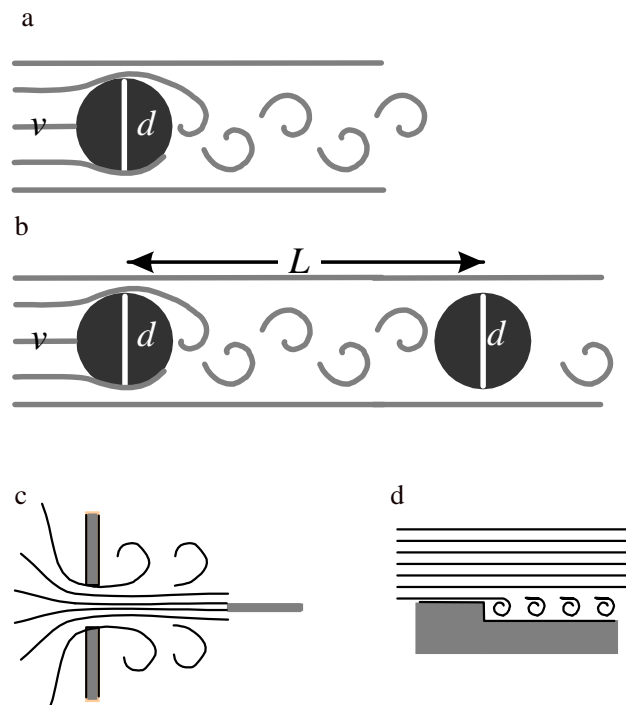


Figure 4.1 Model systems for eddy shedding. (a) Simple eddy shedding behind an obstacle. (b) Eddy shedding with resonance. (c) Jet edge whistle. (d) Eddies behind a step.

are shed regularly and a von Kármán vortex street develops (Figure 4.1). The shedding frequency, f_K , is given by the Strouhal number,

$$St = f_K d/v . \quad (4.2)$$

In this case, the Reynolds and Strouhal numbers are calculated using the size of the obstacle for d . For all practical purposes, St can be taken to be 0.2 when the Reynolds number lies between 10^2 and 10^5 [MORSE and INGARD, 1968, FABER, 1995, TRITTON, 1988]. When $Re > 1000$, the wake becomes increasingly turbulent and the periodicity is less strong [BIRKHOFF and ZARANTONELLO, 1957].

Under certain conditions vortex shedding may be coupled into a feedback mechanism, producing very large forces and sound amplitudes. As many as 10 integer harmonics have been observed [MORSE and INGARD, 1968]. The geometric conditions necessary for stimulated sound emission due to a feedback resonance from eddy shedding exist when the shedding frequency, f_K , is equal to one of the transverse resonance frequencies of the duct, f_i . If there is a cylinder of diameter d in a duct with the transverse dimension D , for example,

$$f_K = 0.2v/d = nc/2D = f_i, \quad i = 1, 2, 3, \dots \quad (4.3)$$

where c is the speed of sound in the fluid.

Resonance may also occur when the vortex street produced by one cylinder interacts with a cylinder downstream (Figure 4.1b). The interaction between the eddies and the second cylinder produces a pressure disturbance which is radiated in all directions and propagates through the fluid with the velocity of sound. When the pressure pulse reaches the upstream cylinder, it affects the formation and detachment of the eddies. If the pressure disturbance arrives at the time in the formation cycle of a new vortex to stimulate its growth, the vortex will be amplified, and strong acoustic emission will result. To calculate the conditions necessary for stimulation, it is necessary to know how long it takes a vortex to travel between the two cylinders. If the cylinders are separated by a distance, L , a vortex reaches the second cylinder after an interval, $T_D = L/v_D$, where the eddy drift velocity, $v_D \sim 0.8v$ [MORSE and INGARD, 1968]. The pressure pulse then travels at velocity c back to the first

cylinder, and arrives there after an interval, $T_c = L/c$. Usually, $v_D \ll c$, so $T_D \gg T_c$ and the travel time of the pressure pulse can be ignored. The condition for resonance is then that the inverse of the travel time be a multiple of the von Kármán vortex frequency:

$$1/T_D = nf_K \quad (4.4a)$$

or

$$v_D/L \sim 0.8v/L = 0.2nv/d, \text{ or } L \sim 4d/n. \quad (4.4b)$$

Resonances with this type of geometry have produced damage in cooling towers of power plants [TRITTON, 1988].

Eddies form behind almost any object, not only cylinders, under the right flow conditions. HOGAN and MORKOVIN [1974] observed vortex formation at 9.5 Hz behind a 0.0013 m step with flow velocities in air of 3.3 m/s (Figure 4.1d). Vortex resonance can also be observed in jets (Figure 4.1c, [BIRKHOFF and ZARANTONELLO, 1957, MORSE and INGARD, 1968]). There are many reports of vibration-induced damage in dams [i.e. DOUMA, 1974, LYSENKO and CHEPAJKIN, 1974, GONCHAROV and SEMENKOV, 1974]. In particular, LJATKHER [1980] describes “self-induced vibrations” in a dam spillway that he attributes to vortex shedding. The amplitude of these vibrations in an instrumented structure more than 2.5 km from the dam was greater than 0.5 mm/s.

In a volcano, it is unrealistic to expect to find cylinders in the center of a flow field. Steps, corners and jets similar to those sketched in Figure 4.1 are however not unlikely. Jets, for example, have been observed in association with steam explosions and harmonic events at Semeru [HELLWEG et al, 1994, SCHLINDWEIN et al, 1995]. In geological investigations of dike structures, junctions and constrictions have been observed which could act like corners or steps in a flow field.

Just as the fundamental frequency is a basic characteristic of harmonic tremor, von Kármán vortex streets, which occur when $10^2 < Re < 10^5$, are defined by their shedding frequency, f_K , (Equation 4.2). Solving Equations 4.1 and 4.2 for the flow velocity v in terms of frequency, the Reynolds number and the kinematic viscosity gives:

$$v^2 = f_k \kappa Re / St. \tag{4.5}$$

Figure 4.2 shows the velocity (color) for a range of Reynolds numbers and kinematic viscosities, if the vortex shedding frequency is taken to be $f_1 = 0.63$ Hz, the fundamental frequency of the harmonic tremor. The Reynolds number range for which vortex resonance occurs is indicated by cross-hatching. The colored bars show typical kinematic viscosities for dry air, water and steam at atmospheric pressure and various temperatures, for steam at 2×10^7 Pa and for andesite melt at several temperatures [MURASE and McBIRNEY, 1973]. A lithostatic pressure $P = 2 \times 10^7$ Pa corresponds to a depth below the surface, h , of

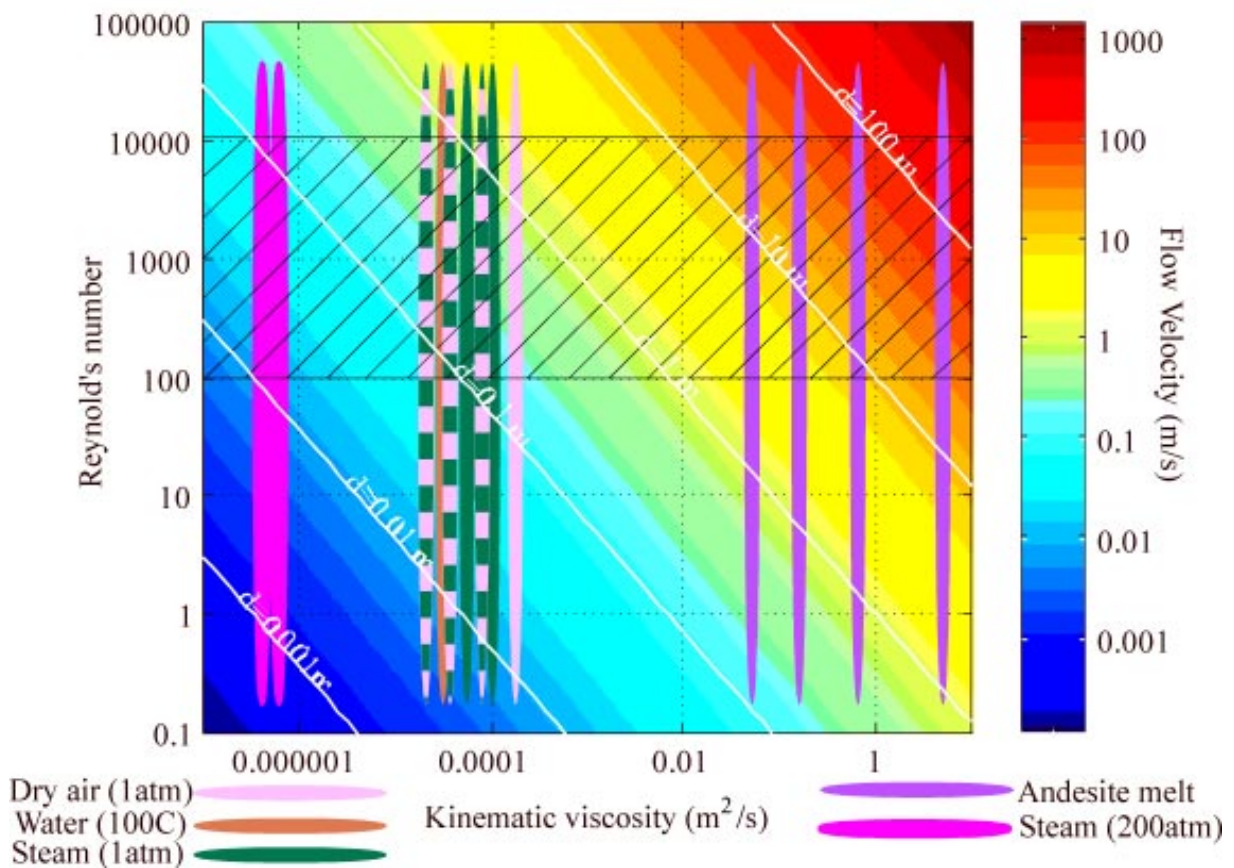


Figure 4.2 Flow velocities for the eddy shedding model as a function of Reynolds number and kinematic viscosity when the eddy frequency is 0.63 Hz. The flow velocity, denoted by color, is calculated from Equation 4.5. The colored bars give the kinematic viscosities of several fluids which may be encountered in a volcano. Eddy shedding may occur when the Reynolds number lies within the cross-hatched region. The white lines show the flow dimension as a function of kinematic viscosity and Reynolds number, given the eddy frequency.

$$h = \frac{P}{\rho g} = 2 \times 10^7 \text{ Pa} / (2.5 \times 10^3 \text{ kg/m}^3 \cdot 9.81 \text{ m/s}^2) \sim 800 \text{ m}$$

where ρ is the density of the rock and g the gravitational acceleration at the surface of the earth. Characteristic dimensions calculated using Equation 4.3, are plotted as labeled, white contour lines.

If vortex shedding resonance is the process which generates harmonic tremor, then Figure 4.2 provides several clues to the fluid involved, as well as the location and size of the obstacle causing the eddies. For steam at pressures equivalent to a depth of 800 m to shed eddies every 1.6 s, the obstacle could range in size from 4 mm to 4 cm at flow velocities of 1 cm/s to 10 cm/s. At the opposite end of the range of kinematic viscosity, even the most fluid andesite melt, assuming it retains the characteristics that MURASE and MCBIRNEY [1973] reported, must flow at 5 m/s to 50 m/s through characteristic flow dimensions of 5 m to 50 m in order to generate vortices that detach every 1.6 s. The order of magnitude for velocity and obstacle size for water at 100° C, superheated steam or dry air at atmospheric pressure are 0.1 - 5 m/s and 0.05 - 0.5 m, respectively. These dimensions are similar to those of dikes observed in volcanoes.

Shed vortices produce sound waves in two ways. First, the eddies produce density variations in the fluid, in particular when they come into contact with conduit walls, and are

Table 4 -- Eddy Shedding Forces

Fluid	Density (kg/m ³)	Velocity (m/s)	Dimension (m)	Force assuming length of 1 m (N)
Steam (2x10 ⁷ Pa)	660	0.05	0.01	0.008
Steam (100° C)	0.6	1	0.5	0.15
Steam (400° C)	0.3	1	0.5	0.08
Water (100° C)	960	1	0.5	240
Andesite (1400° C)	2500	5	5	1.5x10 ⁵

therefore sources of sound waves. Secondly, each time an eddy is shed from the object, it produces a force on the object. The force per unit length due to shedding on a cylinder of diameter d , is given by MORSE and INGARD [1968]:

$$F_l \sim b\rho v^2 d/2, \tag{4.6}$$

where where b is a unitless constant and its range, $0.5 \leq b \leq 2$, has been determined experimentally [MORSE and INGARD, 1968]. This force is similar to the force due to the Magnus effect. It is actually a time-varying force on the cylinder that increases as the vortex forms and reaches a maximum when the eddy is shed, then dropping suddenly. In the volcano, each impulse to the obstacle as an eddy is shed will propagate in the medium as a seismic wave. For the flow velocities and dimensions given in the previous paragraph, Table 4 gives

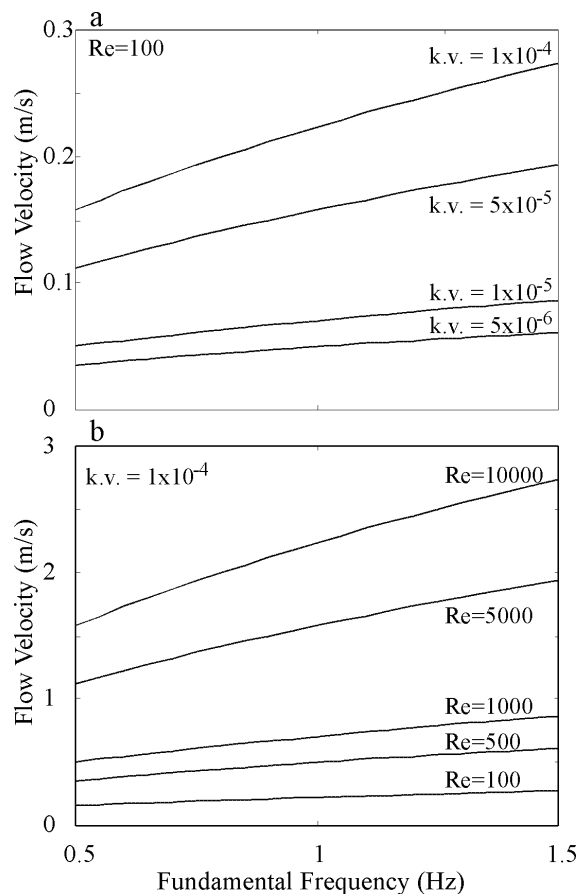


Figure 4.3 Relationship of flow velocity to frequency. (a) The Reynolds number is held constant and flow velocities are given for various kinematic viscosities taken from the range for air, steam and water at low pressures. (b) Kinematic viscosity is held constant and flow velocities are given as a function of shedding frequency for several Reynolds numbers. $k.v.$ is the kinematic viscosity in m²/s.

the force due to eddy shedding calculated using Equation 4.6 on a cylinder of 1 m length. These values can only be taken only as a rough estimate of the minimum order of magnitude for the force as they do not take resonance into account. This can intensify the force by several orders of magnitude. In addition, it is highly unlikely that the obstacle producing the eddies is a cylinder. While many papers describe observations and experimental evidence of damage due to eddy shedding, there are few measurements of the forces involved and little theory that can be applied to calculating exact forces. BLAKE [1986] reports that under appropriate geometric conditions, the forces due to eddy shedding can exceed the values predicted by Equation 4.6 by four orders of magnitude.

Section 3.1.2 gives the amplitude for a point force as the source of Lascar's harmonic tremor as being on the order of 10^6 N. Even if feedback resonance is a factor [BLAKE, 1986], and the geometry of the vortex-producing obstacle can be approximated as a cylinder, so that Equation 4.6 is valid, it is unlikely that the first three substances listed in Table 4 would cause sufficiently large forces to be involved in the generation of harmonic tremor. According to the table, the forces due to the flow of andesite would be nearly large enough to produce the tremor observed at Lascar. It is, however, unlikely that andesite would flow at a velocity of 5 m/s or more, if the volcano is not erupting. There were no reports of eruptions during the observation of harmonic tremor. Only the vortex shedding in the flow of water near the surface, with the additional assumption of feedback resonance [BLAKE, 1986] produces forces which approximate the estimate of the amplitude of a point force derived from the seismograms using Equation 3.1.

If Lascar's harmonic tremor is caused by eddy shedding in a flow of hot water near the volcano's surface, changes in the frequency may result from changes in the flow velocity, the viscosity of the fluid or the geometry of the obstacle. If the geometry of the obstacle were to change rapidly, it would probably mean some movements of the rock walls of the conduit. Such changes are unlikely to be reversible and the tremor would probably stop. Reversible changes in the flow velocity, due to changes in the pressure or the kinematic viscosity are quite realistic. Figure 4.3a shows how the fundamental frequency changes with changing flow velocity at constant Reynolds number for several different kinematic

viscosities. In Figure 4.3b the relationship between flow velocity and frequency at various Reynolds numbers is shown for constant kinematic viscosity. Relatively large changes in the kinematic viscosity or the Reynolds number produce only small changes in the flow velocity and tremor frequencies.

4.2 Turbulent Slug Flow

Intermittent turbulence or turbulent slugs are sometimes observed in the transition from purely laminar pipe flow to completely turbulent flow [GINZBURG, 1963, TRITTON, 1988]. In this case, the slug is a region of turbulence in the pipe, which is separated from other turbulent segments by regions of laminar flow. Figure 4.4 shows a sketch of a slug flow cycle. If the reservoir is large, the pressure difference between the reservoir and the outlet will remain approximately constant over a long period of time. When calculating the Reynolds number for this experiment, the characteristic dimension is the diameter of the pipe or

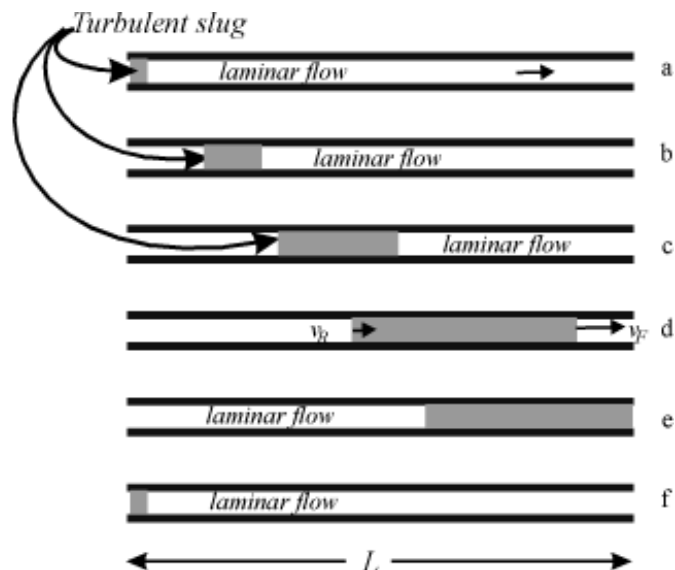


Figure 4.4 Cycle of turbulence slug generation. (a) Laminar flow in the conduit has reached a Reynolds number at which turbulence is generated at the intake. (b) The turbulence slows the flow and therefore lowers the Reynolds number, so that the fluid behind the turbulent section or slug again flows laminarily. (c-d) As the turbulent slug progresses through the conduit, it lengthens because its forward end progresses more rapidly than the average flow velocity while the rear end is slower. (e-f) Eventually the slug leaves the end of the conduit and the flow velocity increases again until a new slug is generated.

conduit, d . One of the necessary conditions for the generation of turbulent slugs is that the ratio of the length of the pipe or conduit, L , to its diameter, d , be $L/d > 50$. For a given pressure, the flow rate will be higher if the flow is laminar and lower if the flow is turbulent.

Imagine a situation, as in Figure 4.4, where the flow at a certain Reynolds number in a pipe connecting two reservoirs is laminar. Experiments have shown that sometimes when the Reynolds number increases, usually due to an increase in the flow velocity, turbulence develops at the intake (Figure 4.4a, [GINZBURG, 1963, TRITTON, 1988, FABER, 1995]). The turbulent slug moves through the pipe at a lower velocity than the laminarily flowing fluid (Figure 4.4b). At the same time, its front and rear edges propagate at different velocities through the pipe, the front at a higher velocity, v_F , than the “center” of the slug and the rear at a lower velocity, v_R , so that the slug grows in length as it progresses (Figure 4.4c). In the meantime, the fluid behind the slug can no longer flow at the high velocity which caused turbulence to develop; the flow becomes laminar again (Figure 4.4b). When the front end of the slug has left the pipe, the region of laminar flow grows until the rear of the turbulent slug has left the pipe (Figure 4.4e). Finally the velocity of the flow can again increase to the point at which a new turbulent slug is generated at the intake (Figure 4.4f). The cycle begins again.

The propagation velocities of the front and rear ends of the slug have been studied experimentally [TRITTON, 1988]. Figure 4.5 [taken from TRITTON, 1988] shows the ratios of v_F

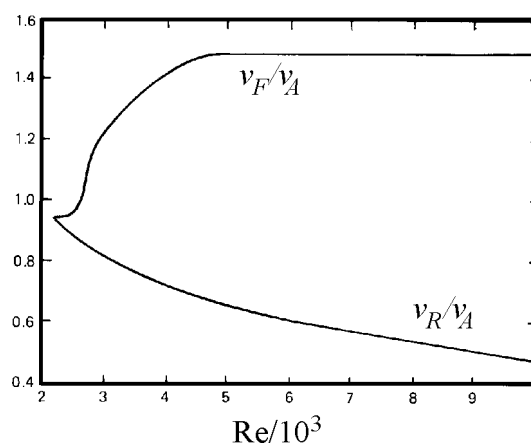


Figure 4.5 Ratios of front and rear velocities of turbulent slugs to the mean flow speed as functions of the Reynolds number, based on experimental results. Taken from TRITTON [1988], p. 286.

and v_R to the mean flow velocity, v_A , as a function of the Reynolds number of the flow. When $Re \sim 2300$ and generation of turbulent slugs begins, these two velocities are very close to v_A , and the slugs do not grow while flowing through the system.

Slug flow is a cyclic process. The period of the cycle is determined by the length of the conduit and the velocity of the rear of the slug,

$$T_S = L/v_R. \quad (4.7)$$

The flow leaving the conduit is turbulent from the time the front of the slug reaches the end, L/v_F , until the rear of the slug reaches the end, L/v_R . $T_T = L/v_R - L/v_F$ is the time the flow is turbulent. This value is used along with the cycle length to calculate the intermittency factor, the fraction of time that the motion is turbulent [TRITTON, 1988],

$$T_I = T_T/T_S = (L/v_R - L/v_F)v_R/L = 1 - v_R/v_F. \quad (4.8)$$

If, for a given configuration, the mean flow velocities in turbulent and laminar regimes are taken to be constants, and the change between the regimes virtually instantaneous, the variation of flow velocity can be modeled as a square wave (Figure 4.6a). This figure also shows the relationship between the intermittency and the period of the slug flow cycle. Figure 4.6b [TRITTON, 1988] shows an example of measured flow velocities taken from the

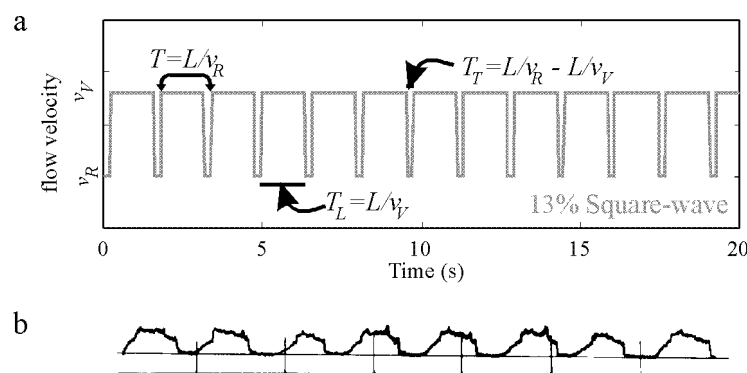


Figure 4.6 Flow velocity as a function of time in a fluid flowing in a turbulent slug regime. (a) Theoretical approximation using a 13% square wave describing the intermittency ($Re=2675$, taken from Table 5). (b) Trace of fluid velocity from a flow experiment showing local mean velocity changes between laminar and turbulent slug regimes ($Re=5000$, $L/d=290$). Taken from TRITTON [1988], p. 18.

literature. Although this waveform is not exactly a square-wave, this example does have extremely rapid velocity changes which produce harmonics in a Fourier spectrum.

For slug flow to occur in a volcano, two reservoirs of fluid must exist at different pressures, separated by a long, narrow conduit with $L/d > 50$ (Figure 4.7). Such conduits may be preserved as dikes often observed in eroded volcanoes. If the slug flow occurs in a conduit connecting an internal reservoir to the atmosphere and the volcano is not erupting, the fluid cannot be magma, but must be water or gases such as steam.

The parameters which define this model are the kinematic viscosity of the fluid, the pressure difference between the reservoirs and the dimensions (length and diameter) of the connecting conduit. To test the model, these parameters must be related to parameters which can be measured from the seismograms of harmonic tremor, such as the harmonic frequencies, f_n , $n = 1, 2, 3, \dots$ (Figure 3.3), and the shape of the spectrum (Figure 3.5). Figure 4.8 shows the power spectrum of a 10 minute interval of harmonic tremor determined from the recording of the east component at station LA2. It is compared with the power spectrum of a 13% square-wave. These spectra are similar, in that their spectral lines appear in groups of 7, with decreasing amplitude. This suggests that the seismogram may be produced by a source function like a square wave with an intermittency of 13%. Figure 4.5 can be used to determine the intermittency for different Reynolds numbers (Table 5). For an intermittency of 13%, the Reynolds number of the flow is 2675.

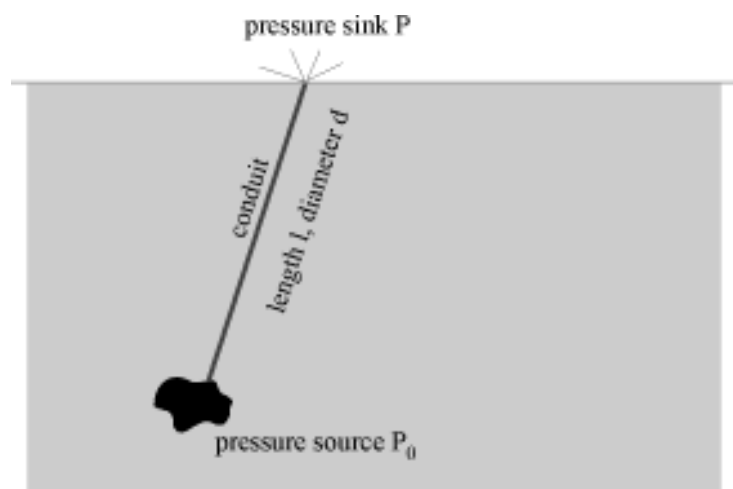


Figure 4.7 Geometry for generating turbulent slug flow in a volcano.

Table 5 -- Slug Velocities and Intermittancy

Re	v_R	v_F	Intermittency
2300			0
2500	0.88	0.96	0.08
2675	0.87	1	0.13
2750	0.85	1.05	0.19
3000	0.8	1.22	0.34
4000	0.73	1.45	0.5
5000	0.65	1.48	0.56
6000	0.6	1.48	0.59
7000	0.55	1.48	0.63

According to this table and Figure 4.5, variations in the flow parameters should have two effects. The intermittency should change with the Reynolds number. In addition, the frequency of the cycle should change as the ratio of v_R/v_F changes.

For a given Reynolds number, the flow velocity is related to the conduit size and the kinematic viscosity of the fluid by Equation 4.1. In Figure 4.9, the flow velocity has been calculated using Eq. 4.1 for $Re = 2675$. The colors denote the flow velocity as in Figure 4.2.

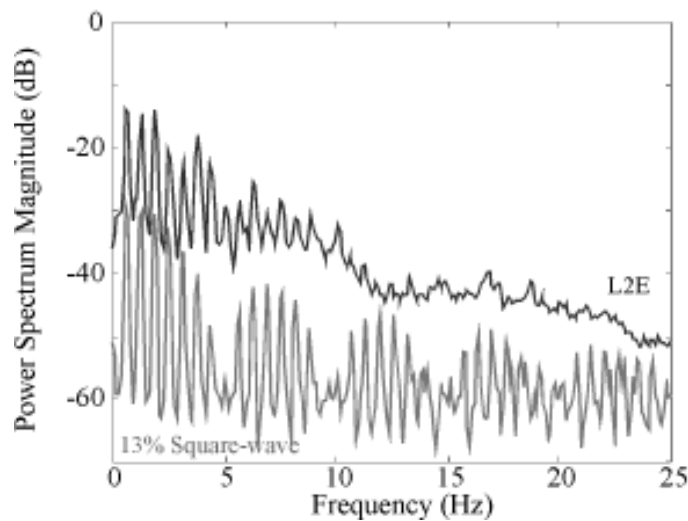


Figure 4.8 Comparison between the power spectra of harmonic tremor (black, taken from Figure 3.3b) and a 13% square wave (gray).

The cross-hatched area indicates the range of conduit sizes which may be expected in a volcano, while kinematic viscosities of andesite melt, water (100° C), steam at various temperatures and pressures, as well as dry air at several temperatures are marked for reference by colored bars.

Equation 4.8 gives another constraint on the geometry. If $L/d = 50$, as is necessary for slug flow and the period of the cycle is that of Lascar's harmonic tremor, $T_s = 1/f_1 = 1.6$ s, then $v_R = L/T_s = 50d/T_s = 50f_1d$. This is plotted in Figure 4.9 as a white bar marked with the frequency. It gives the correspondence between conduit size and flow velocity for cycles of $T_s = 1.6$ s. If the kinematic viscosity of the fluid is of the order of 10^{-6} m²/s, as it would be for steam under high pressure, the conduit would be only several centimeters in diameter, and the flow velocity would be about 0.01 m/s. When the kinematic viscosity is about 10^{-3} m²/s, in the range for air, water and steam at atmospheric pressure, which corresponds to near-surface hydrothermal activity, then the conduit diameter is on the order of 0.1 m and the flow velocity around 1 m/s. According to this model, the flow velocity for even the least viscous andesite melt is close to 100 m/s. Such movement is highly unlikely in a volcano that is not erupting. Thus, the slug flow model indicates that the source of the harmonic tremor recorded at Lascar Volcano must be near the surface, and the fluid generating the signals is not likely to be magma, but rather steam, water or air.

In a slug flow regime, the pressure at any given time and point along the conduit depends on whether the flow is mainly laminar or turbulent at that point. During laminar flow the pressure gradient is given by the Hagen-Poiseuille law [SCHLICHTING, 1958, FABER, 1995]:

$$Re = \left(\frac{d}{2}\right)^3 \frac{\rho}{4\eta^2} \frac{dP}{dL}. \quad (4.9)$$

Suppose one end of the conduit is at atmospheric pressure. If the dimensions for the conduit are taken from Figure 4.9 for flowing water as $d = 0.2$ m and the length is then calculated, $L = 50d = 10$ m, and the Reynolds number is 2675, then Equation 4.9 gives the pressure gradient as $dP/dL \sim 9$ N/m³.

In the region of turbulence the pressure gradient will be steeper than where the flow is laminar, because the net movement of fluid through the conduit is lower than during laminar flow [GINZBURG, 1963, TRITTON, 1988, FABER, 1995]. When the flow is fully turbulent, the Reynolds number and the pressure gradient are related by an experimental relationship given by Blasius [SCHLICHTING, 1958, FABER, 1995]

$$Re^{7/8} = \frac{22.4}{\pi} \left(\frac{\rho(d/2)^3}{\eta^2} \frac{dP}{dL} \right)^{1/2} \quad (4.10)$$

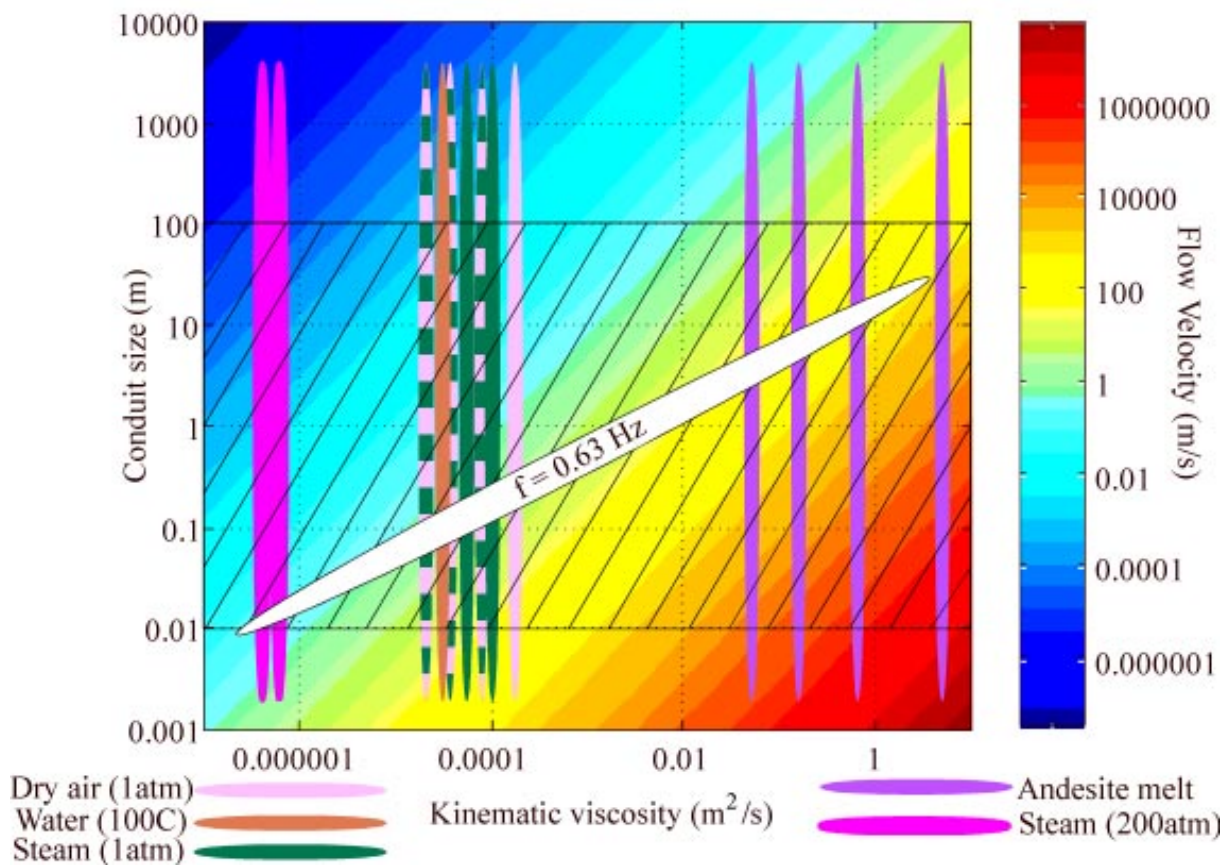


Figure 4.9 Flow velocities for the slug flow model as a function of conduit size and kinematic viscosity when the Reynolds number of the flow is 2675. The flow velocity, denoted by color, is calculated using Equation 4.1. The colored bars give the kinematic viscosities of several fluids which may be encountered in a volcano. Conduit diameters may be reasonably expected to lie within the cross-hatched region. The sloped white region shows configurations for which the slug flow cycle would have a period of $T_s = 1/f_1 = 1.6 \text{ s}$.

For the same geometry and Reynolds number as above, the pressure gradient is $dP/dL \sim 16 \text{ N/m}^3$ for turbulent flow.

In this model, the harmonic tremor signal measured at the stations of the Lascar network is caused by changes in the fluid's pressure which occur when the flow changes from laminar to turbulent. In principle, these pressure variations act as a variable force on the conduit walls [WALLIS, 1969, CHOUET et al, 1997]. Unfortunately, it is difficult to describe these variations theoretically. Although the description here gives the Reynolds number as a constant, it in fact changes during a cycle as the flow changes from laminar to turbulent and back (Figure 4.10). Practically it is difficult to estimate the relative volumes and flow velocities of laminar and turbulent fluid as a function of the cycle. In addition, as shown in Figure 4.10, experiments have demonstrated that Equations 4.9 and 4.10 do not completely describe situations in which intermittent turbulence and slug flow develop, because the flow is not completely turbulent [SCHLICHTING, 1958]. It is thus difficult to correctly estimate the amplitude of the forces on the medium during slug flow.

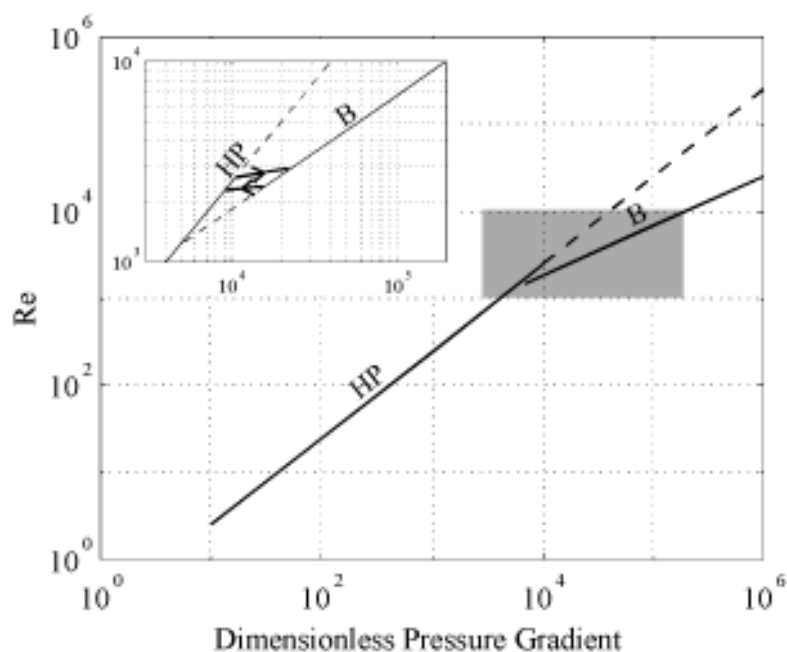


Figure 4.10 Reynolds number as a function of pressure gradient for pipe flow. HP marks the Hagen-Poiseuille relationship for laminar flow while B marks the Blasius relationship for fully turbulent flow. The inset shows approximately how the Reynolds number and pressure gradient change during slug flow.

On the other hand, a simple estimate of these forces can be made by calculating the change in the fluid's momentum between the laminar and turbulent flow regimes. Several assumptions are necessary. If the conduit is assumed to be completely filled with either laminarly or turbulently flowing fluid with the transition between the two regimes occurring in 0.001 s, and if the compressibility of the fluid is neglected, then Table 6 gives the change in fluid momentum, Δp , for several different fluids. These values are calculated for a Reynolds number of 2675 and a fundamental frequency of $f_1 = 0.63$ Hz. In addition, Table 6 gives the conduit dimensions and fluid density and velocity for these flow parameters. The change in momentum of the fluid in the conduit is the force on the fluid in remaining in the reservoir. In this case, only water produces a force comparable to the values of 3.2×10^6 and 1.1×10^6 N determined for harmonic tremor in Section 3.1.2. If the transition is assumed to occur slowly in 0.2 s, the interval given by the intermittency, the forces are much smaller (Table 6).

Table 6 -- Slug Flow Forces

Fluid	Density (kg/m ³)	Conduit Diameter ⁽¹⁾ (m)	Conduit Length ⁽²⁾ (m)	Velocity ⁽³⁾ (m/s)	Mass of Fluid (kg)	$\Delta p^{(4)}$ (N)	$\Delta p^{(5)}$ (N)
Water (100° C)	1000	0.35	17	11	1600	2.6×10^6	1.3×10^4
Air (1x10 ⁵ Pa, 100° C)	0.9	0.32	16	10	1.2	1800	9
Air (1x10 ⁵ Pa, 300° C)	0.6	0.46	23	14	2.3	4900	24
Steam (1x10 ⁵ Pa, 100° C)	0.6	0.3	15	9.5	0.6	900	5
Steam (1x10 ⁵ Pa, 300° C)	0.4	0.48	24	15	1.6	3600	18
Steam (2x10 ⁷ Pa, 300° C)	7	0.11	6	3.5	0.4	200	1

(1) Calculated from $Re=vd/\kappa$, with $Re=2675$, $v=d f_1$ and $f_1 = 0.63$ Hz

(2) Calculated from $L/d=50$

(3) Velocity during laminar flow

(4) Calculated assuming fluid velocity drops by 15% due to turbulence in 0.001 s

(5) Calculated assuming fluid velocity drops by 15% due to turbulence in 13% of one period or 0.2 s

4.3 Soda Bottle

When a system such as a volcano is closed to the atmosphere, the liquids, either magma or water in the hydrothermal system, must be saturated with gases. When such a system opens rapidly, the rapid and explosive degassing which takes place is usually a volcanic eruption or explosion. If, on the other hand, the opening is very small, the gases can only escape slowly. This may give rise to a cycle of pressure drop and bubble formation which can often be observed when a bottle of carbonated water is opened slightly [SOLTZBERG, 1997]. Similar cycles have also been observed in the slow decompression of more viscous fluids used to model volcanic systems [HAMMER et al, 1998]

Figure 4.11 shows a series of pictures taken of a bottle of soda water after its cap was opened only a small amount. Initially, the gas escapes slowly with a hissing noise, and the gas pressure in the volume above the water decreases. When the pressure has dropped enough to overcome the bubble surface tension [LEIGHTON, 1994, SOLTZBERG et al, 1997], bubbles form throughout the water. Their presence compensates for the initial decrease in pressure and therefore inhibits the formation of more bubbles. While gas continues to escape through the “vent” in the cap, the existing bubbles rise toward the surface during an interval which depends on the size (depth) of the bottle. When all the bubbles have reached the surface they can no longer contribute to the pressurization of the bottle, so the pressure again drops as gas continues to escape. When the pressure has dropped enough to overcome the bubble surface tension, the cycle begins again.



Figure 4.11 Photograph series of bubble cycle in a slightly opened bottle of soda water. On the left, the bottle has just been opened. Time increases toward the right.

A similar situation may exist in a volcano, where a small vent or opening allows gas to escape slowly. The volcano's reservoir of gas-saturated magma or water is large, and may, for the purposes of a simulation, be considered to provide an endless supply of gas when the pressure drops below the saturation level. In such a case, the soda bottle cycle could continue for hours.

To describe the processes in the slightly opened soda bottle quantitatively several assumptions are necessary. Figure 4.12 shows schematic pictures of the soda bottle during an interval when there are no bubbles and at a later point in the cycle when bubbles have formed. The gas, particularly at high temperatures such as would be expected in a volcano, may be described using the ideal gas law [GERTHSEN et al, 1974]

$$PV = NRT , \quad (4.11a)$$

where P and V are the pressure and volume of N moles of ideal gas at temperature T . R is the universal gas constant. If the number of moles is rewritten as the quotient of the total mass of the gas divided by its molecular mass, m/M_{gas} , this equation becomes

$$PV = \frac{R}{M_{gas}} mT = mR'T , \quad (4.11b)$$

where R' , the universal gas constant, has been normalized by M_{gas} . The mass of the gas divided by its volume is its density, ρ , giving the relationship

$$P = \rho R'T \quad (4.11c)$$

From Equation 4.11b, the time derivative of the mass flux may be written as

$$R'T\dot{m} = \dot{p}V + p\dot{V} . \quad (4.12)$$

If we assume that the volume of the fluid present does not change, then the total volume filled with gas also remains constant, so that $V = V_0$ and $\dot{V} = 0$. As is to be expected, changes in the pressure in the gas-filled region depend on the mass flux

$$\dot{P} = \frac{R'T}{V_0} \dot{m} = \frac{R'T}{V_0} [\dot{m}_e + \dot{m}_b] . \quad (4.13)$$

Two factors contribute to the mass flux, gas escaping from the volume through the vent and gas leaving the liquid in the form of bubbles. The mass flux of escaping gas, \dot{m}_e , is the product of the density of the gas, ρ , times the cross-sectional area of the vent, q , and the velocity of the gas, v . The mass flux of gas entering the gas-filled volume from bubbles, \dot{m}_b , can be described by product of the mean density of bubbles,

$$\bar{\rho}_b = n_b \left\langle \frac{4\pi}{3} r_b^3 \rho_{gas} \right\rangle , \quad (4.14)$$

with the cross-sectional area of the liquid, Q , and the mean ascent velocity of the bubbles, \bar{v}_b . In Equation 4.14, n_b is the number of bubbles per unit volume, and the factor in brackets is the mean bubble mass, calculated from the volume of spherical bubbles of radii r_b , and their density, ρ_{gas} .

The change in pressure as a function of time is then

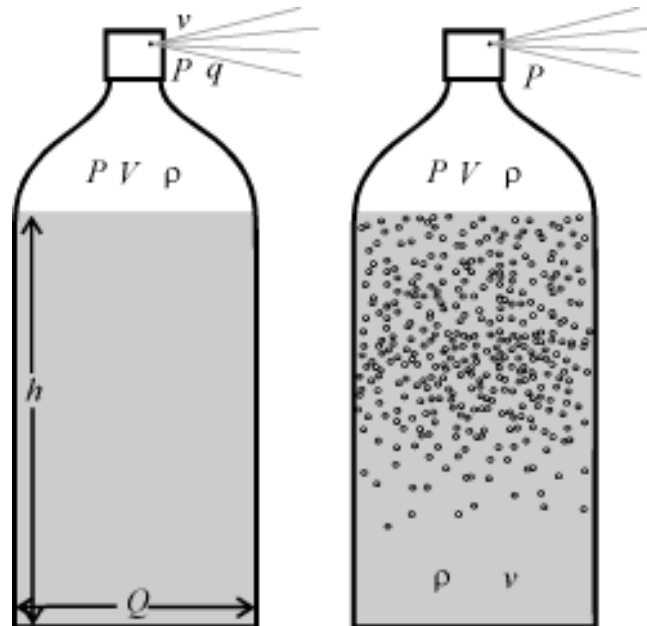


Figure 4.12 Sketch of soda bottle showing parameters used in Equations 4.11 - 4.21.

$$\dot{P} = \frac{R'T}{V_0} [\dot{m}_e + \dot{m}_b] = \frac{R'T}{V_0} [-\rho qv + \bar{\rho}_b Q \bar{v}_b] \quad (4.15)$$

It is not unreasonable to assume that the geometric parameters, such as Q and q , remain constant over several degassing cycles in a soda bottle or a volcano. Further, we may assume that the velocity of the escaping gas, v , is proportional to the difference in pressure between the interior of the bottle or volcano and the outside, with a proportionality constant k' [GINZBURG, 1963]

$$v = k'(P - P_a). \quad (4.16)$$

Inserting these values into Equation 4.15 and using Equation 4.11c for the density of the gas, gives a non-linear differential equation for the pressure:

$$\dot{P} = -\frac{qk'}{V_0} P(P - P_a) + \frac{R'TQ}{V_0} \bar{\rho}_b \bar{v}_b = -\frac{qk'}{V_0} P^2 + \frac{qk'P_a}{V_0} P + c_b = \quad (4.17)$$

$c_1 = qk'/V_0$, and $c_2 = c_1 P_a$ are constants for the soda bottle, and may vary slowly as a function of time in a volcano. If the bubbles rise with constant velocity the final parameter,

$$c_b = \frac{R'TQ}{V_0} \bar{\rho}_b \bar{v}_b, \quad (4.18)$$

may be related to the kinematic viscosity of the liquid by setting Stoke's law equal to the bubbles' bouyancy and and solving for the velocity .

$$c_b = \frac{R'TQ}{V_0} \bar{\rho}_b \frac{2\pi\bar{r}_b^2 g}{9\kappa}, \quad (4.19)$$

Thus, c_b is inversely proportional to the kinematic viscosity of the liquid.

In fact, c_b is non-zero only if bubbles are present, since $\bar{\rho}_b$ is proportional to n_b , the number of bubbles per unit volume. The presence of bubbles depends on the bubble

nucleation rate. According to SOLTZBERG et al [1997], the bubble nucleation rate, \dot{n}_b , is an exponential function of the Helmholtz energy, ΔE_H , necessary to form a bubble,

$$\dot{n}_b \propto \exp(-\Delta E_H / kT), \quad (4.20)$$

where k is Boltzmann's constant and T is the temperature. From classical nucleation theory, the Helmholtz energy is proportional to the cube of the bubble surface tension, σ_s , and inversely proportional to the square of the difference between the supersaturation concentration of dissolved gas in the fluid, c_s , and the equilibrium concentration, c_{eq} . Using Henry's law, $c = KP$, these concentrations can be used to relate the Helmholtz energy to the original pressure in the system, as well as, the pressure after it drops,

$$\Delta E_H = 16\pi\sigma_s^3 K^2 / 3(c_s - c_{eq})^2 = 16\pi\sigma_s^3 / 3(P_s - P_{eq})^2. \quad (4.21)$$

For the soda bottle, P_s is the initial pressure of gas in the bottle. Bubbles begin to form when $P_{eq} = 2\sigma_s/r_b$, that is, when it reaches the Laplace pressure corresponding to the surface tension in a bubble of radius r_b .

Initially, there are no bubbles in the bottle, $n_b \sim 0$. According to Equation 4.20, \dot{n}_b is very small and nearly constant until $P_s \sim P_{eq}$, when it very suddenly becomes extremely large. Thus, no bubbles appear spontaneously until the pressure drop exceeds the Laplace pressure. They immediately cease to form as soon as P_{eq} rises again due to the presence of bubbles.

To simplify calculations, Equation 4.17 can be solved for two cases. I assume $c_b = 0$ initially when no bubbles are present, and after a wave of them has risen to the surface. It is a non-zero constant depending on the viscosity of the liquid, on the bubble density and rise velocity, and on the geometry of the chamber when bubbles are present. In this case, bubble formation acts as a regulator relay for the self-regulation of the pressure in the bottle or volcano [MAGNUS and POPP, 1997]. Equation 4.17 can be solved numerically, using Matlab, for example. Figure 4.13 shows several solutions for assumed initial conditions in a soda bottle. As c_b increases, that is with decreasing kinematic viscosity of the liquid, the bubbles rise more quickly and pressure oscillations increase dramatically in amplitude. To

produce the oscillations observed at Lascar, with a fundamental frequency of 0.63 Hz, the kinematic viscosity of the liquid involved must be low. It could, for example, be water near the surface at relatively low overpressure.

Although this description of the soda bottle phenomenon is highly simplified, the model generates non-sinusoidal waveforms (Figure 4.13) which resemble the seismograms of harmonic tremor at Lascar. They are produced by pressure variations inside the reservoir during the bubble formation cycle. Under the simple assumptions used for solving Equation 4.17, the pressure changed by more than a factor of 2.

ACHENBACH [1975] gives a relationship describing the wavefield generated by pressure changes in a spherical cavity of radius A in a homogeneous, isotropic and linearly elastic medium. If the pressure change is a step function, $P(t) = P_0 H(t)$ with $H(t)$ the Heaviside function, then the displacement potential is

$$\Phi(r,t) = -\frac{1}{4\mu} \frac{A^3 P_0}{r} [1 - (2 - 2\sigma)^{1/2} \exp(-\chi s) \sin(\phi s + \lambda)] H(s) \quad (4.22)$$

where α is the speed of longitudinal waves in the medium, σ is the Poisson ratio, μ is the shear modulus, χ , ϕ and λ are defined as

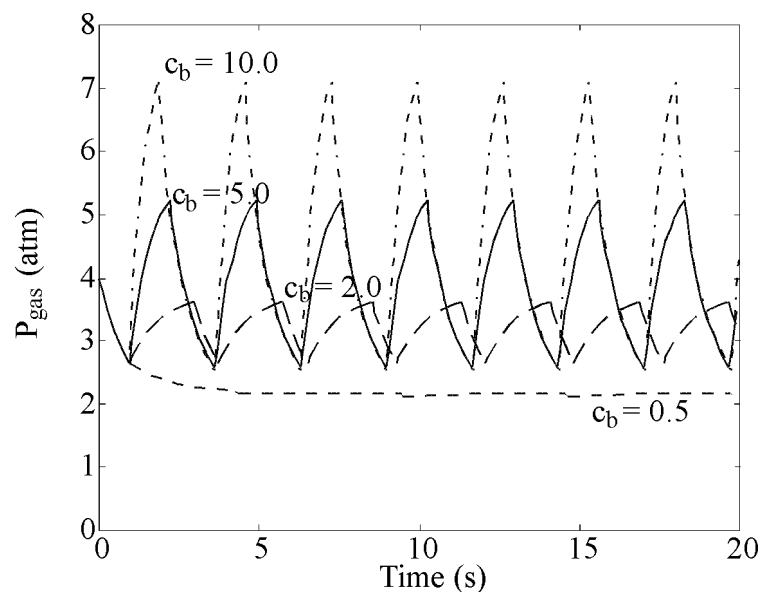


Figure 4.13 Pressure oscillations in a soda bottle with a small opening. The curves are marked with their initial conditions.

$$\chi = \frac{1-2\sigma}{1-\sigma} \frac{\alpha}{A}, \quad \varphi^2 = \frac{1-2\sigma}{(1-\sigma)^2} \frac{\alpha^2}{A^2}, \quad \lambda = \cot^{-1}(1-2\sigma)^{1/2} \quad (\pi/4 \leq \lambda \leq \pi/2)$$

and

$$s = t - \frac{r-a}{c_L}.$$

A pulse of finite duration, τ , can be simulated by superimposing the displacement potential for a pressure change of equal but opposite magnitude a time τ after the initial pressurization. Solutions for Equation 4.22 giving the displacement at a distance $r = 4000$ m, using $\alpha = 1000$ m/s, $\sigma = 0.3$ and $\mu = 2 \times 10^{10}$ N/m² are plotted in Figure 4.14. The expected displacement is displayed as a function of the source radius, A , for initial pressures, $P_0 = 3$ atm, 5 atm and 7 atm, the pressures used in the calculations for Figure 4.13. The root mean square displacement measured at LA2 is also plotted as a dashed line. It intersects the lines for all three atmospheric pressures at a radius of about 20 m. This indicates that

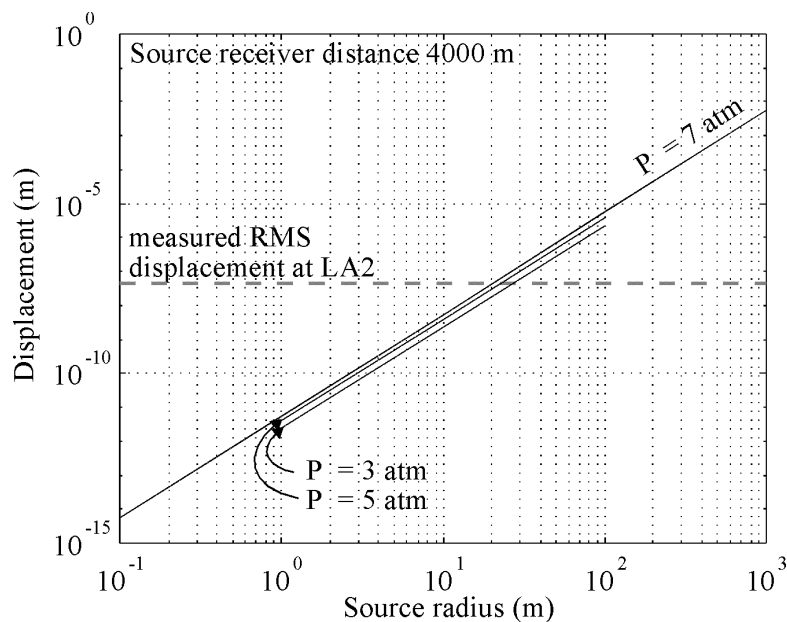


Figure 4.14 Displacement amplitude due to a pressure pulse at 4000 m distance from a spherical cavity of radius A in a homogeneous, isotropic and linearly elastic medium calculated using Equation 4.22. The dashed line is the root mean square displacement amplitude measured at station LA2. The solid lines are for pressure differences between the interior of the sphere and the environment of 3 atm, 5 atm and 7 atm.

under the simplifying assumptions used here, fluctuating pressure of the order of magnitude described above in a sphere with a radius of 20 m, or approximately $3 \times 10^4 \text{ m}^3$ volume, could produce the harmonic tremor seismograms measured at Lascar. If harmonic tremor is produced by such a mechanism, Lascar must contain such a volume of boiling or otherwise periodically degassing fluid.

5 Tremor Polarization: The Medium

The polarization pattern of Lascar's harmonic tremor described in Section 3.4 is puzzling when viewed in terms of analysis procedures from earthquake seismology. Although each spectral peak has a predominant polarization direction at each station, the wavefield can not be explained as either P, S or surface waves from a single point source. There are three possible explanations. The source radiation may be much more complex than that expected from a point source, giving rise to the polarization patterns observed in Section 3.4. A second possibility is that the source radiation pattern is relatively simple and the path along which harmonic tremor oscillations propagate and the conditions at the measurement site affect the polarization of the measured signals. Finally, at Lascar the particle motion may be produced by some combination from these two contributions. In the first case, the polarization of harmonic tremor can give new insights into the tremor source. If either of the other two possibilities is true, the tremor polarization cannot be used to learn about the source.

Using harmonic tremor recordings from the Lascar network, it is not possible to distinguish between these three explanations. If simple models for propagation effects can produce the observed polarization characteristics, then they may not be used for source modelling without additional evidence. Three simple models for the interaction of harmonic tremor waves with the medium demonstrate possible effects on the polarization: point scatterers in an acoustic medium, the superposition of P and S waves and the effects of reflections at the surface.

5.1 Scattering

The codas of volcanic shocks are an indication that scattering is an important phenomenon in wave propagation in volcanoes [Section 2.3.1, AKI and CHOUET, 1975]. The harmonic tremor wavefield must also be affected. A simple, three-dimensional model of an acoustic medium with no attenuation can demonstrate the qualitative effects of scattering on impulsive wavelets, as well as on continuous sine and square waves.

In the model, a 16 km by 16 km by 16 km grid of scatterers is embedded in an infinite, acoustic medium. Since the medium is infinite, there are no reflections from its boundaries. Because the medium is acoustic, it transmits only compressional waves. Although the volcanic medium is probably highly attenuating, this simple model does not include intrinsic attenuation.

The scatterers are located at randomly selected nodes of the 4096 km³ grid and their density can be varied. This model uses the Born approximation, which assumes that the scatterers are much smaller than the wavelength of the incident waves.

The velocity amplitude of a spherically propagating, acoustic wave of frequency $\omega = 2\pi f$ from a point source, in a medium in which the velocity of sound is c , is given by INGARD [1988]:

$$\dot{u}(r) = \frac{U_0 a_0}{r} \frac{1 + i/k r}{1 + i/k a_0} \exp(ikr - ika_0) \quad (5.1)$$

In this equation, U_0 is the velocity amplitude as a function of time at the source-medium interface at radius a_0 , while $k = \omega/c$ is the wave number. The wave propagating a distance r from an isotropically scattering monopole, s , at r_s takes on the same form,

$$\dot{u}_s(r) = \frac{\dot{u}(r_s) a_s}{r} \varepsilon_s \frac{1 + i/k r}{1 + i/k a_s} \exp(ikr - ika_s) \quad (5.2)$$

with the exception that U_0 is replaced by $\dot{u}(r_s)$, the amplitude of the incident wave at the location of the scatterer, times the scatterer's efficiency, ε_s , and a_0 is replaced by the diameter of the scatterer a_s . For small values of ka_s , that is when the wavelength is much larger than the radius of the scatterer (Born approximation), the scatterer's efficiency is

$$\varepsilon_s = \sqrt{\frac{\theta_s}{[(\theta + \theta_s)^2 + (\chi + \chi_s)^2]}} \quad (5.3)$$

θ and θ_s are the normalized radiation resistance of the medium and the scatterers, while χ and χ_s are their respective reactances. This number can never be greater than 1, and varies depending on the characteristics of the medium and scatterers [INGARD, 1988]. In the model, each scatterer is randomly assigned a scattering efficiency, $0 < \varepsilon_s < 1$. This very simple

model holds when the density of scatterers is low, so that the incident wave at any point in the model can be assumed not to have lost any energy to scattering. If the scatterers are more dense, the incident wave at the scatterer will have lost energy and have a lower amplitude than that given in Equation 5.1. If the direct wave has travelled a distance r , the loss as compared to the wave amplitude with no scattering can be estimated as [INGARD, 1988]:

$$C_{scat} = \exp\left(-\frac{r \langle \varepsilon^2 \rangle \sigma_{scat} \rho_{scat}}{2}\right) \quad (5.4)$$

where $\langle \varepsilon^2 \rangle$ is the root mean square scattering efficiency, $\sigma_{scat} = 4\pi a_s^2$ is the scatterer cross-section and ρ_{scat} , the density of the scatterers, is taken to be the inverse of the cube of the mean interscatterer distance, δ_{scat} . For this model, I take both a_0 and a_s to be 100 m, half the separation of the grid points, and the velocity of sound to be $c = 1000$ m/s. Strictly speaking, the Born approximation implies that for this geometry, the model is only valid for frequencies below 3 Hz.

Figure 5.1 shows the geometry of one plane of the scattering medium containing the source (X) and receiver (O) for a realization of a densely scattering medium. The seismogram at the receiver location is the sum of contributions from the source and from the single scattering contribution of each point of the scattering grid.

$$\dot{u}_r = C_{scat}(r_0)\dot{u}(r_0) + \sum_s C_{scat}(r_s)\dot{u}_s(r_{s0}) \quad (5.5)$$

For each node the incident amplitude is corrected for attenuation due to scattering using Equation 5.4.

If the source only radiates at a single frequency, i.e. a sine wave, it is easy to use this equation to calculate its outwardly propagating wave and the corresponding scattered waves in the time domain and superpose them at the location of the receiver to generate the expected seismogram for the configuration of scatters. If the source has a finite bandwidth, however, the problem becomes more difficult because of the frequency dependent product

$kr = \omega r / c$ in Equations 5.1 and 5.2. I have therefore calculated the theoretical seismograms discussed in the following paragraphs in the frequency domain. First, the source seismogram is Fourier transformed. For each scatterer, s , this spectrum is multiplied by the amplitude factor describing the geometric distance decay and that due to scattering losses and by the phase factors describing the phase shifts due to the distance traveled to the scatterer s . The spectrum is further multiplied by geometric distance decay factors and phase shifts for the distance between the scatterer and the receiver. The resulting spectrum for the contribution to the seismogram from the scatterer s is resolved into a radial component, parallel to the direction between the source and the receiver, and a transverse component perpendicular to it in a chosen plane. Since these calculations are made under the assumption of acoustic scattering, the radial and transverse components at the receiver location depend only on the direction between the scatterer and the receiver. The radial and transverse contributions for each scatterer in the scattering model are added to the radial and transverse receiver spectra of the direct wave before they are inverse Fourier transformed to give the synthetic

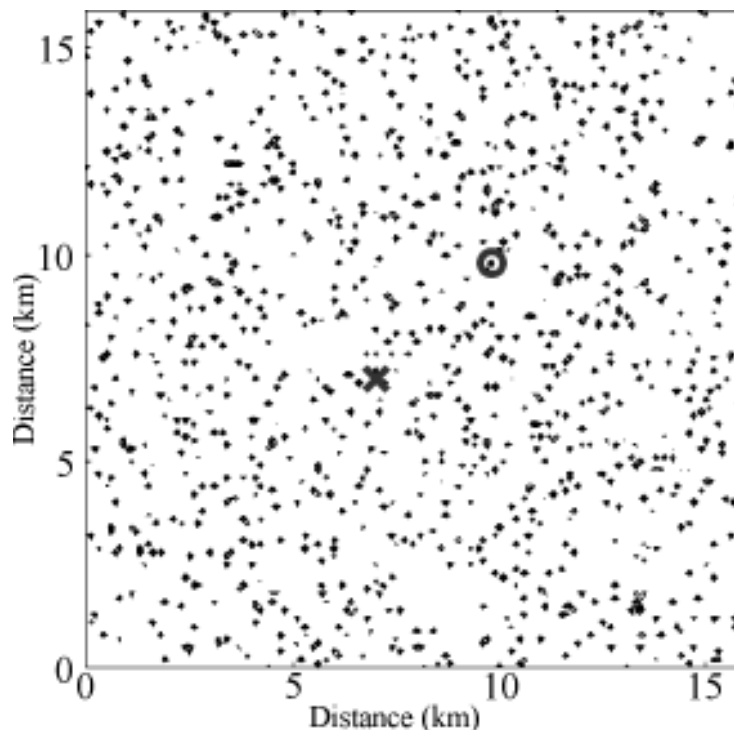


Figure 5.1 One plane of the three-dimensional sample scattering space containing the source (X) and receiver locations (O). The mean scatterer separation in three dimensions is 0.45 km. The distance between the source and receiver is 3.96 km.

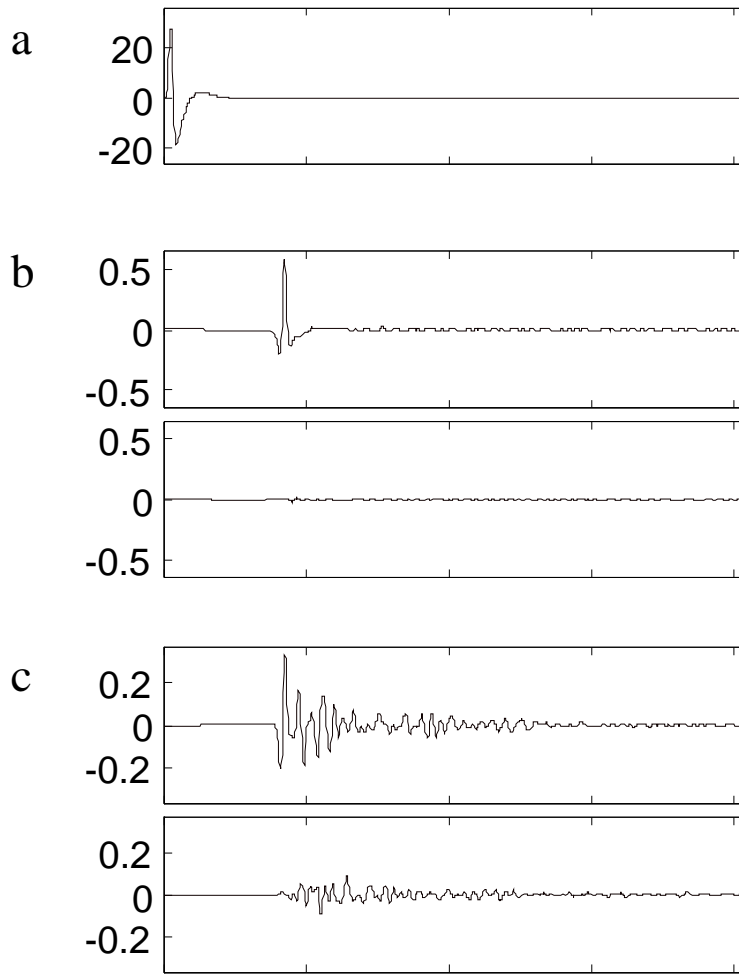


Figure 5.2 Source and scattered seismograms for an impulsive source. (a) The seismogram of ground velocity at the source. (b) Radial and transverse seismograms are plotted for a very sparse system of scatterers, 495 scatterers in 4096 km^3 and $\delta_{scat} = 2.0 \text{ km}$. (c) and (d) Seismograms for more densely scattering media with 25246 scatterers and $\delta_{scat} = 0.55 \text{ km}$ and 50509 scatterers and $\delta_{scat} = 0.43 \text{ km}$, respectively.

seismograms. The only disadvantage of this method is the acausality introduced by the manipulation of the spectra. It is apparent as a low level of energy that arrives at the receiver before the arrival of the direct wave.

If there are no scatterers, the wavefield at the receiver is by assumption only radial, regardless of the duration and shape of the source function. With scatterers, the situation changes. For an impulsive source, like an earthquake or explosion, these effects are familiar to analysts as the coda (Figure 5.2). The amplitude of the source for this and later figures is normalized so that the product of source amplitude and source radius are approximately equal to the amplitude of the incident wave excluding attenuation due to scattering times the source-receiver distance, $U_0 a_0 = \dot{u}(r_0) r_0$. Far from being narrowband, the spectrum of the impulsive source is broadband with contributions from many wavenumbers $k = \omega/c$. The effect of a medium with low scattering density is small, producing a small coda and a low level of energy on the transverse component (Figure 5.2b). The coda is effectively a transient which continues from the time of the first arrival until waves reflected from the most distant scatterers have returned to the receiver location. After the incident wave has passed the most distant scatterers, no more energy returns to the receiver, and the coda ends. When the number of scatterers increases, the simple, impulsive source function produces a seismogram similar to those measured for volcanic shocks like rapid fire tremor (Section 2.3.1), volcano-tectonic events and earthquakes. The energy is partitioned between the radial and transverse components (Figure 5.2c). The amplitude of the coda on the transverse component depends on the location and strength of the scatterers. When the density of scatterers is high, the maximum amplitude of the synthetic seismogram may be shifted from the onset to later in the seismogram, as it is in Figure 5.2d.

Unlike shocks which have an impulsive source, tremor signals continue for long intervals. A very simple example of such signals are tremor which have the appearance of a sine wave. These are narrowband signals which begin at some time, $t = 0$ s, and then continue on indefinitely (Figure 5.3a). If the density of scatterers is low (Figure 5.3b), the wavefield at the receiver site is similar to that in a medium without scatterers. The seismograms are nearly radially polarized. After the first arrival, the wave appears to continue unchanged until

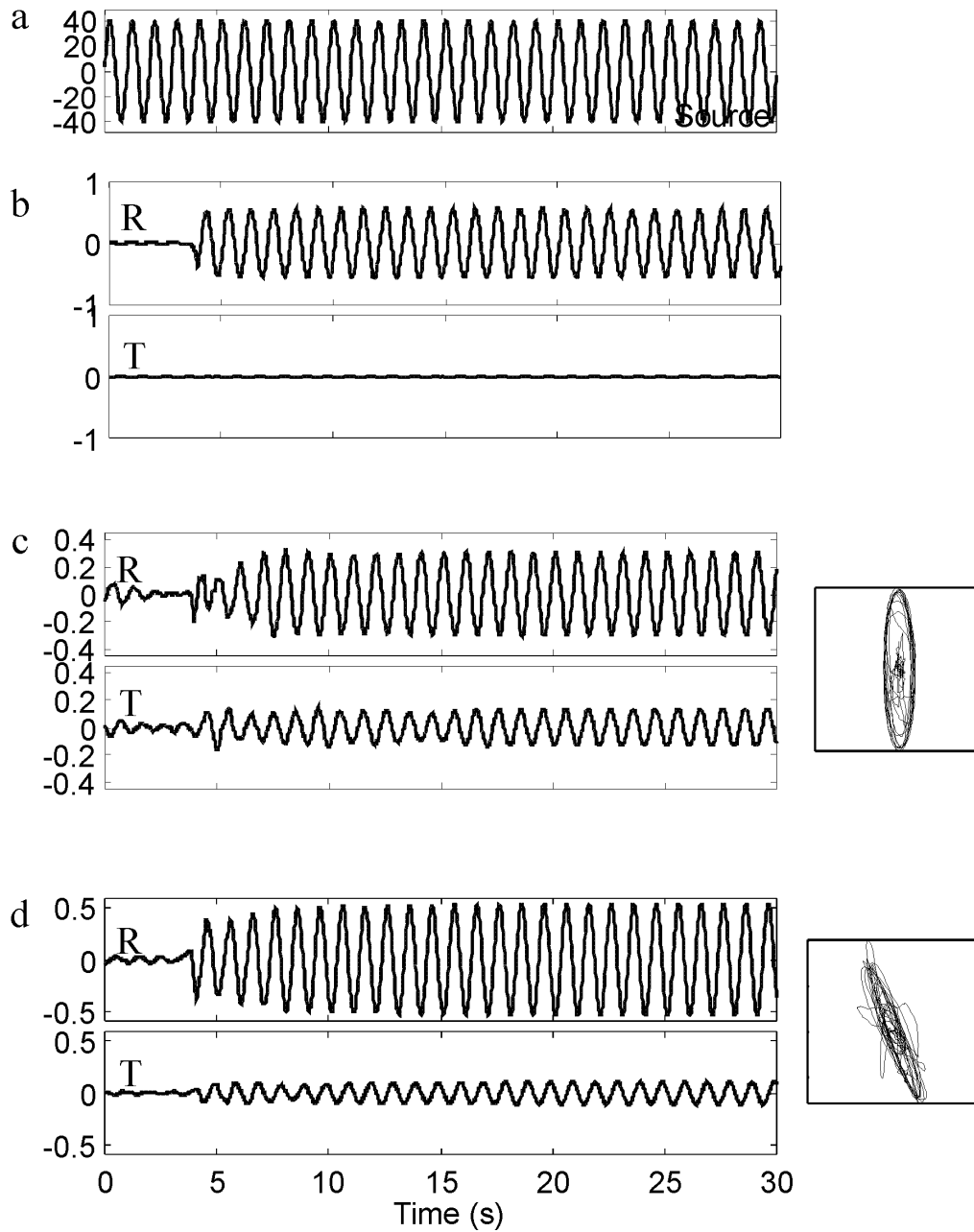


Figure 5.3 Source and scattered seismograms for a source generating a sinusoidal wavefield (1.0 Hz). (a) The seismogram of ground velocity at the source. (b) Radial and transverse seismograms are plotted for a very sparse system of scatterers, 451 scatterers in 4096 km^3 , with $\delta_{scat} = 2.0 \text{ km}$. (c) Radial and transverse seismograms for a more densely scattering medium with 25246 scatterers and $\delta_{scat} = 0.55 \text{ km}$ along with particle motion in the R-T plane. In this plot and all other particle motion diagrams, the radial axis is vertical and the transverse axis is horizontal. Both axes have the same scale. (d) Radial and transverse seismograms for a medium with 50509 scatterers and $\delta_{scat} = 0.43 \text{ km}$, along with the particle motion in an R-T plane. After a transient following the first onset ($\sim 5 \text{ s}$), the particle motion is constant and is not necessarily related to the source-receiver direction.

the end of the interval shown and the amplitude on the transverse component is very low. When there are more scatterers, however, there is a transient after the initial onset (Figure 5.3c). This is the interval between the first arrival and the time in which the outwardly propagating wave reaches the limits of the scattering medium and the scattered waves from the most distant scatterers return to the receiver. As the medium is infinite, there is no reflected wave. During this interval, the amplitudes of both the radial and transverse components change as the effects of more scatterers join the signal. After the transient stops, at about 10 s in this model, the amplitudes of both components remain constant, as does their relative phase. In general, the amplitude and phase of the transverse component depends on the location and strength of the scatterers. If the transverse component is in phase with the radial component (Figure 5.3d), the particle motion at the receiver site will be rotated from the radial and linearly polarized. The angle of rotation depends on the relative amplitudes of the two components. As the phase delay between the two components increases, the rectilinearity decreases. The particle motion no longer necessarily points to the source.

The results for a square wave source provide insights into the effects of propagation on Lascar's harmonic tremor (Figure 5.4). The square wave's spectrum is a sequence of narrowband peaks indicating that its wavefield is made up of waves with discrete wavenumbers $k_n = \omega_n / c$. If there are few scatterers, the transient is so small that it appears to be missing and the waves arriving at the receiver are primarily radially polarized (Figure 5.4b). Because there is little energy on the transverse component, each of the spectral lines is also radially polarized and highly rectilinear. When the number of scatterers increases, the transient after the onset lasts until the medium is saturated with outgoing and scattered radiation. The level of energy on the transverse component also increases. At the same time, for a given scatterer the relative phase for the different peaks depends on the wavenumber, $k_n r$. Thus, when the spectra from the many scatterers are superimposed at the receiver site, the polarization is different for each spectral peak and is not necessarily related to the source-receiver direction (Figures 5.4c and 5.4d). A small change in either the

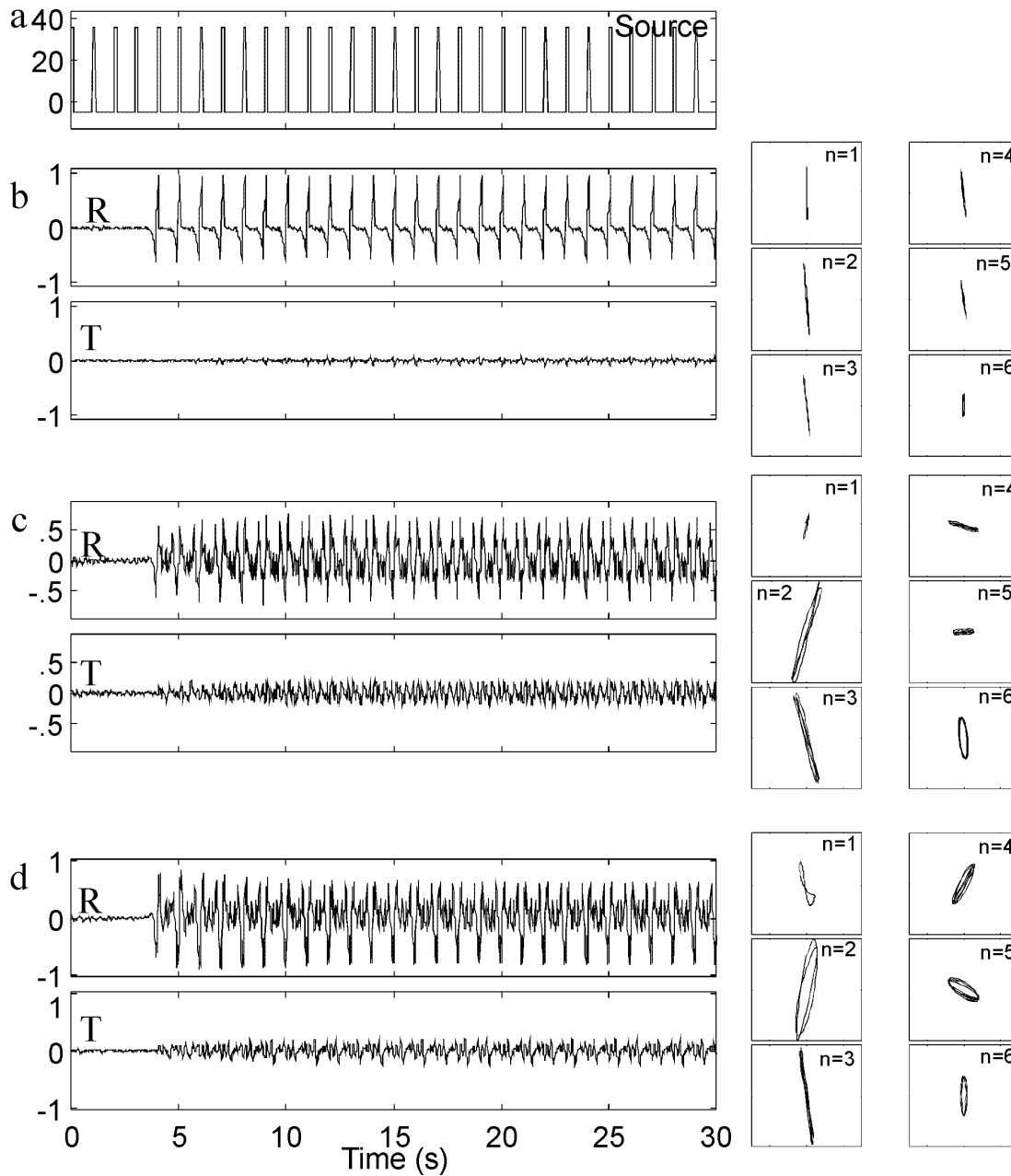


Figure 5.4 Source and scattered seismograms for a 1.0 Hz, 13% square wave source. (a) The seismogram for ground velocity at the source. (b) Radial and transverse seismograms are plotted for a very sparse system of scatterers, 528 scatterers in 4096 km^3 and $\delta_{scat} = 2.0 \text{ km}$. The particle motion diagrams show the particle motion for the data filtered to extract the first 6 harmonics. (c) and (d) Seismograms and particle motion diagrams for the first six harmonics for more densely scattering media with 24934 scatterers and $\delta_{scat} = 0.55 \text{ km}$ and 50582 scatterers and $\delta_{scat} = 0.43 \text{ km}$, respectively. The particle motion diagrams (horizontal axis T, vertical axis R) are taken from the interval between 20 s and 30 s, after the end of transient following the first onset. They show the polarization of the energy for the spectral lines $f_n = nf_1$, $n=1, 2, 3, 4, 5, 6$. For these plots the bandpass filter corner frequencies were [0.5, 1.5] Hz, [1.5, 2.5] Hz, [2.5, 3.5] Hz, [3.5, 4.5] Hz, [4.5, 5.5] Hz and [5.5, 6.5] Hz.

density of scatters or their location can completely change the pattern of particle motion as a function of frequency.

This acoustic model of single scattering with no attenuation demonstrates that even a simple system of scatterers can mimic important characteristics of volcanic shocks and tremor. The strong coda present in the shocks of rapid fire tremor (Figure 2.3a) indicates that scattering is an important process affecting the volcano's wavefield. A quantitative investigation of the volcano's structure using this extremely simple and qualitative scattering model to synthetically emulate the shocks' coda would, however, overrate the validity of the model. The three components of the shock records depend on the more complicated and yet unknown source process, as well as the direct and scattered P, S and surface waves. To properly model the shock codas requires an exhaustive investigation of these variables along with the effects of changes in scatterer size and efficiency and wave velocity.

This scattering model only allows qualitative conclusions about the volcanic medium. It must have many scatterers. Small, arbitrary changes in the locations and strengths of the scatters have a large effect on the polarization. The model also provides an explanation for the apparently unusual behavior of the polarization of the different frequency peaks of harmonic tremor at Lascar Volcano (Section 3.4).

5.2 Superposition

Normally a double couple, impulsive source will generate both P and S waves. Because the P waves, which are compressional waves, travel at a higher velocity than the S waves, they arrive at the station before the S waves which are transversely polarized. Explosive sources only excite P waves, but these may be converted near the source, so that the explosion's wavefield also includes both P and S waves. In the farfield of a single, impulsive source, the two types of waves are well separated in time. If the source is continuous, the recordings at the receiver location will be a superposition of both wavetypes. A very simple, two dimensional experiment can qualitatively demonstrate the effects of the concurrent arrival of these two wavetypes with the same frequency content on the polarization observed at a recorder. The geometry of the model is similar to that of the plane shown in Figure 5.1.

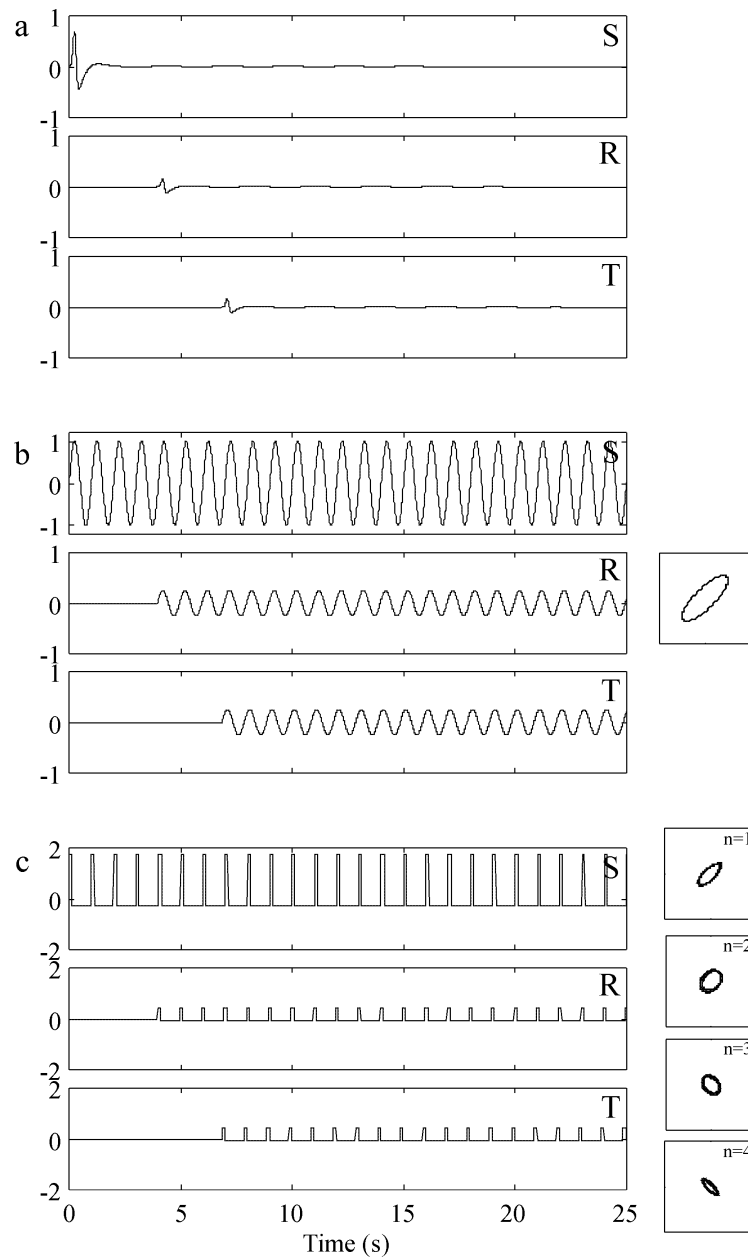


Figure 5.5 Source and station seismograms for a medium with P and S waves. The P-wave and S-wave velocities are $\alpha = 1.0$ km/s and $\beta = 0.58$ km/s. The distance between the source and station is 3.96 km. (a) Seismograms for a source pulse (S) and the radial (R, P wave) and transverse (T, S wave) arrivals at the station. (b) Seismograms for a sine wave source (1 Hz) and the radial and transverse seismograms at the station. The particle motion diagram shows the polarization under steady-state conditions. (c) Seismograms for a 13% square wave source (1 Hz) and the radial and transverse seismograms at the station. The particle motion diagrams show the polarization for the spectral lines $f_n = nf_1$, $n=1, 2, 3, 4$ under steady-state conditions. For these plots the bandpass filter corner frequencies are [0.5, 1.5] Hz, [1.5, 2.5] Hz, [2.5, 3.5] Hz and [3.5, 4.5] Hz.

The medium, however, has no scatterers and conducts both compressional waves that travel at $\alpha = 1000$ m/s and transverse waves that travel at $\beta = \alpha/\sqrt{3}$.

In the farfield of a single, impulsive source, the two wavetypes arrive separately (Figure 5.5, top) and the polarization for each arrival is well defined. When the source is continuous, the polarization becomes more complex. For a sine wave (Figure 5.5 middle), the compressional waves arrive first, but because they are generated continuously, they are still present when the first S-waves arrive, with a different phase and on the transverse component. Rather than producing separate movement as with the impulsive source, the particle motion is rotated from the radial or transverse. The polarization angle depends on the phase difference between the two waves, which in turn depends on the wave velocities and the distance travelled.

The model wave for harmonic tremor, a 13% square wave (Figure 5.5, bottom), also produces a superposition of phase-shifted P and S waves. The polarization for each harmonic depends, as it did for the sine wave, on the phase of the contributions from each wavetype. Because the phase-shifts depend on the frequency and the distance travelled, the polarization is different for each spectral peak. For each of the harmonics shown in the particle motion diagrams, the polarization direction bears no apparent relationship to the propagation direction of the seismic waves.

5.3 Surface Reflections

In a homogeneous space, the particle motion of P waves is parallel to the source-receiver direction, while that of S waves is perpendicular to it. The reflections generated by P or S waves at a free surface, such as a seismometer site, have been described by NUTTLI and WHITMORE [1961] and NUTTLI [1961], respectively. The recorded seismogram is a sum of the particle motion due to the incoming wave and the reflected waves.

The case for P waves is fairly simple. At the free surface, an incoming P wave generates a reflected P wave and a reflected S_v wave. All of the motion is in the plane defined by the wave propagation ray and the vertical direction, and the azimuth determined from the particle

motion points toward the source. In contrast, the inclination of the particle motion or apparent incidence angle, \bar{i}_0 , is distorted from the incidence angle of the incoming ray, i_0 :

$$i_0 = \sin^{-1} \sqrt{(1 - \cos \bar{i}_0) \alpha^2 / \beta^2} . \quad (5.6)$$

If the P and S wave velocities, α and β , are known, the incidence angle of the incoming wave can be calculated from the apparent incidence angle.

S waves produce a more complicated picture. The motion due to the part of the S wave parallel to the Earth's surface, S_H , is reflected simply, producing only a reflected S_H wave. Since the particle motion for this wave is perpendicular to the direction of propagation and parallel to the surface of the earth, the recorded ground motion is

$$\bar{u}_H = 2U_H \cos \omega t \quad (5.7)$$

if $U_H \cos \omega t$ is the S_H ground motion due to the incoming wave. The particle motion due to the rest of the incident S wave, called S_V , is perpendicular to S_H and to the incidence angle, j_0 , at an angle $90-j_0$. Like the P wave, all of its energy is in the vertical plane defined by the propagation direction. This wave produces a reflected S_V wave at an outgoing angle j_0 and a reflected P wave at an outgoing angle i_0 . There are two more complications to this situation. The particle motion of the incoming and outgoing S_V waves have the same vertical amplitude but opposite horizontal motion. Adding them together gives motion that is only vertical. Also, when the incidence angle of the incoming S_V wave is sufficiently large, $j_0 > \sin(\beta/\alpha)$, then $\sin i_0$ is greater than 1, and i_0 is imaginary [NUTTLI, 1961]. Thus, the particle motion due to S waves recorded at the seismometer depends strongly on the incidence angle of the incoming wave and the ratio of S_H to S_V energy. Figure 5.6 shows the particle motion for incidence angles between 0° and 90° . The particle motion is calculated assuming that $\beta = \alpha/\sqrt{3}$ and that the ground motion due to the incident S_V waves is $U_V = U_H \cos \omega t$, that is, energy is evenly partitioned between S_H and S_V waves and they are in phase. Between 35° and 40° the particle motion becomes non-linearly polarized as the outgoing angle for the reflected P-wave becomes complex. NUTTLI (1961) gives an excellent summary of the expected particle

motion due to S waves under various incidence angles and different ratios of S_H to S_V energy.

If the wavefield consists of S waves in an isotropic medium, then a receiver on the surface will record complex motion due to the incoming S_H and S_V energy and all the concomitant reflected waves. Normally a seismic station is assumed to rest on a horizontal surface and the source to lie below the surface. In fact, most volcano stations, as those at Lascar, are installed on slopes, and the source may lie in the crater at a higher altitude than the station. In such cases the incident angles may easily exceed $\sin^{-1}(\beta/a)$.

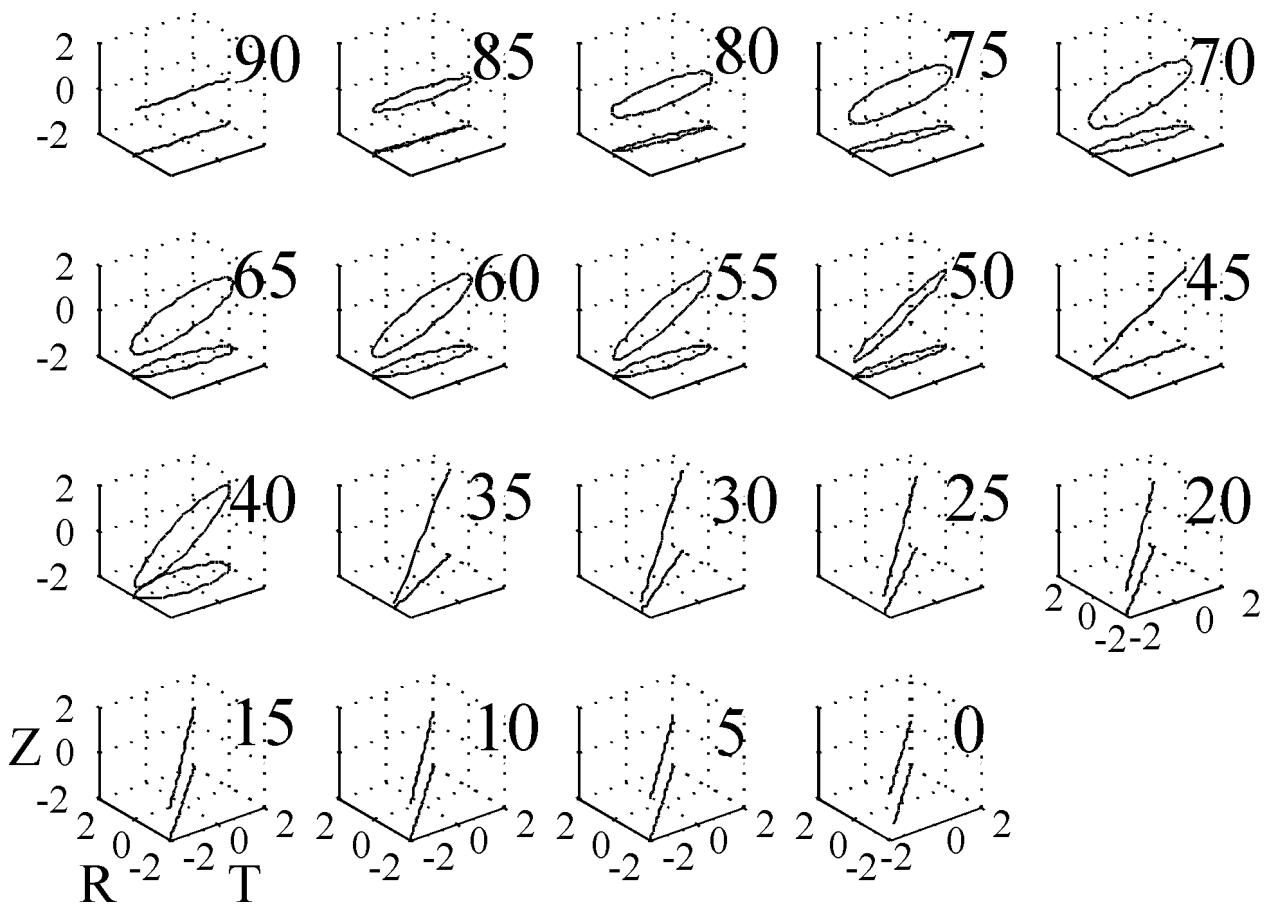


Figure 5.6 Particle motion for S waves (S_H/S_V ratio = 1) reflected at a horizontal surface in an isotropic medium for various incidence angles. The particle motion is given in the coordinate system [transverse (T) - radial (R) - vertical (Z)]. The incidence angle is measured from vertically down.

5.4 Summary

It is inviting to use the particle motion of a propagating wave, as in earthquake analysis, to learn more about the source, either by drawing conclusions about its location or the types of waves it is generating. Unfortunately, the polarization of the different spectral peaks of Lascar's harmonic tremor described in Section 3.4 cannot be used in this fashion. The particle motion may be caused either by source complexity, by propagation effects, or by some combination of these two factors.

The simple models for propagation effects presented in this chapter indicate that the observed polarization characteristics can be produced in continuous signals by path and site conditions. Taken individually each model reproduces some of the polarization and phase characteristics observed in harmonic tremor. Realistically, factors from all three models must in some way be represented in the Lascar. Scattering is certainly an important factor in wave transmission, as are the presence of P and S waves and their reflections at the surface. Even if Lascar's harmonic tremor began at the source with a simple polarization and with a well-defined phase relationship between the overtones, after passing through even a simple volcanic medium which could be described by these models, the polarization and waveforms would be very complex. Any source complexities affecting the polarization and phase of the harmonics are completely masked by these effects.

6 Conclusions

Like other active volcanoes, Lascar generates many different kinds of seismic signals. The interval of harmonic tremor, with its regularly peaked spectrum, recorded by PISCO's Lascar network is unique in its number of overtones and its duration. Similar signals observed at other volcanoes only occur during a short interval following a triggering event and have only a few overtones [KAMO et al., 1977, MORI et al., 1989, SCHLINDWEIN et al., 1995, BENOIT and McNUTT, 1997, HAGERTY et al., 1997, LEES et al, 1997].

Even at Lascar, episodes of harmonic tremor are relatively rare. Nonetheless this type of tremor provides new insights into the inner workings of volcanoes. Because it so obviously does not fit the accepted source models for volcanic tremor [for example, CHOUET, 1996, SCHLINDWEIN et al., 1995, McNUTT, 1994], it also demands their reexamination and invites the proposal of new models. On further evaluation these new models may be seen to apply not only to the special case of harmonic tremor, but more universally to other types of tremor.

The standard methods for seismological data analysis were developed for the investigation of events, broadband wavelets with a distinct beginning and with a definable end. In contrast, volcanic tremor is a continuous signal generated by a persistent process. It usually has neither a clear beginning nor end. Often, it also has narrow band peaks in its spectrum. Common methods of seismological data analysis can provide a foundation on which to base tremor analysis. However, they miss much of the information encoded in the wavefield. The new methods presented here for analyzing the tremor frequencies as a function of time and for analyzing polarization offer additional insights into the behavior and characteristics of volcanic, and in particular harmonic, tremor.

The polarization of the wavefield of a impulsive source, measured using three component recordings from several stations, can often provide information about the location of the source or the type of wave. Unlike the polarization of first arrivals from events, however, the polarization of the harmonic peaks seems to be unrelated to the direction to the active crater, their probable source. Indeed, the particle motion of any given peak cannot be explained as a simple wavefield of P, S or surface waves from a single source. It is possible that the observed polarization patterns are caused by a complex and extended source.

However, they can also be explained as propagation effects on a steady-state wavefield. Scattering, the superposition of P and S waves and surface reflections affect the polarization of continuous waves in ways that mimic the recordings of harmonic tremor at Lascar. Before the particle motion can be used to derive source characteristics, such effects must be excluded. On the otherhand the long term stability of harmonic tremor's polarization indicates that the source remains in the same place for extended intervals.

The most striking feature of harmonic tremor is its cyclic nature. In the seismograms, the waveforms are highly repetitive, changing only slowly over the course of many periods. In spectra, the cycles take the form of a regular series of extremely sharp peaks which can be characterized by $f_n(t) = nf_1(t)$, where $T = 1/f_1(t)$ is the period of the cycles. The peaks are observed at the same frequencies at all the Lascar stations, indicating that they are a characteristic of the process generating the harmonic tremor.

Many models have been proposed for the source of volcanic tremor (SEIDL et al, 1981, FERRICK *et al*, 1982, JULIAN, 1994). Several attempt to explain tremor characterized by narrow spectral peaks as the oscillatory response of a gas or fluid-filled body to some unspecified force (MORI et al, 1989, SCHLINDWEIN et al, 1995, CHOUET, 1996). These models have two disadvantages. First, while the authors relate the frequencies of the peaks to geometric parameters which are volcano specific, many volcanoes throughout the world have peaks at similar frequencies. Thus, the tremor source must have characteristics that are not volcano dependent and that can vary over short (30 s) intervals by 30% or more (BENOIT and McNUTT, 1997, HELLWEG, 1997, LEES et al, 1997, HAGERTY et al, 1996). Second, with these models their proponents describe a static picture of the volcano, neglecting the forces and processes which are necessary to excite the oscillations. The harmonic tremor of Lascar, along with the high quality of the recordings and the insights from the methods presented here provide an improved foundation for new, physical models for the source.

Here, I present the three new models for the source of harmonic tremor which relate the tremor to dynamic flow processes in the volcano. The models are based on the results of both standard and new analysis methods. For the three models, eddy shedding, slug flow and soda bottle, the observed characteristics of the tremor, in particular its fundamental

frequency and the shape of the power spectrum are related to fluid dynamic variables of the models such as characteristic flow dimension (i.e. conduit size), kinematic viscosity of the fluid and flow velocity. Estimates of the signal amplitude generated by the eddy shedding and slug flow models suggest that the moving fluid is probably water.

All three models give the same result: If the flow dimensions and velocities are to remain within reasonable bounds,

1. Harmonic tremor must be generated by the **movement of water or gases like steam**, not magma,
2. Harmonic tremor must be generated **near the surface**, close to atmospheric pressure, therefore probably in the active crater, and
3. Changes in the tremor frequency are caused by **small, easily reversible changes in flow velocity**, rather than by changes in the geometry of the volcano's conduit system.

In addition, the physical processes described by the models occur in specific ranges of flow "amplitude" as described by the Reynolds number. If the Reynolds number is lower or higher, as it would be during other flow regimes, the same flow geometry would generate other types of signals. The sound associated with turbulent flow systems, for example, is considered broadband noise (MORSE and INGARD, 1968, TRITTON, 1988, FABER, 1995). Thus, these models may be applicable at many volcanoes and may, in addition, explain the continuous "background" tremor as part of the same phenomenon. If these models are correct, harmonic tremor, and perhaps other forms of tremor, are symptoms of activity in the hydrothermal system of the volcano. Increases in tremor amplitude may then be related to increases in heat flow.

Although each volcano is unique, many share a characteristic: the tremor at many volcanoes has one or more sharp peaks between 0.5 and 2 Hz. One important question of volcano seismology has been to find the uniting factor which will explain such similarities. The models for harmonic tremor presented here provide the common factor: harmonic tremor is generated by the flow of heated gases or water in the near-surface hydro/gas-thermal system of the volcano.

8 References

- ACHENBACH, J.D. (1975): Wave Propagation in Elastic Solids, American Elsevier Publishing Co., New York, pp. 425.
- AKI, K. and P.G. RICHARDS (1980): Quantitative Seismology, W.H. Freeman and Co., San Francisco, pp. 920.
- AKI, K. and B. CHOUET, B. (1975): Origin of coda waves: source, attenuation, and scattering effects, *J. Geophys. Res.*, **80**, 3322 - 3342.
- ANDRES R.J. and A.D. KASGNOC (1998): A time-averaged inventory of subaerial volcanic sulfur emissions. *J. Geophys. Res.*, **103**, 25251-25261.
- ASCH, G., G. BOCK, F. GRÄBER, C. HABERLAND, M. HELLWEG, R. KIND, A. RUDLOFF and K. WYLLAGALLA (1995): Passive Seismologie im Rahmen von PISCO'94. *Sonderforschungsbereich 267 Deformationsprozesse in den Anden, Berichtband für die Jahre 1993-1995*, Berlin, 619-677.
- ASCH, G., K. WYLLAGALLA, M. HELLWEG, D. SEIDL and H. RADEMACHER (1996): Observations of Rapid-Fire Event Tremor at Lascar Volcano, Chile. *Annali di Geofisica*, **39**, 273-282.
- BATCHELOR, G.K. (1994): *An Introduction to Fluid Dynamics*. Cambridge University Press, Cambridge, pp. 615.
- BENOIT, J. and S.R. McNUTT (1997): New constraints on source processes of volcanic tremor at Arenal volcano, Costa Rica, using broadband seismic data. *Geophys. Res. Lett.* **24**, 449-452.
- BENOIT, J.P. S. McNUTT, W. MELSON, V. BARBOZA and J. BARQUERO (1995): Spectral and polarization analysis of broadband recordings of volcanic tremor at Arenal Volcano, Costa Rica. *EOS Tran. AGU*, **76** (46), Fall Meeting Supp., F349.

- BIRKHOFF, G. and E.H. ZARANTONELLO (1957): *Jets, Wakes and Cavities*. Academic Press, New York, pp. 353.
- BLAKE, W.K. (1986): *Mechanics of Flow-Induced Sound and Vibration, volume I*, Academic Press, New York, pp. 425.
- BUTTKUS, B. (1991): *Spektralanalyse und Filtertheorie*. Springer Verlag, Berlin, pp. 650.
- CHOUET, B. (1996): New methods and future trends in seismological volcano monitoring, in Scarpa and Tilling (eds): *Monitoring and Mitigation of Volcano Hazards*. Springer-Verlag, 23-97.
- CHOUET, B., G. SACCOROTTI, M. MARTINI, P. DAWSON, G. DE LUCA, G. MILANA and R. SCARPA (1997): Source and Path effects in the wave fields of tremor and explosions at Stromboli Volcano, Italy. *J. Geophys. Res.*, **102**, 15129-15150.
- DOUMA, J.H. (1974): Field Experiences with Hydraulic Structures, in *Flow Induced Structural Vibrations*. E. Naschauer, ed. Springer Verlag, Heidelberg, 223-249.
- DZIEWONSKI, A.M. and A.L. HALES (1972): Numerical Analysis of Dispersed Seismic Waves, in *Methods in Computational Physics*. B. Bolt, ed. Academic Press, New York, 39-85.
- FABER, T.E. (1995): *Fluid Dynamics for Physicists*. Cambridge University Press, Cambridge, pp. 440.
- FARNBACH, J.S. (1975): The Complex Envelope in Seismic Signal Analysis, *Bull. Seismol. Soc. Am.*, **65**, 951-962.
- FERRICK, M.G., A. QAMAR and W.F. ST. LAWRENCE (1982): Source Mechanism of Volcanic Tremor, *J. Geophys. Res.*, **87**, 8,675-8,683.
- FINCH, R.H. (1949): Volcanic Tremor (Part I), *Bull. Seismol. Soc. Am.*, **39**, 73-78.

- FUENTEALBA, G. and M. MURILLO (1994): Sismicidad del Volcan Lascar: Enero - Octubre 1993, in *Volcan Lascar Geologia y Evaluacion del Riesgo Volcanico — Altiplano II Region*, ed. Gardeweg, M, Servicio Nacional de Geología y Minería 1994-3, 104-120.
- GARCÉS, M.A. (1997): On the volcanic waveguide, *J. Geophys Res.* **102**, 22547-22564.
- GARDEWEG, M. and E. MEDINA (1994): La Erupcion Subpliniana del 19-20 de Abril de 1993 del Volcan Lascar, N. de Chile, *Actas del 7. Congreso Geologico Chileno 1994*, **1**, 299-304.
- GERTHSEN, C., H.O.KNESER and H. VOGEL (1974): *Physik*, Springer Verlag, Heidelberg, pp. 914.
- GIL-CRUZ, F. (1999): Observations of two special kinds of tremor at Galeras volcano, Colombia (1989-1991), *Ann. Geofis.* **42**, 437-450.
- GINZBURG, I.P. (1963): *Applied Fluid Dynamics*, National Science Foundation, Washington, DC, pp. 258.
- GÓMEZ, D. and R. TORRES, (1997): Unusual low-frequency seismic events with slowly decaying coda wave observed at Galeras and other volcanoes. In: J. Stix, M.L. Calvache V. and S.N. Williams (editors), Galeras Volcano, Colombia: Interdisciplinary Study of a Decade Volcano. *J. Volcanol. Geotherm. Res.*, **77** (1-4), 173-193.
- GONCHAROV, L.A. and V.M. SEMENKOV (1974): Field Investigations of Dam and Gate Vibrations, in *Flow Induced Structural Vibrations*, E. Naschauer, ed. Springer Verlag, Heidelberg, 278-296.
- HAGERTY, M.T., S.Y. SCHWARTZ and J. PROTTI (1996): Seismic and geodetic observations at Volcano Arenal, Costa Rica, *EOS Tran. AGU*, **77**(46), Fall Meeting Supp., F813.

- HAGERTY, M.T., S.Y. SCHWARTZ, J. PROTTI, M. GARCES and T. DIXON (1997): Observations at Costa Rican Volcano Offer Clues to Causes of Eruptions *EOS Tran. AGU*, **78**(49), 565,570.
- HAMADA, N., H. JINGU and K. IKUMOTO (1976): On the volcanic earthquakes with slowly decaying coda wave. *Bulletin of the Volcanological Society of Japan*, **21** 167-183.
- HAMMER, J.E., M. MANGA and K.V. CASHMAN (1998): Non-equilibrium and unsteady fluid degassing during slow decompression. *Geophys. Res. Let.* **25**, 4565-4568.
- HELLWEG, M. (1997): Listening carefully: Unique observations of harmonic tremor at Lascar volcano, Chile. *Ann. Geofis.* **42**, 451-465.
- HELLWEG, M., D. SEIDL, KIRBANI S. B. and W. BRUESTLE (1994): Team investigates activity at Mt. Semeru, Java, Volcano. *EOS*, **75**, 313-317.
- HILL, D.P., W. L. ELLSWORTH, M.J.S. JOHNSTON, J.O. LANGBEIN, D.H. OPPENHEIMER, A.M. PITT, P.A. REASENBERG, J.L. SOREY and S.R. McNUTT (1990): The 1989 Earthquake Swarm Beneath Mammoth Mountain, California, An Initial Look at the 4 May through 30 September Activity, *Bull. Seis. Soc. Am.*, **80**, 325-339.
- HOGAN, J.M. and M.V. MORKOVIN (1974): On the Response of Separated Pockets to Modulations of the Free Stream, in *Flow Induced Structural Vibrations*, E. Naschauer, ed. Springer Verlag, Heidelberg, 47-56.
- INGARD, K.U. (1988): *Fundamentals of Waves and Oscillations*, Cambridge University Press, Cambridge, pp. 595.
- JULIAN, B.R. (1994): Volcanic tremor: Nonlinear excitation by fluid flow, *J. Geophys. Res.*, **99**, 11,859-11,877.
- KAMO, K., T. FURUZAWA and J. AKAMATSU (1977): Some Natures of Volcanic Micro-tremors at the Sakura-Jima Volcano, *Bull. Volcanol. Soc. Japan*, **22**, 41-59.

- KANASEWICH, E.R. (1981): *Time Sequence Analysis in Geophysics*, The University of Alberta Press, Alberta, pp 480.
- LEE, W.H.K and J.C. LAHR (1975): HYPO71 (Revised): A computer program for determining hypocenter, magnitude, and first motion pattern of local earthquakes, *USGS Open File Report 75-311*, pp. 114.
- LEES, J.J., J. JOHNSON, E. GORDEEV, K. BATEREAU and A. OZEROV (1997): Volcanic Explosions at Karymsky: A Broadband Experiment around the Cone, *EOS Tran. AGU*, **78**(46), Fall Meeting Supp., F430.
- LEIGHTON, T.G. (1994): *The Acoustic Bubble*, Academic Press, London, pp. 613.
- LIGHTHILL, J. (1993): *Waves in Fluids*, Cambridge University Press, Cambridge, pp. 504.
- LJATKHER, V.M., M.V. SLADNEV and I.S. SHEININ (1980): Hydroelasticity effects in hydraulic engineering practice, in *Practical Experiences with Flow-Induced Vibrations*, E. Naschauer and D. Rockwell, ed. Springer Verlag, Heidelberg, 414-427.
- LYSSENKO, P.E. and G.A. CHEPAJKIN (1974): On Self-Excited Oscillations of Gate Seals, in *Flow Induced Structural Vibrations*, E. Naschauer, ed. Springer Verlag, Heidelberg, 278-296.
- MAGNUS K. and K. POPP (1997): *Schwingungen*, B.G. Teubner, Stuttgart, pp. 400.
- MATSUMURA, S. (1981): Three-dimensional expression of seismic particle motions by the trajectory ellipsoid and its application to the seismic data observed in the Kanto district, Japan, *J. Phys. Earth*, **29**, 221-239.
- McNUTT, S.R. (1994): Volcanic Tremor from Around the World: 1992 Update, *Acta Vulc.*, **5**, 197-200.

- MORI, J., H. PATIA, C MCKEE, I. ITIKARAI, P. LOWENSTEIN, P. DE SAINT OURS and B. TALAI (1989): Seismicity associated with eruptive activity at Langila Volcano, Papua New Guinea. *J. Volcanol Geotherm. Res.*, **38**, 243-255.
- MORSE, P.M. and K.U. INGARD (1968): *Theoretical Acoustics*, McGraw-Hill Book Co. New York, pp. 927.
- MURASE, T. and A.R. MCBIRNEY (1973): Properties of some Common Igneous Rocks and Their Melts at High Temperatures, *Geol. Soc. Am. Bull.*, **84**, 3563-3592.
- NARVÁEZ, L., R. TORRES, D. GÓMEZ, G. CORTÉS and H. CEPEDA, (1997): Tornillo-type seismic signal at Galeras Volcano, Colombia, 1992-1993. In: J. Stix, M.L. Calvache V. and S.N. Williams (editors), Galeras Volcano, Colombia: Interdisciplinary Study of a Decade Volcano. *J. Volcanol. Geotherm. Res.*, **77** (1-4), pp. 159-171.
- NUTTLI, O. (1961): The Effect of the Earth's Surface on the S Wave Particle Motion, *Bull. Seismol. Soc. Am.*, **51**, 237-246.
- NUTTLI, O. and J.D. WHITMORE. (1961): An Observational Determination of the Variation of the Angle of Incidence of P Waves with Epicentral Distance, *Bull. Seismol. Soc. Am.*, **51**, 269-276.
- OMER, G.C. (1950): Volcanic Tremor (Part II: The Theory of Volcanic Tremor), *Bull. Seismol. Soc. Am.*, **40**, 175-194.
- PLEŠINGER, A., M. HELLWEG and D. SEIDL (1986): Interactive High-resolution Polarization Analysis of Broad-band Seismograms, *J. Geophysics*, **59**, 129-139.
- RAYLEIGH, J.W.S. (1945): *The Theory of Sound, Vol. II*, Dover Publications, New York, pp. 504.
- RIPEPE, M and T. BRAUN (1993): Interactions of seismic and air waves recorded at Stromboli Volcano. *Geophys. Res. Lett.*, **20**, 65-68.

- SAWADA, M. (1998): The source mechanism of B-type and explosion earthquakes and origin of N-type earthquakes observed at Asama volcano, Central Japan, *Bull. Earthquake Research Institute*, submitted.
- SHAFFER, N.E. and R.N. ZARE (1991): Through a Beer Glass Darkly, *Physics Today*, **44**, 48-52.
- SCHICK, R. and G. SCHNEIDER (1973): *Physik des Erdkörpers*, Ferdinand Enke Verlag, Stuttgart, pp. 267.
- SCHLICHTING, H. (1958): *Grenzschicht-Theorie*, Verlag G. Braun, Karlsruhe, pp. 603.
- SCHLINDWEIN, V., J. WASSERMANN and F. SCHERBAUM (1995): Spectral analysis of harmonic tremor signals at Mt. Semeru volcano, Indonesia, 1995, *Geophys. Res. Lett.*, **22**, 1685-1688.
- SEIDL, D. and M. HELLWEG (1991): Volcanic Tremor Recordings: Polarization Analysis, in *Volcanic Tremor and Magma Flow*, R. Schick and R. Mugiono, eds. Forschungszentrum Jülich GmbH, 31-46.
- SEIDL, D., M. HELLWEG, R. TORRES and D. GÓMEZ (1998): Seismische Signale am Vulkan Galeras, Kolumbien: Sind Tornillos freie Schwingungen von Gasblasen? *58th Annual Meeting of the Deutsche Geophysikalische Gesellschaft*, Mar.30-Apr.3, 1998, Göttingen, Germany.
- SEIDL, D., R. SCHICK and M. RIUSCETTI (1981): Volcanic tremors at Etna: a model for hydraulic origin, *Bull. Volcan.* **44**, 43-56.
- SEKIYA, H. (1967): Volcano observation (History of Asama and volcanoes in Japan). *So-go Tosho Publication*, pp. 180.
- SHIMA, M. (1958): On the second volcanic micro-tremor at volcano Aso. *Bull. Disaster Prevent. Inst. Kyoto Univ.*, **22**, 1-6.

- SHIMOZURU, D. (1961): Volcanic micro-seisms - discussion on the origin. *Bull. Volcanol. Soc. Japan*, **5**, 154-162.
- SOLTZBERG, L.J., P.G. BOWERS and C. HOFSTETTER (1997): A computer model for soda bottle oscillations: "The bottelator". *J. Chem. Ed.*, **74**: 711-714.
- TAUBENHEIM, J. (1969): *Statistische Auswertung Geophysikalischer und Meteorologischer Daten*, Akademische Verlagsgesellschaft, Leipzig, pp. 386.
- TORRES, R., D. GÓMEZ and L. NARVÁEZ (1996): Unusual seismic signals associated with the activity at Galeras volcano, Colombia, from July 1992 to September 1994. *Ann. Geofis.*, **39**, 299-310.
- TRITTON, D. J. (1988): *Physical Fluid Dynamics*, Clarendon Press, Oxford, pp. 519.
- VIDALE, J. (1986): Complex Polarization Analysis of Particle Motion, *Bull. Seismol. Soc. Am.*, **76**, 1393-1405.
- WALKER, J. (1982): What happens when water boils, *Scient. Am.*, **247**, 144-148.
- WALLIS, G.B. (1969): *One-dimensional Two-phase Flow*, McGraw-Hill Book Co. New York, pp. 408.
- WASSERMAN, J. and F. SCHERBAUM (1994): Spectral Features and Polarization Patterns of Broadband Seismic Signals at Station Serra la Nave, Mt. Etna, Sicily, *Acta Vulcan.*, **5**, 211-220.
- WIELANDT, E. (1975): Generation of seismic waves by underwater explosions, *Geophys. J. Astron. Soc.* **40**, 421-439.
- ZÜRN, W. and P.Q. RYDELEK (1994): Revisiting the Phasor-Walkout Method for Detailed Investigation of Harmonic Signals in Time Series, *Surveys in Geophysics*, **15**, 409-431.

Acknowledgements

Many people and organizations contributed to the work that has culminated in this thesis. It is unfortunately impossible to thank all of them explicitly. The seismological data set which is the basis for the investigations discussed here were collected under the auspices of the “Proyecto de Investigación Sismológica de la Cordillera Occidental '94” (PISCO'94), part of the German Research Foundation Collaborative Research Program (SFB) 267, “*Deformationsprozesse in den Anden*”. I would like to thank its former speaker, Prof. Peter Giese of the Freie Universität Berlin, who approved the deployment at Lascar. The CDs are the result of the determination and valient efforts of Günter Asch, Alex Rudloff and Frank Gräber during field work truly worthy of that designation.

During his career, Prof. Rolf Schick inspired many colleagues and students with his enduring enthusiasm for volcanoes and their workings. I would like to thank him for infecting me with his enthusiasm and then agreeing to sponsor my work on this thesis at the Institut für Geophysik of the Universität Stuttgart. With his comments and criticism, Prof. Erhard Wielandt kept me on the physical “straight and narrow” while encouraging me to investigate the volcanic system as a whole.

Dieter Seidl (Erlangen) is the godfather of my career in seismology. I thank him for reflecting on my fundamental questions and helping to polarize my thinking. Bob Odom (Washington) provided me with random advice on scattered topics.

Moyra Gardeweg, of SERNAGEOMIN, the geological survey of Chile, kindly shared information about Lascar’s geologic and eruptive history with me, as well as allowing me the use of her map.

My family also did their part to contribute to this thesis. My three children, Ben, Nathan and Miriam helped by staying out of trouble, while my mother, Betty Karplus, refrained from troubling me while I was working. I particularly thank my husband, Horst Rademacher, who participated in the ups and downs of progress on this project.

7 Definition of Variables

α	P or compressional wave velocity
A	Cavity radius
$A(t)$	Instantaneous amplitude
A_n	RF event amplitude factor
a_0, a_s	Radius of source, radii of scatterers
β	S or shear wave velocity
b	Unitless constant
χ and χ_s	Radiation reactance of medium and scatterer
C	A normalization constant
C_{scat}	Amplitude decay factor due to scattering
c	Speed of sound in a fluid or gas
c_s and c_{eq}	Concentrations of dissolved gas
	Diameter of flow dimension
d	Cylinder diameter (vortex shedding) Conduit diameter (slug flow)
D	Duct diameter
d_{scat}	Mean distance between scatterers
ΔE_H	Helmholtz energy of bubble formation
E_{nT}	Total energy of a rapid fire event
ϵ_s	Scatterer efficiency
$f(t)$	Instantaneous frequency
F_0	Point force in the j direction
f_0	A fixed or test frequency
f_1	Fundamental frequency of harmonic tremor
f_K	Vortex shedding frequency
F_l	Force per unit length (vortex shedding)
f_n	Frequency of n th overtone ($f_n = nf_1, n = 1, 2, 3$)
f_i	Frequencies of transverse duct resonance ($i = 1, 2, 3$)
g	Gravitational acceleration
$g(t)$	Green's function
γ_i and γ_j	Directional cosines

η	Dynamic or shear viscosity
h	Depth
$H(t)$	Heaviside function
i_0	True incidence angle for P waves
\bar{i}_0	Apparent incidence angle
j_0	True incidence angle for SV waves
κ	Kinematic viscosity
k', k	Proportionality constant between pressure difference and flow velocity, Boltzmann constant, Wavenumber
K	Proportionality factor in Henry's Law
$k\Delta t$	A sequence of times spaced Δt , $k = 1, 2, 3, \dots$
λ	Poisson parameter
L	Separation between cylinders (vortex shedding) Length of conduit (slug flow)
m	Mass of gas
\dot{m}	Mass flux
\dot{m}_b	Mass flux due to bubbles
\dot{m}_e	Mass flux due to escaping gas
μ	Shear modulus
M_{gas}	Molecular mass of gas
N	Number of moles of gas
n_b, \dot{n}_b	Number of bubbles, Bubble nucleation rate
P	Pressure
\dot{P}	Time derivative of pressure
Δp	Change in momentum between laminar and turbulent flow
P_A	Atmospheric pressure
q	Cross-sectional area of soda bottle vent
Q	Cross-sectional area of bubble filled fluid
θ and θ_s	Radiation resistance of medium and scatterer
$\Theta(t)$	Instantaneous phase
Θ_R	Reduced instantaneous phase
ρ	Density

$\bar{\rho}_b$	Mean density of bubbles
ρ_{gas}	Density of gas in bubble
ρ_{scat}	Density of scatterers in medium
R	Universal gas constant
R'	Normalized universal gas constant
Re	Reynolds number (dimensionless)
r	Distance from source
r_0	Source receiver distance
r_b	Bubble radius
r_s	Source scatterer distance
r_{s0}	Scatterer receiver distance
σ	Poisson ratio
$s_0(t)$	Characteristic source function for RF events
$s_n(t)$	Source-time function of RF event n
σ_s	Surface tension
σ_{scat}	Scatterer cross-sectional area
St	Strouhal number (dimensionless)
t	Time
T	Temperature
τ	Pulse duration
T_c	Interval for sound pulse to travel distance L
T_D	Vortex drift interval
T_I	Intermittency factor (slug flow)
T_S	Interval of slug cycle
T_T	Interval of turbulence
$\dot{u}(t)$	Characteristic time function for RF events
\bar{u}_H	Recorded ground motion of SH waves
$u_i(x,t)$	The i th component of the displacement wavefield
$\dot{u}_i(x,t)$	The i th component of the velocity wavefield
$\dot{u}_{n\max}$	Maximum ground velocity
$\dot{u}_n(t)$	Ground velocity of RF event n
U_0	Velocity amplitude at the source

U_H	Ground motion due to incident SH waves
U_V	Ground motion due to incident SV waves
v	Velocity of flow for fluids
V	Gas volume
\dot{V}	Time derivative of volume
V_0	Constant volume of gas
v_A	Average flow velocity of slug
\bar{v}_b	Mean ascent velocity of bubbles
v_D	Vortex drift velocity
v_F	Flow velocity of front of slug
v_R	Flow velocity of rear of slug
$X(f_0, n)$	Fourier transform of n points of $x(t)$
$x(t)$	Some function of time
$y(t)=\mathbf{H}(x(t))$	Hilbert transform of $x(t)$
$z(t)$	Analytic function of $x(t)$